Seismic investigation of subduction in Cascadia and Alaska and Simulating the ability of MyShake networks to detect and locate earthquakes

by

Robert Michael Martin-Short

A dissertation submitted in partial satisfaction of the

requirements for the degree of

Doctor of Philosophy

in

Earth and Planetary Science

in the

Graduate Division

of the

University of California, Berkeley

Committee in charge:

Professor Richard M. Allen, Chair
Professor Mark Richards
Professor Walter Alvarez
Professor Fotini K. Chow

Summer 2019

Seismic investigation of subduction in Cascadia and Alaska and Simulating the ability of MyShake networks to detect and locate earthquakes

Abstract

Seismic investigation of subduction in Cascadia and Alaska and Simulating the ability of MyShake networks to detect and locate earthquakes

by

Robert Michael Martin-Short

Doctor of Philosophy in Earth and Planetary Science

University of California, Berkeley

Professor Richard M. Allen, Chair

This study has two major focuses, which are united by the theme of applying data processing and imaging techniques to extract valuable information from large volumes of seismic data.

The first focus is on the use of seismic imaging to improve our understanding of the tectonic settings of two of North-America's subduction zones; namely Cascadia and Alaska. Both exhibit enigmatic features and provide insight into fundamental seismotectonic processes relating to the interplay between subduction, mantle flow, volcanism and continental crust growth. Cascadia, for example, represents the final stages of subduction of the once giant Farallon plate. Using data collected from an ambitious deployment of ocean bottom seismometers across the entirety of the Juan-de-Fuca and Gorda plates offshore Oregon and Washington, this study maps the geometry of upper mantle flow in the region, which has important tectonic implications.

The Alaskan subduction zone contrasts with Cascadia because the downgoing oceanic lithosphere here is older and more seismically active. This study uses data from an unprecedented seismic survey of Alaska to construct high resolution, three dimensional models of the velocity structure from the surface down to about 400km depth. These elucidate many fascinating features of this region, including the geometry of the downgoing material and its relationship to several enigmatic volcanic provinces.

The second focus of this study is concerned with earthquake early warning. This is a technology that aims to provide seconds to minutes of warning to people before the onset of severe shaking during an earthquake, potentially allowing them to take life-saving actions. MyShake is a smartphone application developed by the U.C Berkeley Seismological Laboratory that allows mobile devices to detect earthquakes. MyShake is available for public download and is providing a rich dataset for investigation. This study describes an algorithm designed to use networks of MyShake devices to quickly locate and issue warnings about earthquakes, and a simulation workflow designed to test this approach. The results

indicate that MyShake networks have exciting potential to issue useful earthquake early warnings worldwide.

For my family, friends and mentors

Contents

List of Figures

Acknowledgments

A PhD is a long, challenging and unpredictable journey, but one that for me has been very rewarding and fulfilling. There are many people to whom I am incredibly grateful for making this possible, without whose guidance and support I could not have completed the program. I must start with a special thank you to my advisor, Richard Allen. Despite being incredibly busy in simultaneous roles as director of the U.C. Berkeley Seismic Laboratory and department chair, Richard has always found the time to provide guidance and support when I needed it. He has been consistently positive and helpful, introducing me to new ideas and research projects but also encouraging my participation in a host of exciting opportunities, some of which were completely unrelated to my research. Indeed, I am most grateful to Richard for his trust in allowing me to explore a wide range of projects, career opportunities and novel experiences while at Berkeley. Without this freedom I could never have learned and grown as much as I have in the past five years as his student.

My journey at Berkeley and fascination with the San Francisco bay area began 7 years ago, when I first came here as a visiting undergraduate student as part of my 'Geophysics with a year abroad' degree. I maintain that participating in this study abroad program, a daunting prospect for me at the time, was one of the best decisions I have ever made. I am grateful to my mentors at Imperial College London, especially to Lorraine Craig, who had the foresight to see how much I could gain from a year in Berkeley and whose organizational skills largely made it possible. While in Berkeley I experienced first hand some of the ups and downs of research life in the Seismolab, took a host of interesting classes and made great friendships at the International House, where I lived. I returned home to the UK absolutely convinced that I wanted to do a PhD in the bay area, and Richard accepted me back to Berkeley.

Since returning to the Seismolab as a graduate student the list of people and organizations I am indebted to for my many positive experiences here has grown steadily. I want to thank the staff at International House Berkeley for providing me with an amazing living experience the first two years of my PhD. I want to thank John Edmiston at the Lawrence Berkeley Laboratory for giving me the opportunity to undertake a very interesting semester-long computational research project with him and then, much later, for recommending me to the Insight data science program. I want to thank the organizers of the Collaborative Institute for Deep Earth Research (CIDER) program for allowing me to participate in the summer of 2016, and the organizers of the Los Alamos National Laboratory parallel computing internship for my time there 2017, especially Bob Robey and Eunmo Koo, who were fantastic mentors. Finally, I want to say a big thank you to the entire community at the Silicon Valley Insight program, which has enabled me to begin my new journey as a data scientist upon graduating from Berkeley.

One of the main reasons why I was able to have so many interesting experiences beyond

PhD research has been the friendly, secure, supportive environment that exists within the Department of Earth and Planetary Science and Berkeley Seismic Laboratory. I wish to thank the faculty, staff and my fellow students for providing this environment and for their help and support throughout the various challenges I've faced in my research. A special thank you goes to Avinash, Felipe, Cheng, Qingkai, Kathyrn, Nate, Claire, William and Sarina for their friendship, guidance and humor.

The seismological community as a whole, with which I have interacted at various conferences and workshops, has also been an invaluable resource though which I have gained access to valuable ideas, mentorship and software. On a related note, the ongoing student exchange program between Berkeley and Imperial College London would not have been possible without the dedication of Ian Bastow, who is now the main organizer of the program. Ian has also been an invaluable co-author on every one of my publications since arriving here. Though this program, I have have the opportunity to work with several excellent visiting undergraduate students from Imperial, which has taught me much about what it means to be a teacher and mentor.

My PhD experience has been immeasurably enriched by the diverse community of friends that I have made here in the San Francisco bay area and beyond. These people are one of my main reasons for wanting to stay here after graduating and I am incredibly grateful to be part of their lives. Finally, but perhaps most importantly, none of this would have been possible without the continued support of my parents in the UK. Being far away from home can be tough for all parties, but they have always enthusiastically supported my work here and provided truly invaluable guidance on multiple occasions when I had to make difficult decisions. With their support, my independence has grown to the point that a 10 hour flight home feels like a minor undertaking. Life at Berkeley has opened doors unimaginable to the three of us just a few years ago, so I think my parents are almost as excited as I am to see where they might lead.

Chapter 1

Introduction

The history of progress in seismology has been a history of increasingly accessible, high quality and high volume seismic data. During the early to mid 20th century, scientific pioneers such as Andrija Mohorovičić, Beno Gutenberg and Inge Lehmann made fundamental contributions to our knowledge of Earth's internal structure by observing seismic phases on just a handful of seismograms. Today, high resolution three-dimensional models of the seismic velocity of the subsurface are constructed using data from thousands or millions of seismograms. It is an exciting time to be a seismologist. Over the last century the field has established itself as a primary tool for determining the structure and composition of the Earth's interior. In the 21st century, the presence of freely available, high-quality data from large scale, community-driven experiments such as the Transportable Array (http://www.usarray.org/) is being combined with a plethora of new computational capabilities and tools for the analysis and transformation of this data into new knowledge about the planet and the hazards it presents to human society.

Recently, large volumes of seismic data area also being obtained from unconventional networks, such as fiber-optic cables (Lindsey et al. 2017) and smartphones (Kong et al. 2016). While presenting new and unique challenges, such non-traditional networks could provide dramatic advances in high resolution imaging and hazard analysis, especially when combined with state of the art processing techniques from the field of machine learning (e.g. Kong et al. 2018)

This dissertation is divided into two parts, which have very different objectives but are united by the theme of making use of data from modern seismic networks. The first part, which encompasses chapters 2-4, involves investigation of the structure and geometry of the Cascadia and Alaskan subduction zones. Here we use a variety of seismic techniques with data from traditional seismometer arrays to model properties of the crust and mantle within these subduction zones and to make interpretations about their tectonic history. The second part of this dissertation, which encompasses chapter 5, is concerned with seismic hazard.

We present a software platform designed to simulate the ability of networks of smartphones running the MyShake mobile application (Kong et al. 2016) to detect, locate and issue early warnings about local earthquakes. This is part of an ongoing effort by researchers in the Berkeley Seisological Laboratory to develop a public earthquake early warning system that incorporates data from MyShake phones.

The preceding three chapters deal with imaging of subduction zones. Subduction zones are a fascinating and complicated subset of plate boundaries, where one tectonic plate is sinking beneath another into the deep interior of the planet. They are worthy of study for a range of reasons, not least because plate locking there is responsible for the generation of great earthquakes and tsunamis, which threaten coastal communities wordwide. Subduction zones also transport sediments and fluids into earth's interior, where they interact with mantle material to generate the magma responsible for volcanic arcs (e.g. Hacker et al. 2003). As subducting lithosphere descends it also undergoes mineralogical phase transitions, which may be responsible for intermediate depth seismicity and change the relative density between the downgoing material and its surroundings. Finally, transportation of cool lithosphere into the deep mantle is a fundamental component of global mantle convection and may be the most important driving force behind plate tectonics (e.g. Conrad et al. 2007). Thus, the study of subduction zones is inherently multidisciplinary, requiring input from the seismological, geodynamic and geochemical communities.

The ages, compositions, fluid content and relative speed of the incoming and overriding plates are thought to control important characteristics of a subduction zone, such as the frequency and maximum magnitude of earthquakes, the location and eruptive style of volcanoes and the geometry of the downgoing plate at depth. The pioneering work of authors such as Uyeda and Kanamori (1979) and Uyeda (1982) grouped global subduction zones into a small number of broad categories based on their geometry, seismic activity and stress regime. However, recent high-resolution imaging of individual subduction zones (e.g. Cascadia; Hawley et al. 2016, Japan; Wei et al. 2015, Alaska; Martin-Short et al. 2018, Chile; Huang et al. 2018) has revealed dramatic changes in slab geometry, seismic, deformation and volcanism along strike, highlighting just how complicated and unique each subduction zone really is. These detailed studies have been made possible by the deployment of dense, regional scale networks of seismometers in conjunction with the development and use of imaging techniques and the computational resources required to implement them. These techniques include ambient noise tomography to investigate crustal structure (e.g. Shapiro et al. 2005), non-planar earthquake surface wave tomography to investigate the lower crust and uppermost mantle (e.g. Pollitz et al. 2010), receiver function analysis to determine discontinuity structure (e.g. Zhu et al. 2000, Cheng et al. 2017), finite frequency and full waveform body wave tomography to investigate slab geometry at depth (e.g. Bodmer et al. 2018, Simutė et al. 2016) and various joint inversions using subsets of these techniques. Each approach has its unique caveats, which explains why authors often draw upon non-seismic methods such as geodynamic models (e.g. Jadamec et al. 2010), geochemical analysis (e.g. Preece et al.

2004) and plate tectonic reconstructions (Boyden et al. 2011) to inform and support their interpretations.

In chapter 2 of this dissertation we focus on the Cascadia subduction zone, specifically an investigation of the geometry of mantle flow beneath the incoming Juan-de-Fuca and Gorda plates and interaction with the subducting material. To do this we use the well-established technique of teleseismic shear-wave splitting, which is used to determine the direction and magnitude of seismic anisotropy beneath a region (Silver et al. 1991). Data quality issues related to ocean bottom seismometers (OBS) present a major challenge to our workflow, but we provide a solid demonstration that shear wave splitting analysis can be used to extract scientifically useful results from such networks.

We support our interpretations with the results of a simple geodynamic model of flow beneath the Gorda plate (Martin-Short et al. 2015). This work complements and extends a growing body of literature about the Cascadia subduction zone, which has been made possible by ambitious deployments of offshore seismometers as part of the Cascadia Initiative (Toomey et al. 2014). Cascadia represents an end-member subduction zone, from which we can attempt to learn about tectonic plates where the ridge and trench are in relatively close proximity. The downgoing Juan-de-Fuca plate system here is the final remnant of the giant Farallon plate, which has almost completely subducted beneath North America. Consequently, the slab is warm and young (< 10 Mya). Although the age of the incoming plate varies little, there are multiple lines of evidence for along-strike segmentation of the Cascadia subduction zone. This includes co-located variation in tremor density and seismicity (Brudzinski et al. 2007), plate locking, subsurface discontinuity structure as inferred from receiver functions (Cheng et al. 2017) and seismic velocity structure (e.g. Hawley et al. 2016; Bodmer et al. 2018; Gao 2018). The strong correlations between the locations of segment boundaries as inferred from these independent observations are not well understood. However, they suggest a cause related to the buoyancy and hydration state of the downgoing material and the geology of the overriding plate. The region is also fascinating from a geodynamic perspective because it features a slab edge south of the Mendocino triple junction, around which asthenospheric material might flow (e.g. Zandt et al. 2008; Eakin et al. 2010). Furthermore, teleseismic body wave imaging suggests the presence of a gap or tear in the Juan-de-Fuca slab beneath Oregon, which may also have geodynamic implications (Obrebski et al. 2010; Long 2016). Our study sheds new light upon the geometry of mantle flow beneath the entirety of the Juan-de-Fuca plate system from ridge the trench and onshore beneath the downgoing slab. Very similar work by Bodmer et al. (2015) corroborates our results and interpretations.

In chapters 3 and 4 we turn our attention to another of North America's subduction zones, the Aleutian-Alaska arc. Here, the Pacific plate is converging beneath North America in a subduction system that appears to terminate below south-central Alaska. The Alaska subduction zone is very different to Cascadia: The downgoing plate is large and old, although there is significant variation in age along strike, seismicity is abundant and the region is

relatively unexplored from a geophysical perspective due to its remoteness. Geologically, much of the state of Alaska has been constructed via accretion of terranes brought into contact with its southern margin by subduction. Indeed, the process of continental crust growth can be observed in operation at present at the northeastern corner of the Pacific plate, where the thick oceanic crust of the Yakutat terrane is in the process of accreting to south-central Alaska. This process has led to a host of enigmatic tectonic features, including broad intraplate deformation, shallow subduction and the Denali Volcanic Gap, a zone of volcanic quiescence (Plafker et al. 1994). Large scale seismic imaging of Alaska has previously not been possible due to a lack of instrumentation. However, thanks to recent deployment of high quality, broadband, transportable array (TA) seismometers in Alaska between 2014 and 2018, we are provided with an unprecedented opportunity to image the crust and mantle structure beneath the entire region in high resolution. Chapter 3 is concerned with finite frequency, body wave tomography, which uses P- and S-waves from teleseismic events to construct three dimensional models of the velocity structure of the upper mantle beneath south-central Alaska. When published in 2016, this model provided the most comprehensive images of the geometry of the subducted slab here to date. It is notable for the discovery of a distinct, northeastern edge to the subducting material, which lies $\sim$ 100km east of the edge of the Wadati-Benioff zone, implying a zone of aseismic subduction.

However, despite providing comprehensive images of the slab at depth, the resolution of the teleseismic body wave models is insufficient to reveal the structure of the mantle wedge and continental crust, which is required to make interpretations about the cause of the Denali Volcanic Gap, for example. Thus, in chapter 4 we explore an alternative approach which makes use of joint inversions of ambient noise, earthquake Rayleigh wave and P-S receiver functions to image the absolute velocity structure of South-Central Alaska from the surface to $\sim$ 150km depth with sufficient detail to discern differences in the structure of the mantle wedge between the volcanic and non-volcanic regions and across the eastern edge of the slab.

As of the writing of this introduction chapter, the community is just beginning to publish exciting new results derived from data obtained by the Transportable Array in Alaska. Jiang et al. (2018), for example, present a 3D model obtained by joint inversion of teleseismic body and surface waves. They observe and comment on many of the same features that are present in the models of Martin-Short et al. (2016) and Martin-Short et al. (2018) (described in chapters 3 and 4). Ward and Lin (2018) present a similar model constructed using ambient noise and receiver functions, which is also remarkably consistent with Martin-Short et al. (2018), although the authors focus their analysis on shallower depths. By leveraging a set of seismic imaging techniques on the same dataset, researchers are validating and building upon earlier work and independently reaching similar conclusions about the subsurface structure and tectonic history of Alaska.

In the second part of this dissertation, which encompasses chapter 5, we turn our attention to seismic hazard, and in particular the potential uses of networks of smartphones for

applications in earthquake early warning. This is a very different subject to the three preceding chapters, but they are united by the overarching theme of developing novel uses for new, large scale sources of seismic data. MyShake is an android and IOS application that runs on personal mobile devices and uses an artificial neural network to distinguish between earthquake-related shaking and other activities as recorded by mobile phone accelerometers (Kong et al. 2016). Groups of stationary devices thus act like traditional seismic networks, so they can be used to quickly detect, locate and issue early warnings about earthquakes as they are occurring (e.g. Allen et al. 2003, Kong et al. 2016). Since its release in 2016, MyShake has been downloaded 300,000 times and there are currently $\sim$ 40,000 active users worldwide. As the network expands, so does its potential to contribute to earthquake early warning. Chapter 5 describes the construction and application of a simulation platform and network detection algorithm, which simulates the ability of MyShake networks to detect and locate earthquakes given the event source parameters (time, location, magnitude etc.) and proportion of the population of some region assumed to have the MyShake application installed on their personal devices. The platform accounts for unique challenges of the MyShake network, including variation in the number of steady phones as a function of time of day, uncertainty in the timing of triggers received from the phones and the possibility of random or spurious triggers. A network detection approach based on the DBSCAN clustering algorithm (Ester et al. 1996) is used to reliably associate clusters of MyShake device triggers with earthquake events. An optimization approach is then used to estimate the event source parameters. The purpose of this simulation platform is to demonstrate the ability of MyShake to contribute to earthquake early warning efforts in earthquake-prone regions around the world. To do this, we run a suite of simulations and report network performance for each region. Although the performance varies significantly with population distribution and event location, we show that MyShake networks will be capable of accurately locating and issuing early warnings for large ($M > 5.5$ events) in all of the regions we investigated, assuming that the app is being used by 0.1% of the population. This work is an important proof of concept of the MyShake project, whose ultimate goal is to become a global seismic network that can provide rapid, accurate early warnings to populations in earthquake-prone regions.

The final section of this dissertation is a conclusions chapter, which concisely summaries the major findings and unique contributions of this work.

Part I

Seismic investigation of subduction in Cascadia and Alaska

Chapter 2

Mantle flow geometry beneath the Gorda-Juan de Fuca plate system[1]

Advisor: Richard M. Allen

Coauthors: Ian Bastow, Eoghan Totten & Mark Richards

2.1 Chapter summary

Tectonic plates are underlain by a low viscosity mantle layer, the asthenosphere. Asthenospheric flow may be induced by the overriding plate or by deeper mantle convection (Conrad et al. 2007). Shear strain due to this flow can be inferred using the directional dependence of seismic wave speeds - seismic anisotropy. However, isolation of asthenospheric signals is challenging; most seismometers are located on continents, whose complex structure influences the seismic waves en-route to the surface. The Cascadia Initiative, an offshore seismometer deployment in the US Pacific Northwest, offers the opportunity to analyze seismic data recorded on simpler oceanic lithosphere (Toomey et al. 2014). Here we use measurements of seismic anisotropy across the Juan-de-Fuca and Gorda plates to reconstruct patterns of asthenospheric mantle shear flow from the Juan-de-Fuca mid-ocean ridge to the Cascadia subduction zone trench. We find that the direction of fastest seismic wave motion rotates with increasing distance from the mid-ocean ridge to become aligned with the direction of motion of the Juan-de-Fuca Plate, implying that this plate influences mantle flow. In contrast, asthenospheric flow beneath the Gorda Plate does not align with Gorda Plate motion and instead aligns with the neighbouring Pacific Plate motion. These results show that

[1]Published as Martin-Short, R, et al. Mantle flow geometry from ridge to trench beneath the Gorda-Juan de Fuca plate system. Nature Geoscience 8.12 (2015): 965.

asthenospheric flow beneath the small, slow-moving Gorda Plate is controlled largely by advection due to the much larger, faster-moving Pacific Plate.

2.2 Introduction

The Juan-de-Fuca plate system is the northernmost section of the Farallon slab, which is approaching complete subduction beneath the North American continent (Riddihough 1984). The system is subdivided into the Explorer, Juan-de-Fuca and Gorda segments, which subduct at $\sim$ 12mm/yr in a $\sim$ N60°E direction beneath the Cascadia arc (Eakin et al. 2010; Currie et al. 2004). The assemblage is undergoing rollback at $\sim$ 24mm/yr (Eakin et al. 2010) and rotating clockwise as the Mendocino Triple Junction (MTJ) migrates northwards (Eakin et al. 2010).

Questions about the mantle flow geometry beneath Cascadia focus on interaction between oceanic asthenosphere and the subducting slab (Long and Silver 2008). Shear wave splitting, a technique that quantifies the magnitude and direction of seismic anisotropy, can address such questions (Long and Silver 2008; Silver et al. 1991). Seismic anisotropy in the mantle develops due to the lattice-preferred orientation (LPO) of various minerals (Nicolas et al. 1987). Olivine, the main component of the upper mantle, is highly anisotropic (Nicolas et al. 1987; Karato et al. 2008). Simple shearing under typical asthenosphere conditions yields olivine crystal alignment, with fast axes corresponding to the shearing direction (Nicolas et al. 1987). Shear waves traversing such a medium are split into two orthogonal components, one of which is polarized in the fast direction. A delay time (δt) proportional to the strength and layer-thickness of the anisotropy is acquired as the components transit the layer. The fast axis direction (Φ) is used to determine the shearing direction and by inference the mantle flow geometry (Silver et al. 1991).

Onshore studies in Cascadia reveal uniformly trench perpendicular anisotropy, indicative of sub-slab mantle flow (Currie et al. 2004; Long and Silver 2008). Cascadia is unusual; most subduction zones demonstrate trench-parallel splitting (Long and Silver 2008). This has been variously interpreted as rollback-induced flow (Long and Silver 2008) , the influence of B-type olivine LPO in the mantle wedge (Karato et al. 2008), or the consequence of strong radial anisotropy in steeply dipping, entrained flow (Song et al. 2012).

We analyze data from Cascadia Initiative seismometer deployments (Toomey et al. 2014), including 27 onshore Transportable Array (TA) sites and 70 ocean bottom seismometers (OBS), deployed in ten-month phases at 160 sites (Toomey et al. 2014). We analyze OBS data from years 1-3 of the Cascadia Initiative and 4 years of records from the NEPTUNE cabled seafloor observatory. Public data from the X9 OBS array, deployed along the Blanco Fracture Zone in 2012-20132 are also utilized (Figure 2.1).

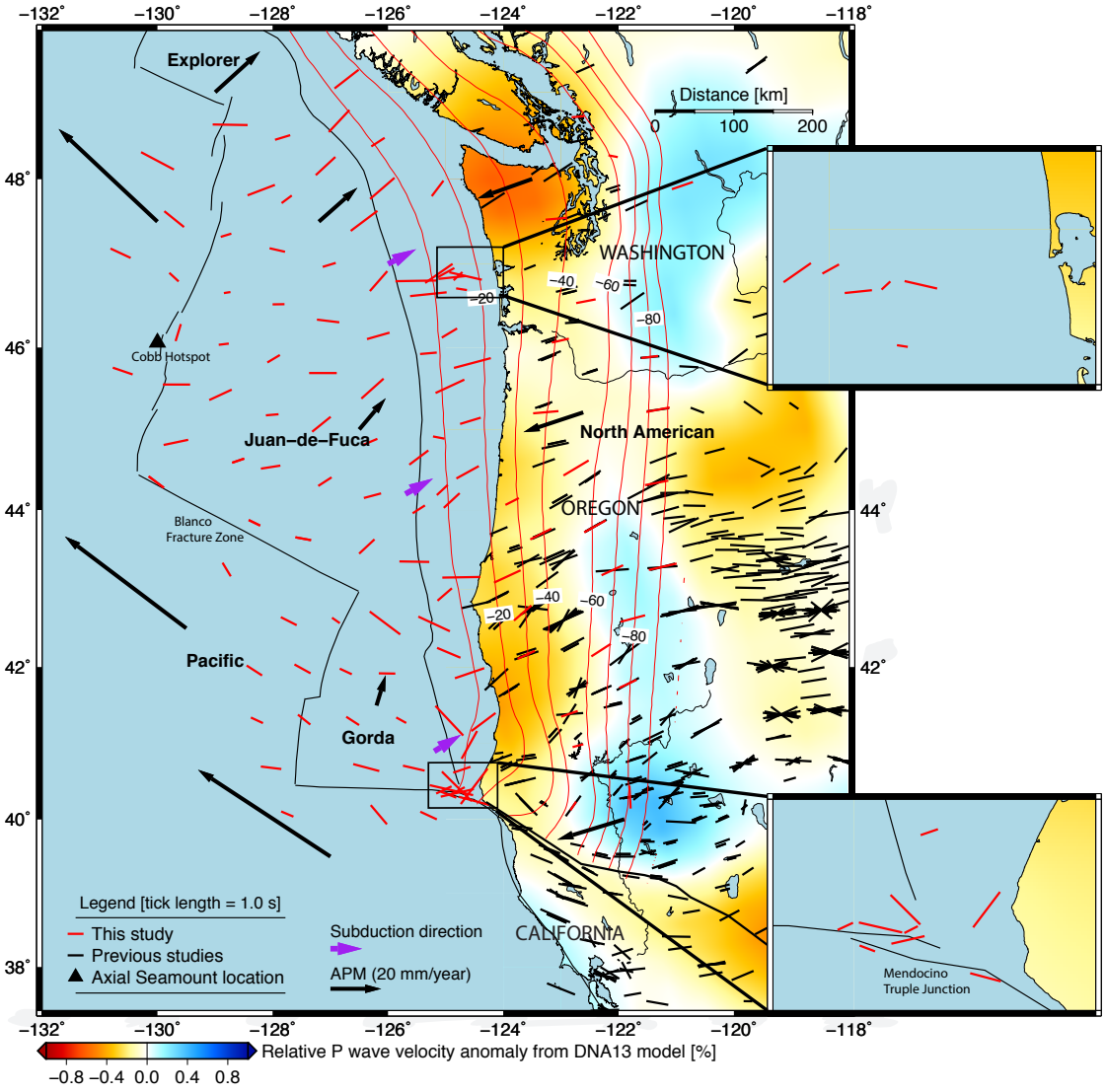

Figure 2.1: Stacked splitting results determined by this study (red bars) and previous work (back bars; from Eakin et al. 2010 and Wüstefeld et al. (2009) The displayed tomography is a 100-400km vertical average through the DNA13 P-wave velocity model of Porritt et al. (2014). This depth range corresponds to that part of the asthenosphere considered most likely to be the source of the observed anisotropy (Karato et al. 2008). All splits are plotted at seismometer station/OBS locations. Black lines indicate plate boundaries, while the red lines are slab depth contours spaced at 10km intervals (Hayes et al. 2012). Black arrows show the direction and magnitude of absolute plate motion in a hotspot reference frame (Debayle et al. 2013), while purple arrows show the subduction direction (Eakin et al. 2010). Insert maps show regions featuring a high concentration of splitting results.

2.3 Methods

Shear wave splitting

Shear wave splitting with OBS data is challenging due to high noise levels within the S frequency band (Bell et al. 2014; Webb 1998) and uncertainty in instrument orientation (Lodewyk et al. 2014). We generally obtain 1-4 good quality measurements per offshore station, compared to 8-15 results for the onshore sites.

We determine the splitting parameters Φ and δt for each station-event pair using Splitlab (Wüstefeld et al. 2008) and SHEBA (Wüstefeld et al. 2010). Splitlab uses three standard techniques: the rotation-correlation method (RC; Bowman et al. 1987), the minimum energy method (SC; Silver et al. 1991) and the eigenvalue method (EV; Silver et al. 1991). This allows measurement classification as 'good', 'fair' or 'poor' according to the criteria of Wüstefeld and Bokelmann (2007). SHEBA uses the eigenvalue method alone and incorporates a cluster analysis algorithm, thus decreasing subjectivity in phase arrival picking (Wüstefeld et al. 2010). A total of 631 'fair' or 'good' measurements were made and subsequently stacked using the method of Wolfe and Silver (1998). This number includes high quality null results, which occur where the anisotropy is very weak, or aligned parallel or perpendicular to the initial polarization of the seismic wave (Wüstefeld and Bokelmann 2007). We used events with moment magnitudes greater than 6.0 and with epicentral distances of between 85 and 130 degrees. Teleseismic SKS and SKKS phases where utilized because their passage through the core as P-waves removes source-side anisotropic effects (Silver et al. 1991). Given that the lower mantle is approximately isotropic, the main splitting signal source observed in teleseismic studies is likely within the upper 400km of earth structure, directly beneath the seismometers (Silver et al. 1991).

The short deployment time of the OBS stations and small number of high quality splitting results obtained limits backazimuthal converge and makes it difficult to model this dataset with anything more complex than a single layer of anisotropy. Given this constraint, we chose not to include information about backazimuth in the stacking process.

Shear wave splitting of OBS data is complicated by the potential for component misorientation (e.g. Lodewyk et al. 2014). This arises because OBS instruments settle on the seabed in unknown orientations that must be determined after recovery in order to rotate the horizontal components into the true 'East' and 'North' directions. The horizontal orientations of the Cascadia Initiative and X9 stations were determined using the surface wave polarization method of J. Stachnik et al. (2012). The accuracy of the results was then checked during the splitting process by comparing initial polarization estimates to backazimuth directions and ensuring separation of approximately 0 or 180 degrees.

A further check on the orientations can be carried out by virtue of how the three methods

respond to misaligned components (Tian et al. 2011). It has been shown that EV and RC splitting time estimates are unaffected by component misorientation, whereas small inaccuracies in orientation introduce large errors for the SC method (Tian et al. 2011). Our measurements were only characterized as 'good' or 'fair' when there was satisfactory agreement between the delay time predictions of the three methods. SC method results are reported singularly in this paper because this technique has been determined to be least sensitive to noise and exhibits the highest accuracy proximal to null measurements (Wüstefeld and Bokelmann 2007).

High levels of long period noise are present in the OBS data (Bell et al. 2014, Webb 1998). Filtering was used to optimize noise reduction without unduly compromising the splitting measurements. The characteristic frequency of teleseismic SKS waves ranges between 0.08-0.13 Hz but most onshore studies utilize bandpass filters such as 0.02-0.20 Hz, which capture the full range of SKS energy (Riddihough 1984, Eakin et al. 2010). The presence of strong 0.16-0.2 Hz secondary microseismic noise peaks in the OBS data (Bell et al. 2014), however, means that such filter bands are not typically useful in this case. OBS data is further affected by strong compliance noise ranging from 0.01 - 0.04 Hz, attributed to infragravity waves (Webb 1998). This suggests an optimal filter band close to the 'noise notch' of 0.03-0.1 Hz, as identified by Webb (1998). Typically we choose a region of 0.05-0.15 Hz, but employ frequencies between 0.03 and 0.18 Hz on an event-by-event basis to optimize the signal-to-noise ratio (SNR). In order to limit subjectivity many events had their splitting parameters determined in multiple frequency bands and multiple time windows. Only events with SNR greater than 4.0 were used in the stack. Upper filter corner frequencies below 0.14 Hz were omitted to avoid signal energy reduction, which makes measurements appear increasingly null.

Geodynamic modeling

Our simple two-dimensional (2D) model of the mantle flow field beneath diverging plates was constructed as a test of our interpretation of the splitting geometry observed beneath the Gorda plate. The propagator matrix method for 2D periodic flow given in the appendix of Hager et al. (1981) was used to solve for instantaneous, incompressible, Newtonian viscous (Stokes) flow with piecewise-constant horizontal (plate) motions imposed at the top of the mantle. Solutions are obtained in Fourier series form with periodic boundary conditions horizontally. To approximate the situation along a profile perpendicular to the Gorda ridge, we model one plate as stationary while the other diverges at a constant speed (60 mm/yr). We focus on flow within a 400 km horizontal window centered at the velocity jump, and choose a horizontal periodic boundary condition whose fundamental length scale is much larger than this window length (Figure 2.3, bottom panel). We follow Richards et al. (2001) by assuming a two-layer structure featuring a thin, low viscosity and thick, underlying mantle layer. We base our viscosity contrast and layer thickness estimates (100km and a viscosity contrast of 100) on the work of Fjeldskaar (1994), although we acknowledge that the width and viscos-

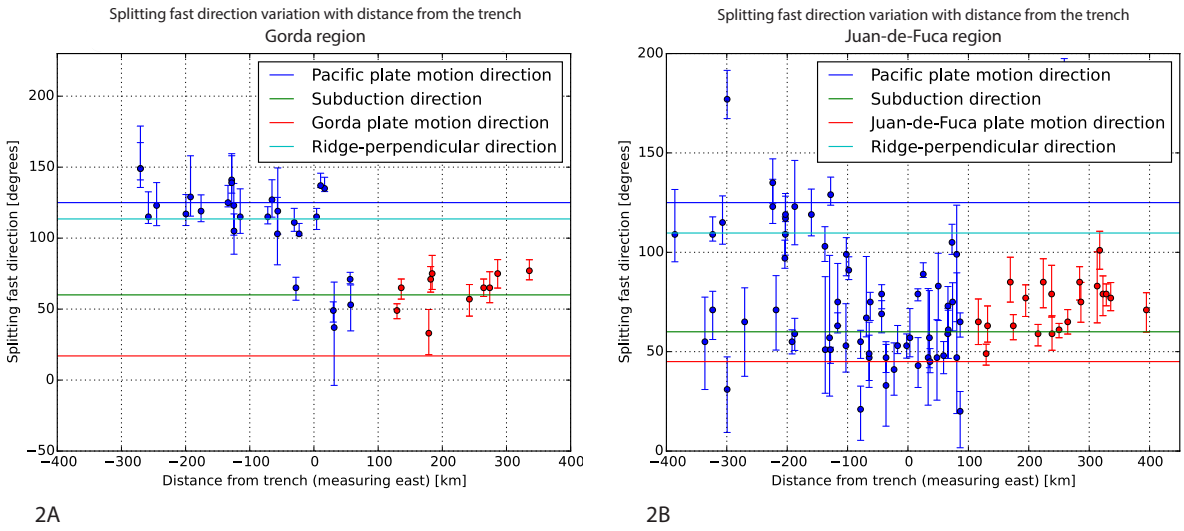

Figure 2.2: Two distinct patterns in the variation of splitting fast directions with distance from the trench. 2A displays results with latitudes between the Mendocino Triple Junction (MTJ) and the southern tip of the Blanco Fracture Zone. 2B shows sites between latitudes of the southern and northern tips of the Juan-de-Fuca ridge. In 2A, one population of splits lies west of the trench and is aligned with Pacific plate motion, while another aligns with the subduction direction. 2B shows continuous variation in splitting direction with trench distance. Blue and red markers indicate offshore and onshore results respectively. Error bars indicate the 95% confidence interval.

ity of the asthenosphere is poorly constrained. Recent seismic constraints, especially seismic anisotropy studies beneath the Pacific Plate (Nettles et al. 2008) , suggest strongly that the base of the highly anisotropic asthenosphere is at approximately 200 km depth, which is consistent with geodynamic constraints as long as the viscosity contrast is at least 2-3 orders of magnitude (Paulson et al. 2009). Thus, our choice remains somewhat arbitrary, although the thickness and viscosity parameters we employ reflect the findings of recent studies. Our model extends to 660km in depth, where the vertical flow field is set to zero at the bottom of the layer. Figure 2.3a shows our preferred model, where the asthenosphere viscosity is reduced by a factor of 100. The model does not account for complicated features such as the 3D plate geometry or the subduction zone, but clearly the weak asthenosphere causes flow to be induced immediately beneath the stationary plate that is strongly aligned with motion of the moving plate. We therefore propose that the large, fast-moving Pacific plate induces asthenospheric flow beneath the small, fragmented, slow-moving Gorda plate that is strongly aligned with Pacific plate motion, as observed.

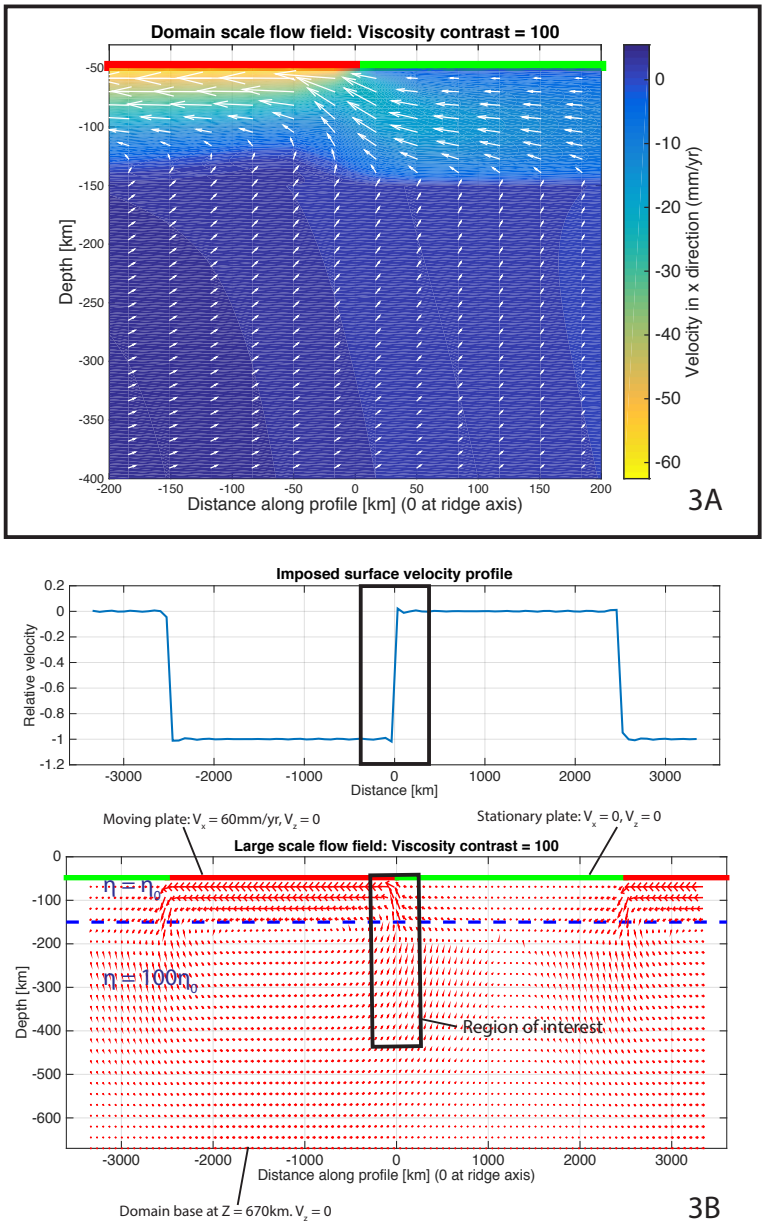

Figure 2.3: Two-dimensional modeling to simulate mantle flow below the Gorda plate as induced by motion of the Pacific plate. The green plate is stationary while the red plate moves to the left at 60 mm/yr. This approximates the situation in profile perpendicular to the Gorda ridge. The setup consists of an 'asthenosphere' from 50-150 km and an 'mesosphere' below. In our preferred model (3A), the viscosity of the mesosphere is 100 times that of the asthenosphere. 3B shows details of the model set-up, including the imposed periodic surface velocity field, region of interest and large scale induced flow structure. The motion of the red plate is seen to generate flow beneath the adjacent stationary plate.

2.4 Results

The TA stations produce a uniform splitting pattern along the length of the subduction zone (Figure 2.1. The mean fast direction and delay times are N72°E and 1.34 s respectively, in agreement with previous studies and sub-parallel to the subduction direction of N60°E (Currie et al. 2004, Eakin et al. 2010). Offshore stations on the Juan-de-Fuca plate display a more complicated pattern: except for a single, ridge-parallel result near Cobb Hotspot, fast splitting directions (FSD) vary between the trench perpendicular and absolute plate motion (APM) direction. Alignment with the Juan-de-Fuca APM direction increases towards the trench (Figure 2.2). The FSD then rotate into the subduction direction as one moves onshore.

Sites on the Gorda plate produce a highly uniform pattern, but are neither aligned with Gorda APM nor the subduction direction. Their mean FSD of N66°W aligns with the motion of Pacific plate ($\sim$ N57°W; Currie et al. 2004) and with the ridge-perpendicular orientation ($\sim$ N67°W). A marked change in FSD is observed just east of the trench in this region, where the fast directions rotate approximately 70°into a trench-perpendicular orientation (Figure 2.2). Results from stations situated on the Pacific plate align well with APM, featuring a mean direction of N60°W.

This study compliments previous shear wave splitting results from ocean basins and enhances coverage of the region. A notable feature of the existing onshore pattern is the arcuate splitting geometry observed south of the MTJ in northern California, which follows the southern edge of the down-going Gorda slab (Eakin et al. 2010; Zandt et al. 2008) (Figure 2.1). The subducting slab is imaged by body wave tomography as a segmented, high velocity anomaly with a 'gap' beneath northern Oregon (Zandt et al. 2008). This 'gap' does not appear to influence the splitting pattern, however.

2.5 Discussion and interpretations

Limited back-azimuthal coverage makes it difficult to model dipping or multi-layer regional anisotropy in our study. We follow previous teleseismic splitting studies (Currie et al. 2004; Eakin et al. 2010) of this area in interpreting a single anisotropic layer.

On oceanic plates, the dominant splitting signal likely arises from a combination of fossil anisotropy in the lithosphere and viscous shearing of the asthenosphere by plate motion (Silver et al. 1991). According to the model of Nishimura et al. (1989), the lithospheric component should lie in the fossil spreading direction, while the asthenospheric component should align with the direction of present day mantle flow. Both are parallel to the spreading direction close to mid-ocean ridges, but diverge beneath older lithosphere as the asthenosphere is dragged in to the APM direction (Nishimura et al. 1989). Shear wave splitting studies of the East Pacific Rise (Wolfe and Solomon 1998) and in French Polynesia (Fontaine et al.

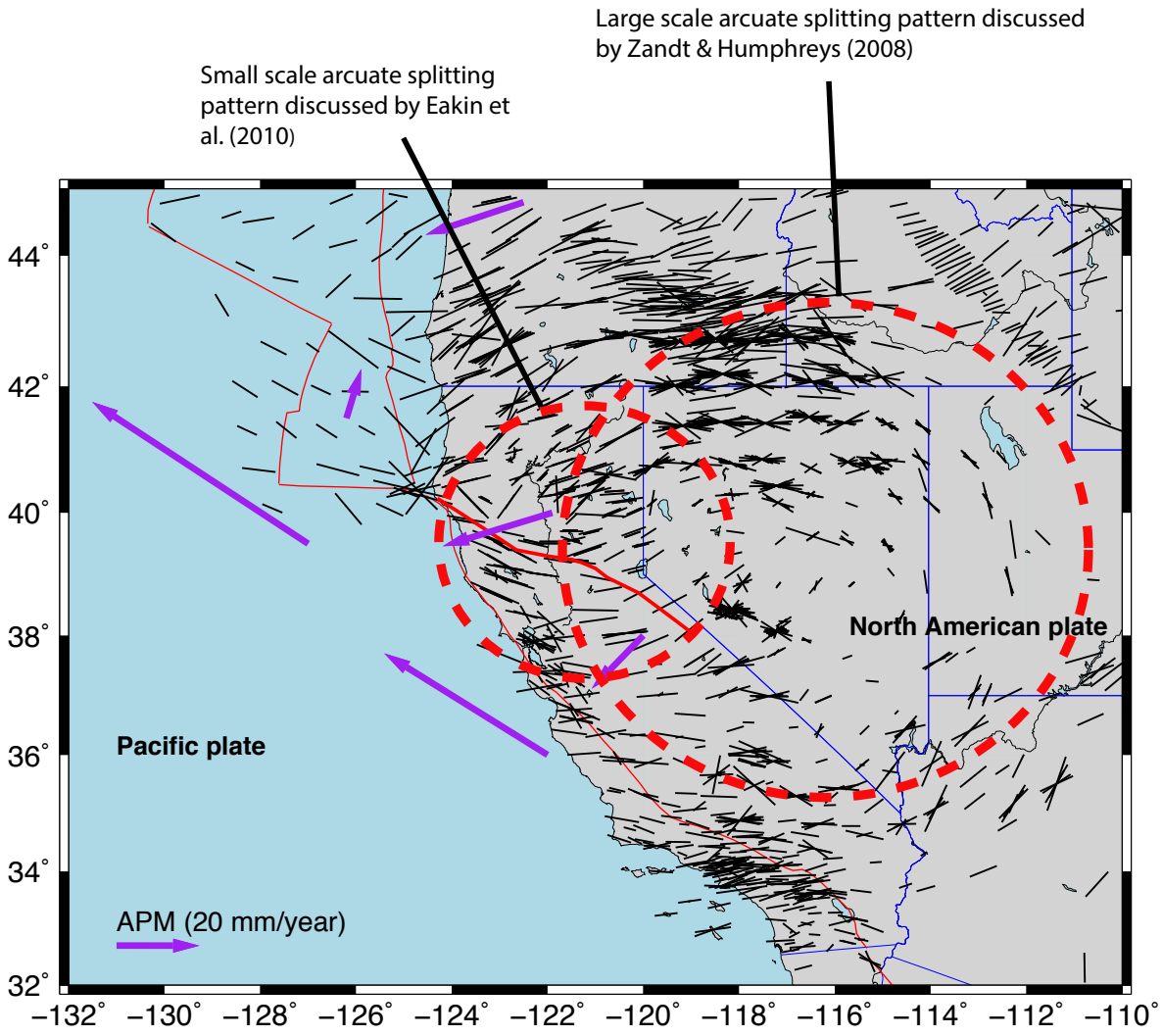

Figure 2.4: This map highlights two arcuate splitting patterns observed near the edge of the downgoing Gorda slab. The first, a large-scale feature centred on Nevada, was interpreted to be the result of mantle flow around the edge of the slab by Zandt et al. (2008). Eakin et al. (2010) interpreted the second, a smaller scale pattern centred on Northern California, in the same fashion. Given our splitting observations on Gorda and the findings of our geodynamic model, we suggest that the second, small-scale pattern could mainly be the result of Pacific plate motion. Indeed, there are likely two layers of mantle flow near the slab edge: One, a shallow asthenospheric flow influenced by the motion of the fast-moving Pacific plate and two, a deeper, actuate flow around the slab edge that is driven by rollback.

2007) generally support this idea.

Given realistic estimates of 50 km, 4 % and 4.6 km/s for the thickness, percentage anisotropy, and shear wave velocity for the Juan-de-Fuca plate, respectively, a lithospheric splitting time contribution of 0.43 s is predicted (Silver et al. 1991, Eakin et al. 2010). This is significantly smaller than the OBS splitting times, implying that the asthenosphere is an important source of anisotropy.

The rotation of fast splitting directions into the APM orientation east of the Juan-de-Fuca ridge implies the influence of competing flow components. A variety of anisotropic fabrics might be expected in the vicinity of a mid-ocean ridge: upwelling asthenosphere in response to passive spreading, oriented melt pocket anisotropy along the ridge itself due to dyke intrusion (Kendall et al. 2005), lateral flow away from the ridge (Blackman et al. 1997) and basal drag fabrics as the plate moves away from the ridge (Nishimura et al. 1989).

Splitting directions close to the Juan-de-Fuca ridge generally lie between APM and the ridge-perpendicular direction, suggesting that lateral flow and basal drag are the strongest influences. We do not see a concentration of null results at stations located close to the ridge, suggesting that the influence of vertically oriented LPO due to upwelling is minimal or confined to a narrow region.

One exception to the pattern occurs at site J39, just east of Axial Seamount. The splitting parameters here are well constrained and suggest strong ridge-parallel anisotropy. This may be the result of aligned pockets of melt present near the ridge axis as observed on land in Ethiopia, a subaerial region of incipient oceanic spreading (Kendall et al. 2005).

On the Gorda section of the plate system there is no significant variation in FSD with distance from the ridge. The FSD are instead well aligned with the direction of Pacific plate motion and with results from the Pacific plate west of the Gorda ridge and south of the Mendocino Fracture Zone. This implies that asthenospheric flow beneath the Gorda plate, west of the trench, is determined by the regional pattern of shearing induced by the north-westward motion of the Pacific plate, which moves at ~ 60 mm/yr (Gripp et al. 2002). An alternative suggestion posits that because flow in this region is ridge perpendicular, it is driven primarily by spreading of the Gorda ridge. This is less likely given the apparent limited influence of the faster-spreading Juan-de-Fuca plate on the splitting pattern to the north. The splitting geometry on Gorda does not suggest major contributions from motion of the plate itself or rollback of the trench, which operates at less than half the speed of the Pacific plate.

The uniform, subduction-parallel splitting pattern seen on the North American plate east of the trench is interpreted as a consequence of entrained mantle material beneath the down-going slab. Fossil anisotropy in the continental lithosphere and subducted slab has been

shown to be insufficient to explain the observed high delay times (Eakin et al. 2010), thus implying an asthenospheric source. Furthermore, the mantle wedge is thin or non-existent within most of study area, so the only region thick enough to produce delay times commensurate to those observed is the sub-slab mantle (Riddihough 1984, Eakin et al. 2010). Nevertheless, onshore FSD tend towards North American APM at great distances from the trench (Figure 2.2b), suggesting some influence from plate-motion induced flow in the mantle wedge, or from lithospheric anisotropy. There is no significant change in delay times, however.

Immediately east of the trench on Juan-de-Fuca plate, splitting geometry rotates smoothly from an APM-parallel direction into a trench-perpendicular direction. This is indicative of entrained easterly flow beneath the slab. In contrast, across the Gorda-North America plate boundary there is a sharp change in FSD (Figure 2.2). This is difficult to justify with a single layer interpretation because it would imply dramatic changes in flow direction. Instead, this region could host two layers of mantle flow: A shallow layer induced by motion of the Pacific plate and a deeper layer related to entrainment by the subducting slab.

Our observation provides a test for the models of Conrad et al. (2007) and Debayle et al. (2013), which suggest that plates moving slower than 40 mm/yr (Debayle et al. 2013) and within 500 km of a constructive plate margin1 are less able to influence asthenospheric flow. Both Gorda and Juan-de-Fuca meet these criteria, so the observation that Juan-de-Fuca does affect the asthenosphere perhaps sets lower bounds on the age and speed of a tectonic plate that can induce asthenospheric flow.

The Gorda plate is young ($<$ 10 My; Chaytor et al. 2004), has a low absolute velocity (Gripp et al. 2002), is undergoing internal deformation (Chaytor et al. 2004) and may have had its current APM for less than 2 Ma (Chaytor et al. 2004). In contrast, the neighboring Pacific plate is large, intact and fast moving. We have constructed a 2D model of this situation using the method of Hager et al. (1981) to show that Pacific plate motion is capable of generating westward flow beneath the width of the Gorda plate, assuming that flow is largely confined to the uppermost mantle within a thin, low viscosity asthenosphere (viscosity contrast 100, channel thickness 100 km, from Fjeldskaar (1994) beneath Gorda. This simple model demonstrates the plausibility of our interpretation of the splitting pattern (Figure 2.3).

This leads to discussion of the arcuate spitting geometry observed south of the MTJ and interpreted as flow forced eastwards around the slab edge by rollback (Eakin et al. 2010). This pattern, however, could be asthenospheric flow induced by drag from the N60°W drifting Pacific plate. A larger scale arcuate splitting pattern, situated much further east, may instead be the result of deep toroidal flow around the slab edge, which extends below 400 km in this region (Figure 2.4)

In summary, we propose that the splitting observed on the Juan-de-Fuca plate system is mainly the result of APM-driven asthenosphere flow. At depth, below the Cascada fore-arc, the downgoing slab entrains underlying mantle material. West of the subduction zone, the Juan-de-Fuca plate is sufficiently large and fast moving to influence mantle flow geometry while the Gorda plate is not. Flow directly beneath Gorda is instead induced by Pacific plate motion. This places bounds on the size of plate capable of inducing asthenospheric flow.

2.6 Concluding remarks

This chapter leverages data from the Cascadia Initiative, a large, community driven deployment of seismometers (OBS) spanning the entirety of the Juan-de-Fuca plate system from ridge to trench and then onshore in Californian, Oregon and Washington state (Figure 2.1). Teleseismic shear wave splitting is used to investigate the geometry of seismic anisotropy beneath this region, which is in turn used to infer the pattern of asthenospheric flow and interaction with the subducting Juan-de-Fuca plate. The noise characteristics of data collected from ocean bottom seismometers make shear wave splitting analysis in this setting particularly challenging, requiring careful data quality assessment and consideration of component misorientations. However, our results appear robust and are corroborated by the similar study of Bodmer et al. (2015). We find the direction of seismic anisotropy to be subparallel with plate motion beneath the Juan-de-Fuca plate and onshore, implying a layer of entrained asthosphere beneath the subducting slab. However, splitting fast directions beneath the smaller, internally deforming Gorda plate are oriented in the direction of motion of the adjacent Pacific plate, suggesting that the latter controls asthensopheric flow in this region. To test this interpretation we construct a simple, two-dimensional geodynamic model that approximates this situation by modelling the Gorda plate as stationary and the Pacific plate as diverging at 60mm/yr. Given reasonable estimates for the viscosity profile of the mantle, we find that drag from the Pacific plate is capable of generating westwards flow beneath the entirety of the Gorda plate, thus offering support for our seismic interpretations. This work demonstrates the power of combining the strengths of seismic and geodynamic approaches to investigate mantle dynamics, and could provide the building blocks for a more sophisticated three-dimensional model of mantle flow beneath Cascadia that uses slab geometry as inferred from seismic tomography as an input density structure, for example.

A full published version of this paper can be found at https://doi.org/10.1038/ngeo2569.

2.7 Chapter acknowledgments

The data used in this research was provided by instruments from the Ocean Bottom Seismograph Instrument Pool (http://www.obsip.org), which is funded by the National Science

Foundation under cooperative agreement OCE-1112722. The facilities of IRIS Data Services, and specifically the IRIS Data Management Center, were used for access to waveforms, related metadata, and/or derived products used in this study. IRIS Data Services are funded through the Seismological Facilities for the Advancement of Geoscience and EarthScope (SAGE) Proposal of the National Science Foundation under Cooperative Agreement EAR-1261681. The work benefited from discussions with J. Lodewyk, A. Frassetto and C. Eakin. We also thank the editor and three anonymous reviewers for their helpful comments. GMT (Wessel et al. 1998) and MATLAB where used to create the figures.

Chapter 3

Subduction geometry beneath south-central Alaska and its relationship to volcanism[1]

Advisor: Richard M. Allen

Coauthor: Ian Bastow

3.1 Chapter summary

The southern Alaskan margin captures a transition between compression and strike-slip dominated deformation, accretion of the over-thickened Yakutat terrane, termination of Aleutian arc magmatism and the enigmatic Wrangell Volcanic Field. The extent of subduction and mantle structure below this region is uncertain, with important implications for volcanism. We present compressional- and shear-wave mantle velocity models below south-central Alaska that leverage a new seismometer deployment to produce the most complete image of the subducting Pacific-Yakutat plate to date. We image a steeply-dipping slab extending below central Alaska to $>$ 400km depth, which abruptly terminates east of $\sim$ 145°W. There is no significant slab anomaly beneath the nearby Wrangell volcanoes. A paucity of volcanism is observed above the subducting Yakutat terrane, but the slab structure below 150km depth and Wadati-Benioff zone here are similar to those along the Aleutian-Alaska arc. Features of the mantle wedge or overlying lithosphere are thus responsible for the volcanic gap.

[1]Published as MartinShort, R, et al. Subduction geometry beneath south central Alaska and its relationship to volcanism. Geophysical Research Letters 43.18 (2016): 9509-9517.

3.2 Introduction

South-central Alaska, at the northeastern vertex of the Pacific plate, displays a so-called 'corner geometry' (Eberhart-Phillips et al. 2006). Here, the Pacific plate is bounded to the east by the Queen Charlotte/Fairweather transform system and to the north by the Alaska-Aleutian subduction zone (Figure 3.1: e.g. Plafker et al. 1994; Eberhart-Phillips et al. 2006). Subduction began in the Late Cretaceous, with consumption of the Kula plate. This was followed by subduction of the Pacific plate, after its capture of Kula at 40-45 Ma (Madsen et al. 2006). This long history of subduction has resulted in growth of northwestern North America though the accretion of oceanic and island arc terrains to form what is now south-central Alaska (Plafker et al. 1994).

Today, the strike of the Alaska-Aleutian subduction zone rotates from approximately normal to plate motion in the central Aleutians into an oblique orientation below Alaska, where it appears to terminate (Ratchkovski et al. 2002). The situation is further complicated by the presence of the Yakutat terrane, a region of thick (>20km) oceanic crust that lies at the eastern terminus of the subduction zone and is in the process of being accreted to the Alaskan margin (Plafker et al. 1994). Convergence of the Yakutat terrane is believed to be responsible for many unusual features of the subduction zone beneath south-central Alaska. These include the very shallow Wadati-Benioff Zone (WBZ) out to 600km from the trench, broad intraplate deformation, rapid uplift of the Chugach and Alaska ranges and a paucity in volcanism above the inferred subducted extent of the Yakutat terrane, known as the Denali gap (Eberhart-Phillips et al. 2006; Plafker et al. 1994; Wang et al. 2014; Nye 1999). High resolution imaging of the mantle below the Denali gap and the adjacent volcanogenic arc is required to better understand the differences in slab geometry and extent between them.

Another unusual feature of south-central Alaska is the Wrangell Volcanic Field (WVF), a group of volcanoes that lie close to the eastern edge of the subducting Yakutat terrane (Figure 3.1). These volcanoes extend $\sim$ 200km from the Alaska-Yukon border. They exhibit a northwestward progression in activity, commencing $\sim$ 26Mya and subsiding since $\sim$ 0.2Mya (Richter et al. 1990; Finzel et al. 2011). Given the scarcity of earthquake activity below 50km depth beneath the WVF, the existence of a subducting slab beneath this area and its relationship to volcanism have become topics of significant debate. The tomographic study of You et al. (2012) suggests the presence of a deep slab beneath the WVF, implying a connection between magmatism and slab dehydration. Alternatively, the geodynamic work of Jadamec et al. (2012) suggests that WVF volcanism might instead be driven by toroidal flow and mantle upwelling around a more easterly slab-edge. Such a feature would be expected to produce a near-vertical, low velocity anomaly below the WVF, but seismic tomography images of the region to date are either of insufficient depth-extent (e.g. Wang et al. 2014) or data coverage (e.g. Qi et al. 2007) to illuminate it.

Although the shallow structure below south-central Alaska is relatively well imaged, the

geometry of the deep slab (below 100km), its potential relationship to volcanism in the WVF and its role in the creation of the Denali gap are poorly known. Here we present teleseismic P- and S-wave models of south-central Alaska, which provide the most complete image of the deep slab structure to date. We are able to confidently image a steeply dipping Pacific-Yakutat slab down to below 400km depth, observe a sharp termination of the subduction zone and see no evidence for a deep slab beneath the WVF. Despite being hinted at by previous studies, these findings have only been made possible by the recent deployment of Transportable Array (TA) seismometers in Alaska, which has significantly expanded network coverage and hence increased the size of the region that we can confidently image with tomographic techniques. Thus, our study represents some of the first scientific findings in this major community effort to understand the seismotectonics of Alaska.

3.3 Background and previous studies

Initial studies of the crustal and mantle structure in Alaska made use of the region's abundant seismicity to investigate the geometry of the subducting plate (e.g. Page et al. 1989; Ratchkovski et al. 2002). Local seismicity has also been used in body wave tomography studies, which have focused mainly on the shallow structure of the slab, mantle wedge and continental crust (e.g. Zhao et al. 1995, You et al. 2012). The subducting Pacific-Yakutat plate is consistently imaged as a dipping, high velocity structure, whose upper surface is delineated by intense seismic activity to $\sim$ 150km depth (Eberhart-Phillips et al. 2006). The dip of the down-going slab shallows beneath the Denali gap (Figure 3.1: e.g., Hayes et al. 2012). Furthermore, a distinct, thin ($<$ 20km), low velocity layer is imaged directly above the high velocity slab in this region, with seismicity occurring solely within this feature (Ferris et al. 2003; Eberhart-Phillips et al. 2006). Rondenay, Abers, et al. (2008) report that the low velocity layer appears to become thinner with depth, and disappears below 150km. It is interpreted to be the thick, hydrated, Yakutat crust, which undergoes dehydration and phase transformation to eclogite at depth (Hacker et al. 2003). The 15-20km thickness of this layer, as inferred from the images of Rondenay, Abers, et al. (2008), is in excellent agreement with Yakutat crustal thickness estimates from offshore reflection studies (Christensen et al. 2010; Worthington et al. 2012).

The Yakutat terrane likely formed as an oceanic plateau offshore of the American Pacific Northwest, and has since been rafted into its present location by motion of the Queen-Charlotte/Fairweather fault system (Worthington et al. 2012). Convergence of this thick oceanic crust has been ongoing for at least 23 Ma (Finzel et al. 2011), during which time it has penetrated over 600km inland of the trench (Eberhart-Phillips et al. 2006). Figure 3.1 shows the striking correlation between the subducted Yakutat region and the 400km long 'gap' in volcanism from Hayes Volcano to Buzzard Creek Maars, known as the Denali volcanic gap (Nye 1999). It is likely that shallow subduction of thick, buoyant, Yakutat crust is responsible for this phenomenon. However, the exact causes of the Denali gap are not well

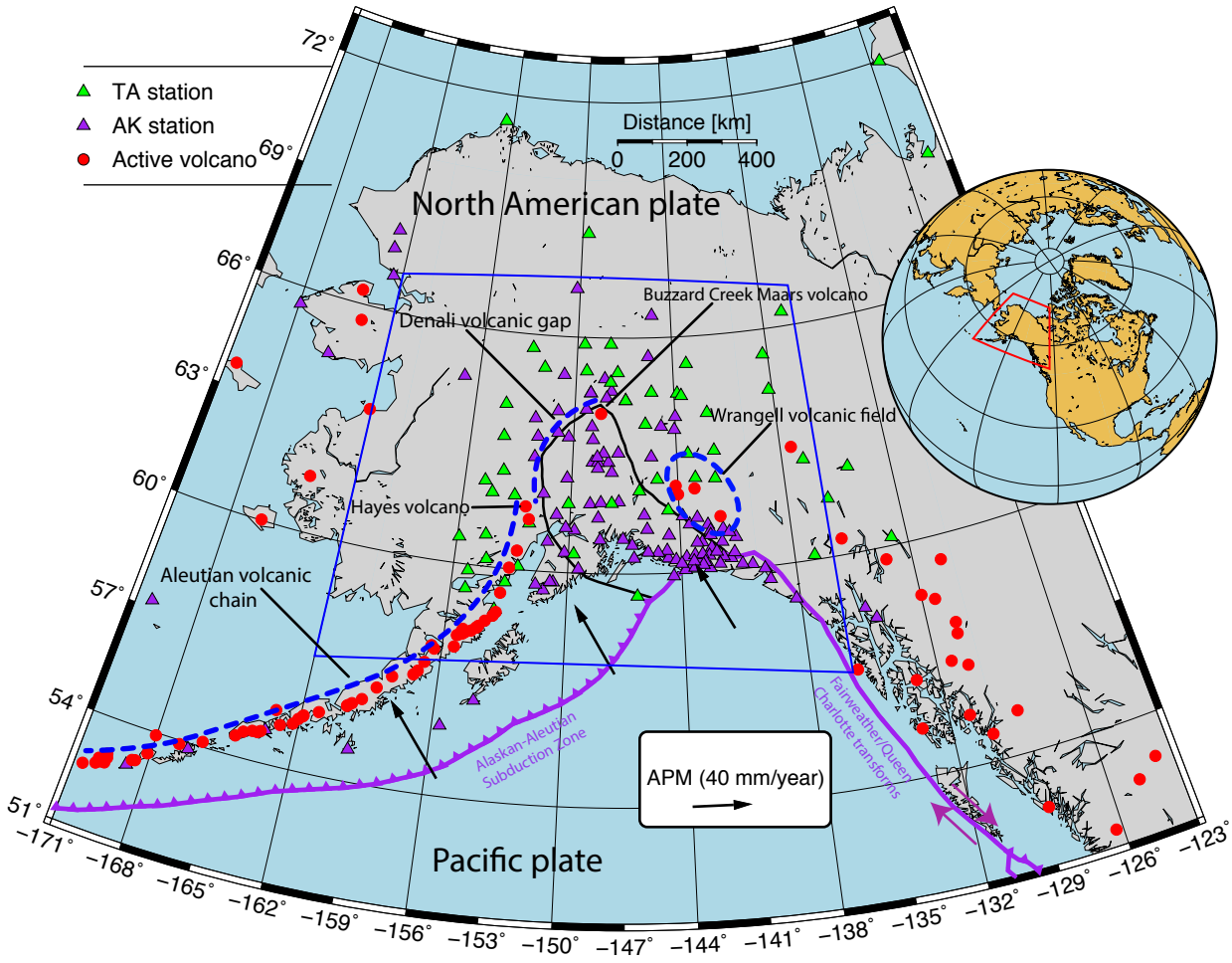

Figure 3.1: Map showing the distribution of broadband seismometers used in this study (triangles). A total of 158 stations were used in this study. The black line indicates the extent of the subducted Yakutat crust as inferred by Eberhart-Phillips et al. (2006). Red dots indicate sites of Holocene volcanic activity, while purple lines indicate plate boundaries (Bird 2003). Black arrows indicate the direction and magnitude of absolute plate motion (APM) from Gripp et al. (2002). The blue box outlines the extent of the maps shown in Figure 3.5.

understood, in part because the slab here does not lie flat against the continental lithosphere and the mantle wedge below the volcanic gap appears suitable for melt production (Rondenay et al. 2010).

Magmatism at the WVF has been the subject of multiple petrological and tectonic studies. Lavas sampled from this region feature alkaline, transitional and calc-alkaline affinities, suggesting a range of contributing sources (Skulski et al. 1991). The oldest eruptive centers, which lie in the southeast, feature mainly alkaline and transitional lavas. Those in the northwest feature lavas with a transitional and calc-alkaline affinity, from which various studies have inferred the presence of a subducting slab at depth beneath the region (e.g. Page et al. 1989; Skulski et al. 1991). However, the presence of adakite lavas at Mounts Drum and Churchill has also been used to argue for flat subduction and slab melting beneath the WVF (Preece et al. 2004).

Tomographic imaging studies of the type previously used to image the aforementioned regions generally make use of local events, thus constraining only the relatively shallow (<100km) velocity structure; there have been relatively few teleseismic studies. Using surface-wave tomography, Wang et al. (2014) imaged the slab as an elongate, high velocity anomaly with abrupt termination at $\sim$ 64°N, 146°W. However, their technique only provides good resolution above 200km depth. Qi et al. (2007) produced a teleseismic P-wave mantle velocity model for the region that reveals structure to 700km depth, but used a much sparser seismic network than is available today.

3.4 Tomography methodology

The models presented here are produced using the method of finite frequency, travel-time tomography, featuring the joint inversion of two frequency bands for P-waves and one for S-waves. The workflow is similar to that employed for the 'Dynamic North America' (DNA) models (Obrebski et al. 2010; Obrebski et al. 2011; Porritt et al. 2014). The waveforms of earthquakes with Mw > 6.0 and epicentral distances of 30-120°from the center of the array were obtained for the period January 2014 to June 2016. This yielded 288 earthquakes recorded at up to 158 stations (Figure 2.1). The data were instrument-corrected and rotated into the tangential-radial-vertical coordinate frame: P-wave arrival times were picked on the vertical component and S-waves on the tangential. Following the aforementioned DNA model series, travel time residuals were calculated with reference to the IASP91 travel-time tables (Kennett et al. 1991) and refined using the multichannel cross correlation method of VanDecar et al. (1990). Refined delay times were determined for frequency bands of 0.02-0.1Hz and 0.9-1.2Hz for the P waves, and 0.02-0.1Hz for the S waves. These filter bands produce the highest signal to noise ratio, based on visual inspection of the waveforms. In our tomography workflow, the travel time sensitivity of the wavefield for each event is approximated using finite frequency kernels calculated using the paraxial method of Hung et

al. (2001), which provide a better representation of the three-dimensional (3D) wavefield than infinite-frequency rays (Hung et al. 2001; Maceira et al. 2015). The kernels and delay times are then assembled into a linear system, which is solved using the method of damped least squares. A model of velocity perturbations is then recovered. Our method simultaneously inverts for a vector of slowness perturbations at each of the grid cells, plus station and event static corrections.

The station corrections attempt to account for heterogeneity in the velocity structure of the crust and upper mantle, which is poorly resolved in teleseismic tomography due to the high incident angles of incoming rays at shallow depths and thus the lack of crossing raypaths. Station corrections thus absorb the travel-time effect of shallow structure beneath the instruments and consequently prevent this poorly resolved structure from generating artifacts in the model. The event corrections are required to account for differences in the mean travel-time between each event and the station. The cross-correlation algorithm of VanDecar et al. (1990) forces the mean of the optimized delay times associated with each station to be zero. However, because of heterogeneities in the model box, the mean travel-time residuals of the event-station paths are not equal across events. Thus a correction associated with each event must be added to ensure that the zero delay-time sum condition imposed by the algorithm of VanDecar et al. (1990) does not generate artifacts in the model.

The model grid is defined over a spherical cap spanning 166.3°W/53.0°N to 115.7°W/71.0°N, with a latitudinal node spacing of 0.28°, a longitudinal spacing of 0.8°and a vertical spacing of 15km. The grid extends from the surface to 1000km depth. The volume encompassed by our grid is much larger than the region where we expect to have good resolution: This corresponds to the region covered by the main cluster of stations, to $\sim$ 500km depth. The number of crossing raypaths is limited at greater depths.

3.5 Resolution tests

We test the resolving power of our dataset in two ways: firstly, a standard checkerboard test employed with progressively smaller checkers to determine the characteristic length scale of the smallest recoverable anomalies (Figure 3.2), and a 'synthetic slab' test (Figure 3.3, 3.4). Normally-distributed errors with standard deviation 0.1s are added to the synthetic travel-time data, which are then inverted using the same regularization scheme as for the observed data.

The checkerboard tests indicate that our P- and S-wave models have good resolution of features on the scale of the subducting slab to $\sim$ 400km depth. Resolution is best beneath south-central Alaska and quickly depreciates towards the edges of the seismometer array. Good recovery of features with lateral scales of 100km is seen in the models at 100km depth, and this transitions to a recovery of features with lateral scales of $\sim$ 300km at 400km depth

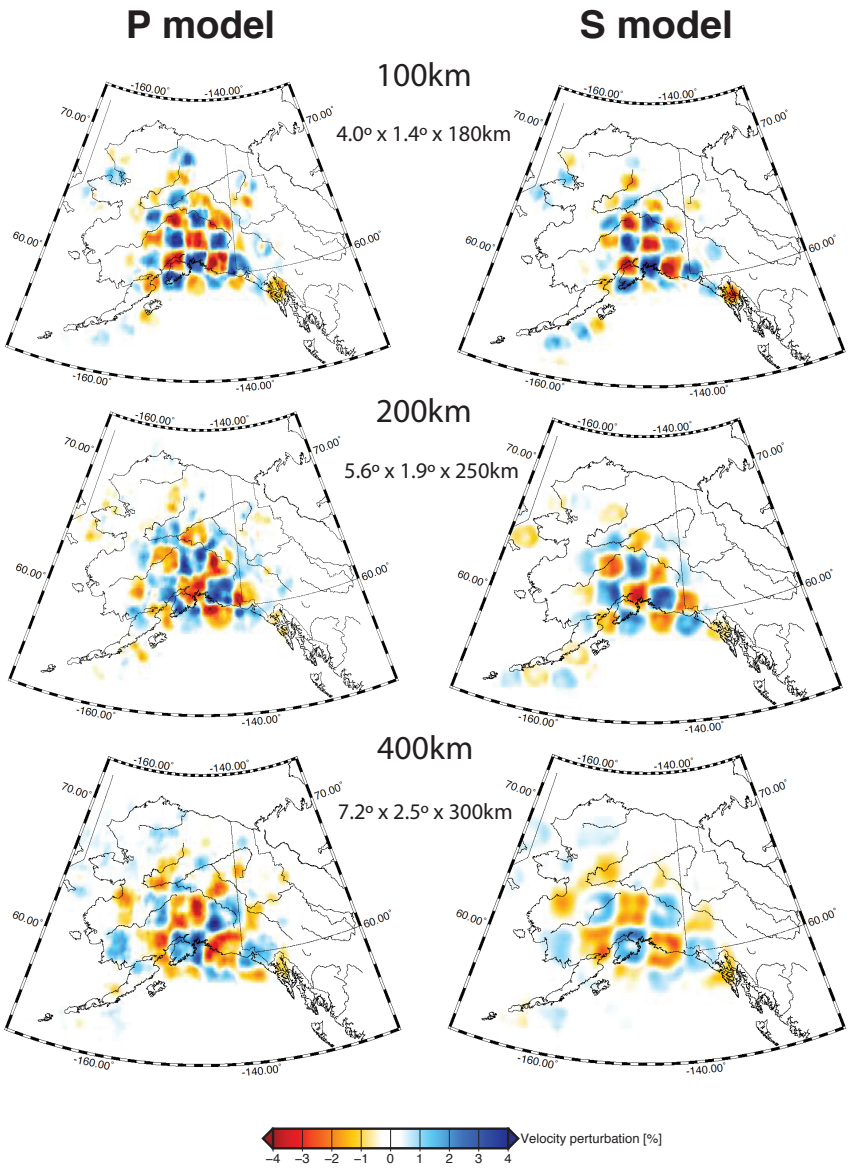

Figure 3.2: Checkerboard resolution tests indicating the spatial resolution of our tomographic models at the depths at which they were interpreted. In both cases, a synthetic grid of approximately cubic anomalies with velocity perturbations of +/- 4% was created, travel time residuals for the utilized station-event pairs were calculated and the inversion was run with the same regularization scheme as with the real data. The images shown approximately represent the smallest checkerboard elements that can be adequately resolved at depths of 100km, 200km and 400km. The dimensions of the checkers are reported in degrees longitude/degrees and latitude/depth. These tests indicate that features on the scale of the subducting Pacific-Yakutat slab can be resolved in our models below south-central Alaska.

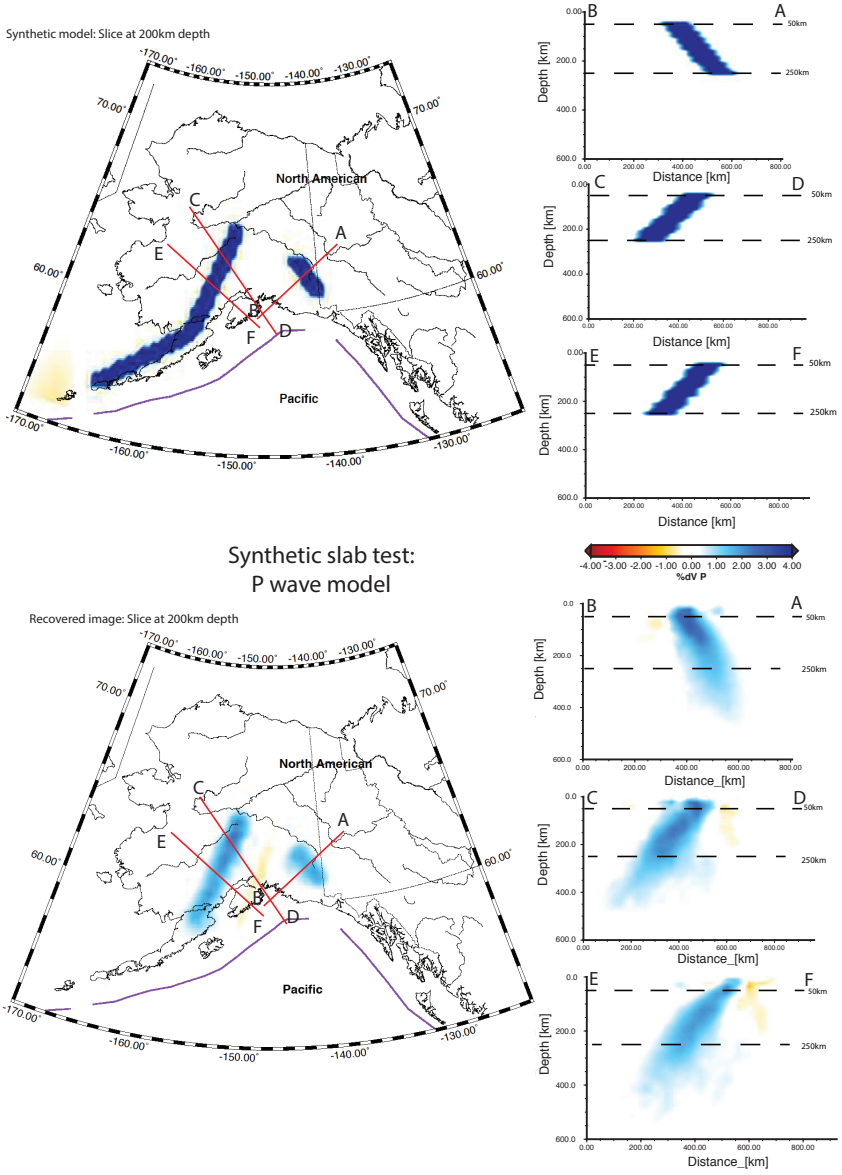

Figure 3.3: Synthetic slab test for the S wave model. A dipping, 100km thick, 'slab-like' anomaly extending from 50 to 250km depth and with a velocity perturbation of +4% was generated as shown in the upper image. Travel-time residuals for this structure were then calculated and the inversion procedure was run. The pattern of recovered anomalies is shown in the bottom panel. We achieve good recovery of the anomalies beneath the Wrangell volcanoes and central Alaska, which suggests that we are indeed capable of resolving features on the scale of the subducting slab. There is some smearing of the high velocity anomaly down-dip beyond the furthest extent of the synthetic anomaly, which suggests that we must be cautious about interpreting the maximum depth of the real slab observed in our models.

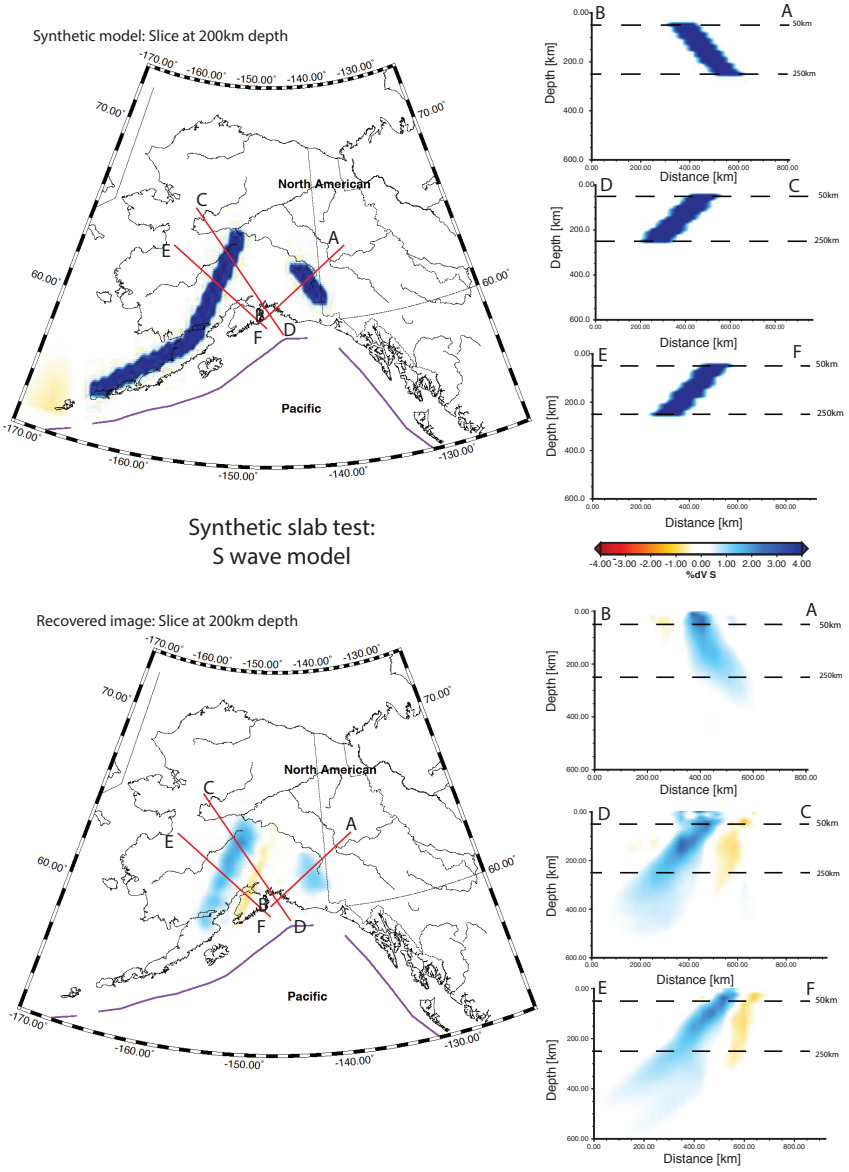

Figure 3.4: Synthetic slab test for the P wave model. The pattern of synthetic slabs is exactly the same here as in the S-model tests (Figure 3.3. Once again we invert the synthetic traveltime residuals using the same regularization scheme as was used in the real P wave model in order to asses the model's ability to recover anomalies on the scale of the Pacific-Yakutat and Wrangell slabs. Anomalies recovered by the P wave inversion process are generally slightly stronger and better defined than those from the S wave model owing to the inclusion of higher frequency data. However, for the purposes of this study the resolving capability of the two models is very much the same.

(Figure 3.2).

The synthetic slab tests are created using three, 100km thick artificial anomalies of +4%, which dip at 50°, terminate at 250km depth and strike in the approximate orientation expected for the Pacific-Yakutat-Wrangell slab (e.g. Jadamec et al. 2012). The along-strike extent of the synthetic slab east of Cook Inlet is successfully recovered, implying that our dataset is able to image slab-like features with minimal along-strike smearing in the region of greatest tectonic interest: That is, the transition between the Aleutian Island arc into the Denali gap, the Yakutat subduction region and the mantle beneath the WVF. Importantly, these synthetic tests suggest that if a deep slab were present beneath the WVF, we would resolve it (Figures 3.3 and 3.4).

3.6 Results

We present our P and S-wave velocity perturbation models in a series of depth slices (Figure 3.5) and cross sections (Figure 3.6). The most striking feature of our models is the presence of an elongate, dipping, high velocity feature that extends northeastwards from Cook Inlet into central Alaska, where it terminates abruptly. This is interpreted to be the subducting Pacific-Yakutat slab. The slab is known to continue further west below the Aleutian Island arc but is not seen in our model because of the lack of resolution in that region, as indicated by the synthetic tests.

The strike of the slab-related anomaly is only subparallel to that of the trench, meaning that it advances inland of the trench from west to east. The strike of this feature exhibits excellent alignment with the northwestern edge of the of subducted Yakutat crust, and it terminates just to the northeast of the northernmost extent of Yakutat subduction (Figure 3.5). Furthermore, the slab anomaly is well aligned with the WBZ, which provides strong support for our interpretation of it as subducting lithosphere (Figure 3.5).

Along the northernmost section of the slab, beneath the Denali gap, seismicity extends to a maximum depth of approximately 150km. However, our models indicate that the slab continues to a much greater depth, likely below 400km (Figure 3.5). This is consistent with the regions long history of subduction, and with the earlier tomography study of Qi et al. (2007). West of the Denali gap the WBZ extends slightly deeper, and the slab is also seen to depths of $>$ 400km.

At its northeastern-most corner, the high velocity anomaly associated with the slab extends to about 150km beyond the furthest extent of the seismicity (Figure 3.5a). This is a surprising finding given the apparent strong connection between seismic activity and slab presence elsewhere in the region. The feature was also highlighted by the teleseismic surface wave tomography study of Wang et al. (2014), and its presence in our body wave tomography

supports their assertion that the Pacific-Yakutat slab extends further northeast than predicted based on the WBZ alone. A further surprising finding is the presense of high velocity anomalies in the mantle wedge below the Denali gap (Figure 3.6a): These anomalies are not present below the volcanic arc west of the Yakutat terrane.

The profile of the slab changes along strike (Figure 3.6). Below the Denali gap, it is shallow for approximately 500km between the trench and the northwestern edge of the subducted Yakutat terrane, where it lies at a depth of about 150km (Figure 3.6). Beyond this, the deep slab exhibits a much steeper dip. Furthermore it becomes increasingly steep towards the northeastern-most edge, where it is almost vertical (Figure 3.3; Figure 3.6). Below the volcanic region, the slab exhibits a similar profile in both P- and S- wave profiles, but with a shorter zone of shallow subduction and a more gradual transition into a steep subduction at depth (Figures 3.5 and 3.6)

Figure 3a demonstrates that the Wrangell volcanoes are not underlain by a deep, high velocity structure. Our resolution tests (Figures 3.2-3.4) suggest that if such a feature were present, it would be clearly imaged. Thus, we can confidently state that there is an abrupt and significant change in upper mantle velocity structure between the Denali gap and the WVF.

3.7 Discussion

Our models provide new constraints on the geometry of the deep slab beneath Alaska, its relationship with the Denali volcanic gap and its proximity to the WVF. In the following section, we examine each of these regions in turn and make new tectonic interpretations based on the tomographic images.

Denali Gap and the Yakutat terrane

The shallow portion of the slab within the Denali gap, which bears the over-thickened Yakutat crust, dips at a shallow angle of $\sim 30°$to $\sim$100km depth, where it steepens to $\sim 60°$(Figure 3.6b). This behavior is indicated by the WBZ (Ratchkovski et al. 2002). Beyond the northwestern edge of the subducted Yakutat region the slab dips steeply into the mantle all the way along the Denali gap. The dip increases towards the northeastern corner, where the slab is almost vertical. This is consistent with the observations of Lallemand et al. (2005), who note an increase in slab dip with edge proximity at many subduction zones. This phenomenon could be attributed to localized heating of the lithosphere near the slab edge, which facilitates bending and steepening when the slab is continuous to great depths. Edge heating may also promote a shallower basalt-eclogite transition, which would encourage steepening (e.g. Arrial et al. 2013) and may, in addition to the heating, help to explain why the northeastern edge of the slab is aseismic at 100km (Figure 3.5)

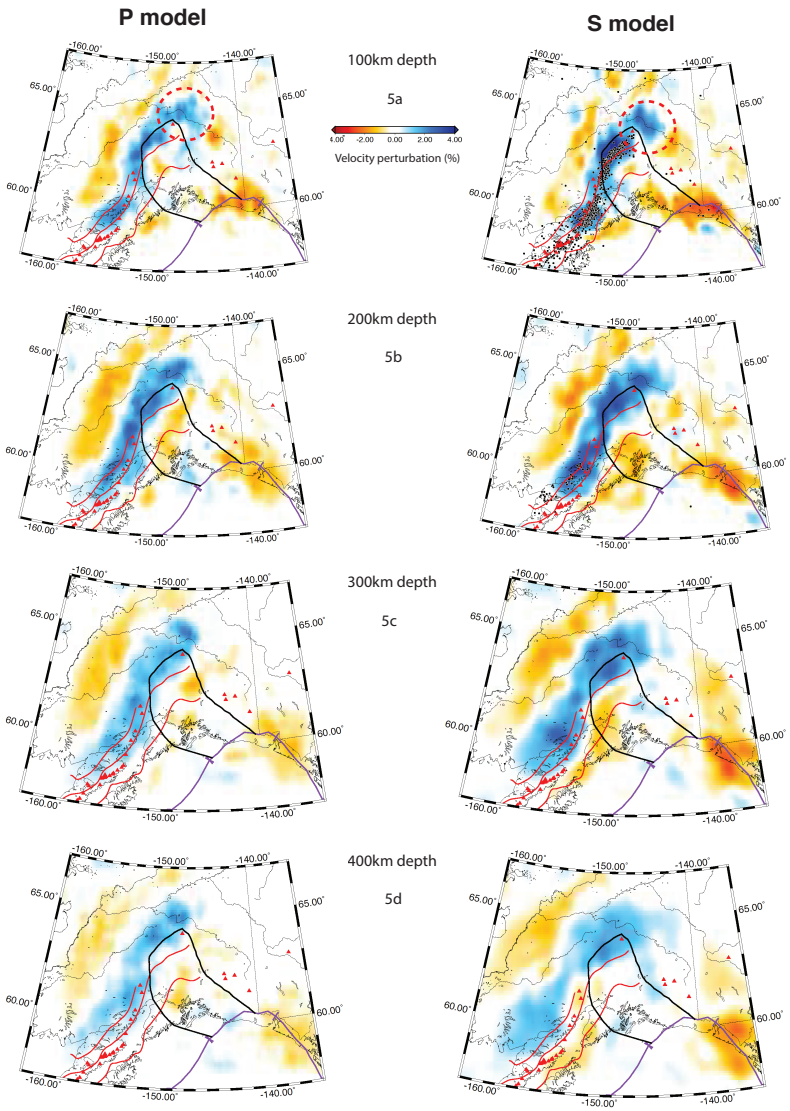

Figure 3.5: Depth slices though P and S wave tomographic models within the blue box in Figure 3.1. Blue regions indicate high velocity anomalies, which are commonly interpreted to be relatively cold, dense regions of the mantle. These images clearly show the presence of an elongate, high velocity anomaly that dips towards the northwest. This is interpreted to be the subducting Pacific-Yakutat slab. The black line indicates the subducted extent of the Yakutat terrane from Eberhart-Phillips et al. (2006). Red lines are 50km slab-depth contours from the slab 1.0 model (Hayes et al. 2012). Red triangles are Holocene volcanoes. The red circle in Figure 3.5a indicates a well-resolved high velocity anomaly that extends significantly to the northeast of the seismicity. Earthquake hypocenters from the Alaska Earthquake Information Center (AEIC) catalog of M $>$ 5.0 and within 20km the depth slice are plotted on the S model.

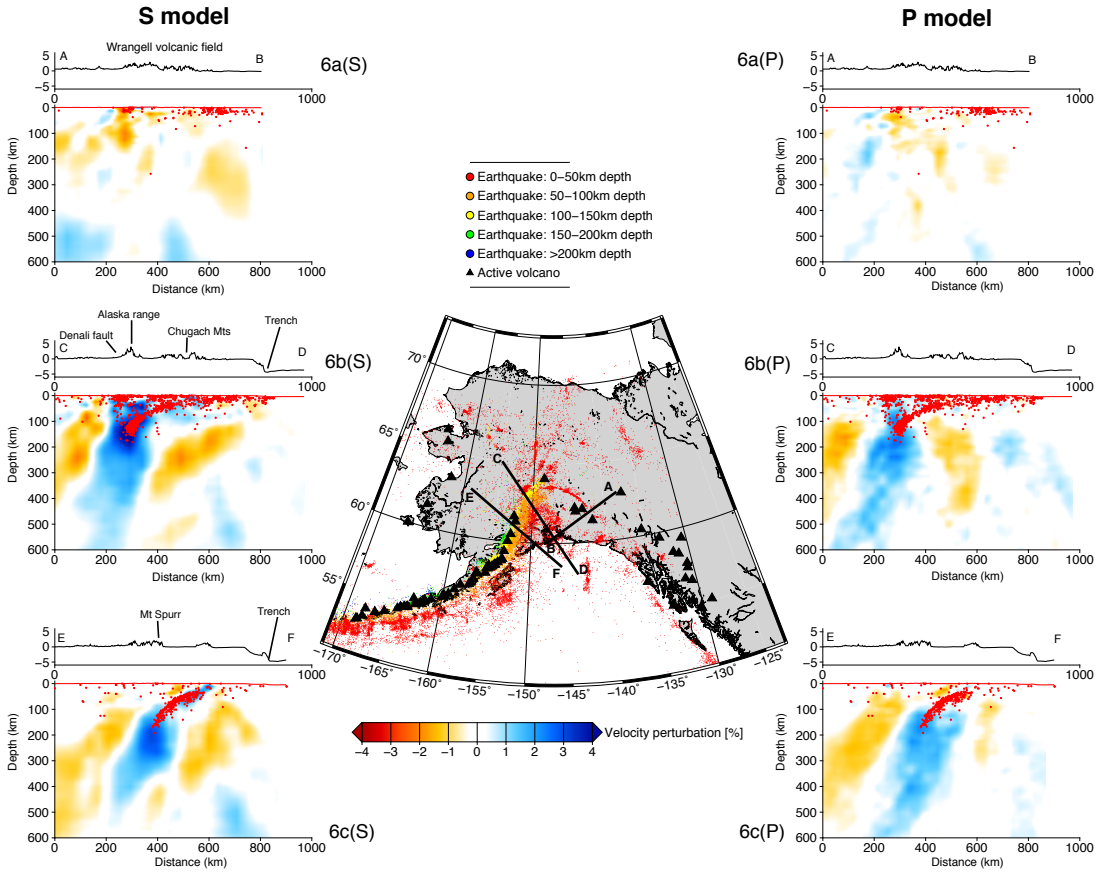

Figure 3.6: Cross-sections though the tomographic models and topographic relief in three regions of interest: A-B (3.6a), Wrangell volcanic belt; C-D (3.6b), Denali volcanic gap; E-F (3.6c), Volcanogenic region. The hypocenters of earthquakes with M $>$ 3.0 with 25km of the sections lines are shown on the cross sections. The locations of all M $>$ 3.0 seismicity in Alaska are also shown on the inset map. This earthquake information was obtained from the AEIC catalog.

If we accept that the region identified by Eberhart-Phillips et al. (2006) represents the true extent of the subducted Yakutat crust, then it follows that much of the slab material seen in our models beneath the Denali gap was subducted prior to Yakutat collision. Hence, it is Pacific lithosphere that once existed between the incoming Yakutat block and the Alaskan margin. Evidently, the Yakutat collision initiated a northwestward propagating zone of flat-slab subduction beneath the Denali gap but the flattened Yakutat portion remained connected to the older, steeper, Pacific portion. The effects of the Yakutat subduction at shallow depth may also have encouraged steepening of the deeper part of the slab, consistent with the instantaneous modeling of Jadamec et al. 2010. Time-dependent, three-dimensional modeling of the situation would be required to further test this hypothesis.

Seismic imaging studies of the Yakutat terrane suggest that it subducts to $\sim$ 150km depth beneath the Denali gap (e.g. Ferris et al. 2003; Rondenay et al. 2008). These studies also reveal that seismic activity is concentrated within the descending Yakutat crust. Our images suggest that the WBZ lies close to the uppermost surface of the subducting slab below the Denali gap and terminates abruptly at $\sim$ 150km, perhaps associated with the leading edge of the Yakutat terrane. Seismic activity is particularly intense in the 100-150km-depth range (Figure 3.6). These observations support the suggestion that these intermediate depth earthquakes are generated by dehydration reactions in the basaltic Yakutat crust, which transforms to eclogite within this depth range (Hacker et al. 2003). The presence of dehydration-related seismic activity here has important implications for the possible causes of the Denali volcanic gap: it implies that the mantle wedge is hydrated. Studies of thermal conditions (Rondenay et al. 2008) and seismic attenuation (Stachnik et al. 2004) predict that mantle wedge temperatures here should exceed the wet-solidus of peridotite, allowing melt generation in the presence of water sourced from the slab. Therefore, some feature of the Denali gap region must prevent mantle wedge melt from reaching the surface and erupting as volcanoes as it does along the Aleutian Island arc.

Rondenay et al. (2010) propose a model to explain the paucity of volcanism in the Denali Gap, whereby the advancing shallow subduction of the Yakutat terrane cools the mantle wedge system and prevents melt from accumulating in a 'pinch zone' where it can feed volcanism. Instead, the melt is proposed to accumulate in a more diffuse region at the top of the mantle wedge, simultaneously explaining a low velocity anomaly imaged there (Rondenay et al. 2008). An alternative hypothesis suggests that melt is present in the mantle wedge, but is unable to migrate to the surface due to the compressional regime that exists within the crust between the megathrust and the Denali fault system (McNamara et al. 2002). The resolution of our tomography models is insufficient to discern features of the continental crust or shallow mantle wedge, although it is intriguing that high velocity anomalies and more abundant seismic activity are observed in the mantle wedge below the Denali gap, whereas this is not the case beneath the volcanic region (Figure 3.6). This could hint at a cooler mantle wedge beneath the Denali gap, which may hinder volcanism as suggested by Eberhart-Phillips et al. (2006). However, this observation is difficult to reconcile with the

hypothesis of Rondenay et al. (2010) and additional imaging constraints from surface waves or local seismicity would be required for further investigation.

Volcanic arc

Figure 3.6 shows a cross section through the eastern end of the Aleutian-Alaskan arc, near Mt Spurr, a stratovolcano typical of this chain. Here, the WBZ lies along the uppermost surface of the descending slab, before terminating at $\sim$ 200km depth. This suggests that seismic activity here is mainly due to dehydration of the subducted oceanic crust (Hacker et al. 2003). The slab profile is very similar to that for the Denali Gap region (Figure 3.6), although the length of shallow, low-angle subduction is smaller ($<$ 200km), near-surface earthquake activity is less abundant and there are no high velocity anomalies in the mantle wedge. Volcanic activity is generally located above the 100km slab depth contour, implying the existence of a hydrated mantle wedge and migration pathways for melt to reach the surface.

Wrangell slab

We observe a continuous curtain of subducted material from the Aleutian Island arc into central Alaska, but one that terminates at $\sim$ 145°W instead of continuing below the Wrangell volcanoes (Figure 3.5). This geometry is similar to that predicted by Jadamec et al. (2010) based on numerical modeling of the mantle flow field around the slab edge and comparison with observations of seismic anisotropy (e.g. Christensen et al. 2010). The preferred model of Jadamec et al. (2010) features a 325km deep Pacific-Yakutat slab that terminates at 148°W but is connected to a much shorter Wrangell slab that extends down to 125km. The presence of this sharp slab edge is predicted to generate a toroidal flow pattern and mantle upwelling beneath the WVF, which led Jadamec et al. (2010) to suggest that volcanism here could be driven by this upwelling. Our models support this interpretation to the extent that we see no evidence for a slab beneath the Wrangell volcanoes, implying that activity there must have some other source (Figure 3.6). We also see several vertically continuous low velocity anomalies within close proximity to the WVF, which may tentatively be linked to mantle upwelling.

Finzel et al. (2011) propose a further explanation for Wrangell volcanism, which may also be consistent with our images. The northwestward younging of Wrangell volcanic belt strata and its close proximity to the eastern edge of the subducted Yakutat terrane implies some connection to the low-angle insertion of the Yakutat crust beneath North America. A combination of magmatism along extensional strike-slip faults and partial melting of the Yakutat slab edge could be invoked to explain the spatial variation in the geochemical characteristics of the Wrangells, and imply that a deep slab is not necessary to explain them (Skulski et al. 1991; Finzel et al. 2011).

3.8 Concluding remarks

We have presented P- and S-wave finite frequency tomographic models of the mantle beneath South-Central Alaska using data from new seismometer networks. Our models demonstrate for the first time the presence of a deep, continuous slab that extends from Cook Inlet into central Alaska, where it terminates abruptly. Slab dip is shallow where thick Yakutat crust is subducting, but steepens dramatically beyond its northwest boundary. Slab geometry cannot explain the Denali volcanic gap, which thus more likely owes its existence to variations in either mantle wedge characteristics, or the overriding plate (e.g. McNamara et al. 2002; Rondenay, Montési, et al. 2010). Evidence for a deep slab beneath the Wrangell volcanoes is lacking, in line with the geodynamic modelling predictions of Jadamec et al. (2012). An alternative magma source for Wrangell volcanism, such the Yakutat-edge-melting model of Finzel et al. (2011), or the slab-edge upwelling suggestion of Jadamac et al. (2010) is thus required.

A full published version of this paper can be found at https://doi.org/10.1002/2016GL070580

This chapter follows the theme of this thesis by leveraging a large, publicly available seismic dataset from a newly installed, community driven experiment in Alaska. One major component of this work that is not discussed in the text above involved the complete restructuring of a group of scripts and codes used within the UC Berkeley Seismological Laboratory for seismic tomography. The entire workflow from data acquisition to visualization of the results is now available as a software package from the group's Github page. It is fully documented and has been tested on Mac and Linux operating systems.

3.9 Chapter acknowledgments

This paper benefitted from useful discussions with R. Porritt and the comments of two anonymous reviewers. Data were sourced from the IRIS Data Management Center, which is funded through the Seismological Facilities for the Advancement of Geoscience and EarthScope (SAGE) Proposal of the National Science Foundation (NSF) under Cooperative Agreement EAR-1261681. Data from the TA network were made freely available as part of the EarthScope USArray facility, operated by IRIS and supported by the NSF under Cooperative Agreements EAR-126168. The program obpyDMT (Hosseini et al. 2017) was used to download the seismic waveforms. Figures were produced using the Generic Mapping Tools software (Wessel et al. 1998).

Chapter 4

Seismic Imaging of the Alaska Subduction Zone: Implications for Slab Geometry and Volcanism[1]

Advisor: Richard M. Allen

Coauthors: Ian Bastow, Robert Porritt & Meghan Miller

4.1 Chapter summary

Alaska has been a site of subduction and terrane accretion since the mid-Jurassic. The area features abundant seismicity, active volcanism, rapid uplift and broad intraplate deformation, all associated with subduction of the Pacific plate beneath North America. The juxtaposition of a slab edge with subducted, over-thickened crust of the Yakutat terrane beneath central Alaska is associated with many enigmatic volcanic features. The causes of the Denali Volcanic Gap, a 400km-long zone of volcanic quiescence west of the slab edge, are debated. Furthermore, the Wrangell Volcanic Field, southeast of the volcanic gap, also has an unexplained relationship with subduction. To address these issues, we present a joint ambient noise, earthquake-based surface wave and P-S receiver function tomography model of Alaska, along with a teleseismic S-wave velocity model. We compare the crust and mantle structure between the volcanic and non-volcanic regions, across the eastern edge of the slab and between models. Low crustal velocities correspond to sedimentary basins, and several terrane boundaries are marked by changes in Moho depth. The continental lithosphere directly beneath the Denali Volcanic Gap is thicker than in the adjacent volcanic region. We

[1]Published as MartinShort, R, et al. Seismic Imaging of the Alaska Subduction Zone: Implications for Slab Geometry and Volcanism. Geochemistry, Geophysics, Geosystems 19.11 (2018): 4541-4560.

suggest that shallow subduction here has cooled the mantle wedge, allowing the formation of thick lithosphere by the prevention of hot asthenosphere from reaching depths where it can interact with fluids released from the slab and promote volcanism. There is no evidence for subducted material east of the edge of the Yakutat terrane, implying that the Wrangell Volcanic Field formed directly above a slab edge.

4.2 Introduction

Alaska exhibits a broad range of tectonic processes, the study of which can be used to address broader questions surrounding subduction, arc accretion, continental crust growth and magmatism. Much of the Alaskan crust comprises rocks associated with the northern Cordilleran orogen, which represents westward growth of the North American continent by accretion of terranes to the margin of Laurentia since the Late Triassic (Plafker et al. 1994; Nelson et al. 2006). This process continues today with the convergence and partial subduction of the Yakutat terrane with the southern margin of Alaska, at the northeastern corner of the Pacific plate (e.g. Plafker et al. 1994; O'Driscoll et al. 2015; Eberhart-Phillips et al. 2006). This unique geometry chronicles a transition from subduction of the Pacific plate beneath North America in the west into right-lateral strike slip motion in the east. Furthermore, the region exhibits a myriad of interesting tectonic and geodynamic processes within a relatively small area: abundant seismicity, shallow subduction, broad intraplate deformation and uplift, mantle flow around a slab edge, unusual magmatic activity in the Wrangell Volcanic Field and a zone of volcanic quiescence known as the Denali Volcanic Gap (Plafker et al. 1994; Wang et al. 2014; Martin-Short et al. 2016; Jadamec et al. 2010; Rondenay et al. 2010; Preece et al. 2004; Eberhart-Phillips et al. 2006).

Of these, the magmatic features are perhaps the most poorly understood: the Denali Volcanic Gap (DVG) has been a region of volcanic paucity since the Miocene (Plafker et al. 1994). It extends $\sim$ 400 km NE along strike of the subducting slab, from the eastern end of Aleutian Island Arc volcanism at Mt. Spurr to the eastern terminus of the subduction zone (Figure 4.1a). It aligns with the northwestern edge of the subducted Yakutat terrane as determined by Eberhart-Phillips et al. (2006). The Yakutat terrane is a portion of buoyant, over-thickened ($>$ 20km) oceanic crust, thought to have formed as an oceanic plateau (Christeson et al. 2010). Yakutat subduction is believed to have caused shallowing of the slab beneath south-central Alaska (Plafker et al. 1994). Globally, subduction zones of over-thickened crust are known to be associated with slab-flattening and volcanic gaps (e.g. Gutscher et al. 2000).

The DVG features a well-defined Wadati-Benioff Zone (WBZ) to $\sim$ 120km depth, likely associated with seismicity generated by the expulsion of water from hydrous minerals (Rondenay et al. 2008). The subduction style beneath the DVG differs from archetypal regions of flat-slab subduction (e.g. Nankai, Peru and Chile) because its WBZ does not become horizontal (Gutscher et al. 2000; Chuang et al. 2017). Furthermore, several studies have argued that

the sub-DVG mantle wedge may feature conditions suitable for melt production, but suggest that this melt is unable to reach the surface (e.g. McNamara et al. 2002; Rondenay et al. 2010).

The Wrangell Volcanic Field (WVF) lies just east of the eastern edge of the subducted Yakutat terrane (Figure 4.1a); it is dominated by large, andesitic shield volcanoes and calc-alkaline affinity lavas that are typical of continental volcanic arcs (Richter et al. 1990). However, the WVF also features some unusual characteristics: the presence of adakitic and tholeiitic lavas at some locations (e.g. Preece et al. 2004), a northwestwards progression in activity over time (Richter et al. 1990) and limited seismic or tomographic evidence for an underlying slab (Martin-Short et al. 2016). These findings raise questions about the source of magma for the WFV and how it is connected to the history of Yakutat subduction, which is thought to be associated with the onset of volcanism here (e.g. Finzel et al. 2011).

Any explanation of the causes of volcanism in the WVF requires consideration of the eastern edge of the subducted Pacific-Yakutat plate, the location of which is also a subject of debate (e.g. Wech 2016). Although the Wadati-Benioff zone terminates abruptly at $\sim 148°$W, there are multiple lines of evidence that suggest that the slab extends further east. This includes the location of the eastern edge of the Yakutat terrane as inferred from local tomography (Eberhart-Phillips et al. 2006) and the eastern limit of slab-related high velocity anomalies seen in teleseismic surface wave (Wang et al. 2014) and teleseismic body wave (Martin-Short et al. 2016) tomography. Furthermore, Wech (2016) identified a zone of tectonic tremor extending 85 km east of the eastern edge of the Wadati-Benioff zone, suggesting the presence of an aseismically-deforming slab (Figure 4.1c). It has been suggested that the slab extends further east of the tremor zone, below the WVF, but deforms by continuous slip there (Wech 2016). This interpretation has important implications for the potential causes of volcanism here and, given the lack of seismicity, high resolution imaging of the upper mantle is required to locate the eastern edge of the subducting material.

The Alaskan subduction zone has been the subject of numerous seismic imaging studies. However, most utilize linear or small-aperture seismometer networks, whose resulting models do not fully map the geometry of the subducting material beneath Alaska. Recent deployment of the EarthScope Transportable Array (TA) offers an unprecedented opportunity to expand these models.

This study uses data from 405 broadband seismograph stations, including TA deployments up to September 2017 (Figure 4.1b). We construct an absolute S-wave velocity model using a joint inversion of Rayleigh wave phase velocity maps from ambient noise and earthquake-based surface wave tomography in combination with P-S receiver functions calculated at each station. This joint model complements an updated version of the finite frequency, earthquake-based S-wave relative-arrival-time model of Martin-Short et al. (2016), which uses data from the TA and AK networks from January 2014 to September 2017. All models

presented are isotropic. Our ambient noise workflow constructs phase velocity maps for periods of 10-35s, which are sensitive primarily to crustal velocity structure. Our earthquake-based surface wave tomography workflow generates phase velocity maps for periods 25-130 s, which are sensitive primarily to the velocity structure at lower-crustal to mid upper-mantle depths. To improve the resolution of velocity discontinuities, we use P-to-S receiver functions (Miller et al. 2018) calculated using the FuncLab software package (Eagar et al. 2012; Porritt and Miller 2018).

Numerous recent studies have used joint inversion of phase velocities from ambient noise and teleseismic surface waves in regional tomography (the central Andean plateau; Ward and Lin 2018, Madagascar; Pratt et al. 2017; the Malawi rift, Accardo et al. 2017). Receiver functions have also been incorporated into such inversions (e.g. Porritt et al. 2015). However, few studies have marshaled a combination of ambient noise, surface wave tomography, receiver functions and body wave tomography to investigate a single region as we do here.

This paper presents the most comprehensive velocity models of the Alaskan crust and mantle to date, using them to reconcile the interpretations of previous, more geographically restricted, studies of the area. Our joint imaging approach is powerful because it harnesses the complimentary strengths of each technique. However, one caveat is that it becomes difficult to accurately assess the resolution of the models because they are constructed from the inversion of multiple datasets, the uncertainties associated with which combine in a non-trivial fashion. Throughout this paper we acknowledge that confidence in our interpretation may be limited by this constraint.

Our images reveal large variations in crustal thickness across Alaska. Futhermore, they reveal significant differences between the velocity structure of the mantle wedge beneath the volcanic region and the DVG, and provide important new constraints on the eastern edge of the subducted slab.

4.3 Tectonic Setting

Alaska comprises a collection of terranes (Figure 4.1b), most of which have accreted to the western margin of North America via a combination of subduction and translation along major strike-slip faults over the past 200 Ma (Plafker et al. 1994). Throughout much of the Proterozoic, Alaska lay at a passive margin at the edge of Laurentia (Colpron et al. 2007). Continental growth began with the onset of subduction in the Devonian, which brought the Yukon Composite Terrane (YCT), whose basement material had previously rifted from the margin of Laurentia, back into contact with cratonic North America by the early Triassic. Since the Cretaceous this terrane has undergone extension and migration via right-lateral motion on the Tintina fault, which bounds it to the north (Figure 4.1d; Pavlis et al. 1993).

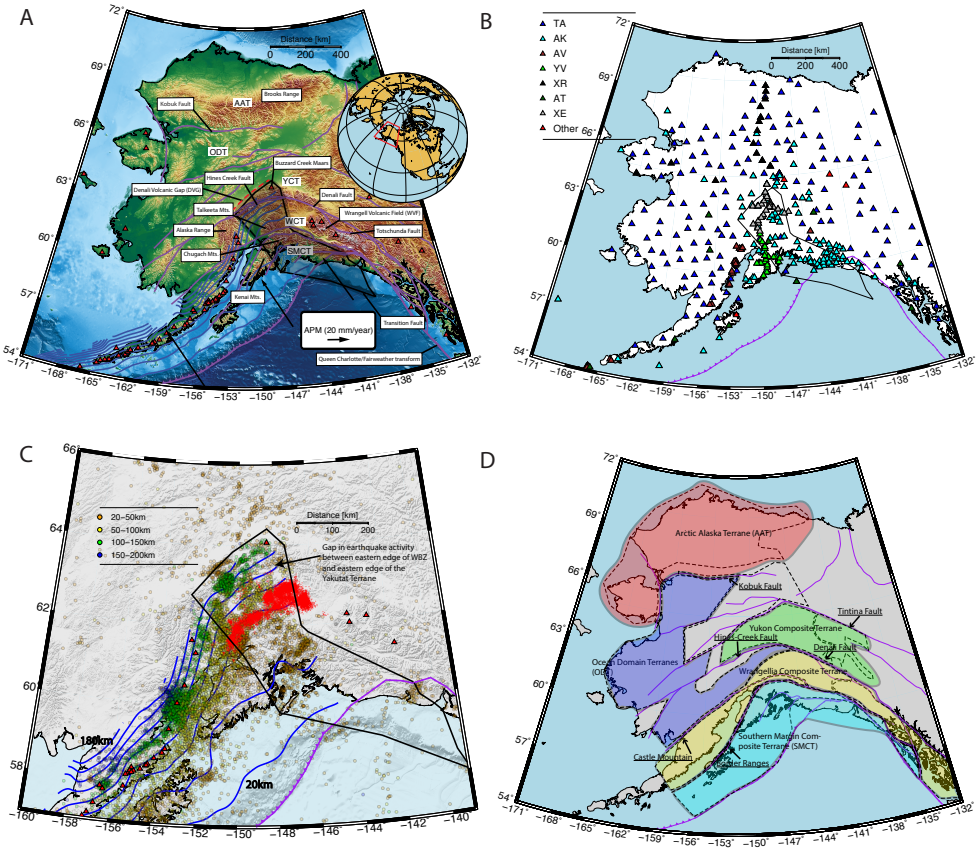

Figure 4.1: **a)** Regional tectonic setting. Purple lines: major active and inactive strike-slip faults (Colpron et al. 2007). Black line: the subducted extent of the Yakutat terrane as imaged by Eberhart-Phillips et al. (2006). SMCT = Southern Margin Composite Terrane; WCT = Wrangellia Composite Terrane; YCT = Yukon Composite Terrane; ODT = Ocean Domain Terrane; AAT = Arctic Alaska Terrane (Colpron et al. 2007). Purple lines contour the uppermost surface of the subducting slab at 20km intervals, as inferred from seismicity Hayes et al. (2012). Red triangles indicate active volcanoes. Absolute plate motion vectors were obtained from Gripp et al. (2002). **b)** The locations of the 403 broadband seismograph station locations used in this study (coverage of Alaska as of September 2017). TA = Transportable Array (167), AK = Alaska Regional Network (113), AV = Alaska Volcano Observatory (36), YV = Multidisciplinary Observation of Subduction (MOOS) (23), XR = Structure and Rotation of the Inner Core (ARCTIC) (15), AT = National Tsunami Warning System (10), XE = Broadband Experiment Across the Alaska Range (BEAAR) (31). **c)** Epicenters of all M $>$ 3 earthquakes in South Central Alaska below 20km depth, from the AEIC catalog. Red dots are tectonic tremor identified by Wech (2016). Blue lines are slab depth contours at an interval of 20km (Colpron et al. 2007). **d)** Map showing the boundaries of the composite terranes mentioned in this paper. Back dashed lines are terrane outlines from Colpron et al. (2007).

The Arctic Alaska (AAT) and Ocean Domain (ODT) terranes are located to the northwest of the YCT (Figure 4.1). The former contains continental-affinity rocks of the Alaska-Arctic microplate that collided with the northern margin of Laurentia in late Jurassic time, forming the Brooks Range (Cole et al. 1997). The latter are a complex assembly of ocean-affinity terranes accreted during the Mesozoic (Nokleberg 2000).

South of the Denali Fault, the Wrangellia Composite Terrane (WCT) comprises three major allochthonous terranes: Wrangellia, Alexander and Peninsular, which consist of various island arc assemblages, flood basalts and volcanoclastic rocks (Trop et al. 2007). By the early Cretaceaous, the WCT had accreted to the YCT via northward verging subduction. Subduction and consumption of the Kula plate, followed by subduction of the Pacific plate, then brought the Southern Margin Composite Terrane (SMCT; Figure 4.1d) into contact with North America (Colpron et al. 2007; Trop et al. 2007). This composite terrane contains mlange, scraped-off sediments and near-trench intrusive material that form an accretionary prism. The SMCT also includes the allochthonous Yakutat terrane. Thought to have been formed as an oceanic plateau off the west coast of North America $\sim$ 50 Ma, the Yakutat terrane was subsequently rafted north by dextral motion on the Queen Charlotte/Fairweather transform. It came into contact with and began subducting beneath the southern margin of Alaska as early as 35 Ma (Finzel et al. 2011; Christeson et al. 2010). Offshore seismic reflection surveys reveal that the Yakutat crust is uniform and wedge shaped, thickening from 15km to 30km in a west-east profile and overlain by $\sim$ 8km of sedimentary cover (Worthington et al. 2012). The Yakutat terrane is bounded to the south by the Transition fault (Figure 4.1a), across which there is a sharp Moho offset between $\sim$ 20Ma-old, 6km-thick Pacific crust to $\sim$ 50Ma-old, 30km-thick Yakutat crust (Christensen et al. 2010). The outline of the subducted Yakuat terrane, as inferred from the local tomography of Eberhart-Phillips et al. (2006), is highlighted in Figure 4.1.

It is generally accepted that subduction of the thick, buoyant, downgoing Yakutat crust has reduced the dip of the down-going plate, which in turn has led to rapid uplift of the Chugach and Alaska ranges, large scale crustal shortening and a cessation of magmatism in the DVG. Geological and thermochronological data suggest significant uplift in south-central Alaska began in late Eocene time and advanced northeastwards (Finzel et al. 2011). Furthermore, magmatism above the Yakutat subduction region ceased $\sim$ 32 Ma. This implies that south-central Alaska experienced steep subduction and volcanism similar to that operating in the modern Aleutian island arc before the onset of interaction with the Yakutat terrane at $\sim$ 35 Ma (Finzel et al. 2011). Additionally, there is evidence that volcanism in the WVF is connected to the history of Yakutat subduction. Geochronological evidence suggests a northwestwards progression of volcanic activity in the WFV, starting $\sim$ 26 Ma and ceasing $\sim$ 0.2 Ma (Richter et al. 1990). This led Finzel et al. (2011) to suggest that the northwestward insertion of Yakutat lithosphere beneath Alaska is responsible for WVF volcanism at the slab edge.

WVF volcanism is atypical for a subduction zone. Preece et al. (2004) identify three geochemical trends in WVF lavas that may illuminate their origins. The first is a dominant, arc-wide suite of calc-alkaline lavas derived from a mantle wedge MORB source that experienced relatively high degree partial melting due to interaction with slab-derived fluids. A second suite of calc-alkaline lavas is restricted to 'front side' volcanoes along the southeastern edge of the field. This also has a mantle wedge source, but contains adakites suggestive of slab melting (Preece et al. 2004). Thirdly, a collection of tholeiitic lavas erupted from a chain of cinder cones along the central axis of the WVF are inferred to derive from low degree partial melting of anhydrous mantle wedge material in a localized extensional setting (Preece et al. 2004). In contrast to the WVF, the geochemistry and physiography of the Aleutian arc are more typical of a subduction setting: calc-alkaline lava-erupting stratovolcanoes overlie the 100km depth contour of a well-defined, steeply dipping Wadati-Benioff zone (e.g. Plafker et al. 1994). The position of the present-day Aleutian arc was established by $\sim$ 55 Ma (Plafker et al. 1994) and, given the modern Pacific plate convergence rate of $\sim$ 50 mm/yr, several thousand kilometers of lithosphere has been subducted beneath the Aleutian arc since its formation.

4.4 Previous imaging studies

Martin-Short et al. (2016) used teleseismic P- and S-wave body wave tomography to image the Pacific-Yakutat slab beneath Alaska as a continuous feature. At $>$ 150 km depth, slab structure beneath the DVG is similar to that beneath the Aleutian Island arc. A high velocity anomaly in the mantle wedge beneath the DVG, absent beneath the Aleutian arc, is only tentatively interpreted due to poor resolution in the upper 100 km of the model. Limited resolution also hampers the ability of Martin-Short et al. (2016) to interpret shallow mantle structure beneath the Wrangell Volcanoes: despite recognizing the absence of deep subduction beneath the WVF, their model cannot preclude the presence of a flat-lying or truncated slab in the upper 100km. The surface wave tomography study of Wang et al. (2014) reaches similar conclusions: a weak high velocity anomaly underlies the WVF, but its relationship to the subducting Yakutat lithosphere is unresolved due to sparse instrument coverage northeast of the volcanoes. Additionally, Wang et al. (2014) note the presence of an aseismic portion of the slab close to its eastern edge, an observation corroborated by Martin-Short et al. (2016).

Local earthquake tomography reveals the shallow structure of the Yakutat subduction zone (Eberhart-Phillips et al. 2006). The down-going Yakutat crust is imaged as a low velocity, high Vp/Vs layer above relatively flat-lying high velocity lithosphere. This double layer structure is seen only beneath the DVG, where it extends to $\sim$ 150km depth, coincident with the termination of seismicity. The receiver function study of Ferris et al. (2003) and images from 2D multichannel inversion of scattered teleseismic body waves (Rondenay et al. 2008) confirm the presence of a low velocity zone atop the down-going Yakutat lithosphere.

This is readily interpreted as the basaltic Yakutat crust, which undergoes dehydration and transformation to eclogite, resulting in a thinning of the low velocity zone down to 150km, where it vanishes (Rondenay et al. 2008). Wadati-Benioff zone seismicity beneath the DVG follows a single plane, confined to the low velocity Yakutat crust. In contrast, intermediate depth seismicity within the downgoing Pacific slab to the west exhibits a thicker Wadati-Benioff zone with two planes of seismicity (Cole et al. 1997). This observation has been interpreted as differences in the hydration state of the Yakutat crust beneath the DVG and the Pacific crust beneath the volcanic arc, which may be an important step towards explaining the link between Yakutat subduction and volcanic quiescence (Chuang et al. 2017).

Stachnik et al. (2004) produce a 2D model of the seismic attenuation structure beneath the DVG, which exhibits three distinctive regions. First, a low attenuation zone in the nose of the mantle wedge trenchward of the Denali fault, is interpreted as cool, serpentinized material, isolated from mantle wedge convection. Second, a higher attenuation zone in the uppermost layer of the subducting lithosphere directly below the mantle wedge nose, is interpreted as fluids escaping the Yakutat crust. Finally, a high attenuation zone in the mantle wedge northwest of the Denali fault is interpreted as hot, convecting mantle material. However, the maximum attenuation values in this region are roughly half those of the central Andes and northern Japan subduction zones, suggesting a wedge that is 100-150°C cooler than 'normal' (Stachnik et al. 2004). This observation has been suggested as an explanation for the DVG and is consistent with the high velocity anomaly in the DVG mantle wedge imaged by Martin-Short et al. (2016). Eberhart-Phillips et al. (2006) also see a high velocity anomaly here, but interpret it as a residual slab segment from partial subduction of the WCT beneath the YCT. Such a feature could inhibit the passage of fluids and magma towards the surface, but its continuity beneath the DVG is poorly constrained.

Other studies assert that melt is present within the DVG mantle wedge, but cannot reach the surface: local tomography-derived Poisson's ratios are similarly high beneath the DVG and arc volcanoes to the west (McNamara et al. 2002), suggesting suitable melting conditions in the DVG wedge, but with melt migration arrested by increased compression in the overlying crust as a result of Yakutat collision (McNamara et al. 2002). Rondenay et al. (2010) propose a model in which shallowing of the slab dip due to Yakutat subduction has cooled the DVG mantle wedge and prevented the accumulation of melt produced in a 'pinch zone' from which it can erupt. This explains the presence of a flat-lying low velocity zone at 60km depth in the images of Rondenay et al. (2008), interpreted as pooling melt beneath the LAB. Rondenay et al. (2010) support their interpretation via geodynamic modeling of the evolution of the mantle wedge temperate field in the case of steady-state subduction and slab advance. Given an approximation to the shallow slab geometry beneath the DVG and in the presence of temperature-dependent viscosity, slab advance acts to cool the mantle wedge and limits the focused accumulation of melt, extinguishing volcanism (Rondenay et al. 2010); slab advance associated with Yakutat subduction has thus led to a cessation of

DVG volcanics.

A similar argument pertains to the eastern edge of the subducted slab beneath South-Central Alaska. Geodynamic modeling of mantle flow and comparison to constraints from seismic anisotropy supports the existence of deep subduction west of $\sim 148°$E, but only a short (reaching < 115 km depth) slab beneath the WVF (Jadamec et al. 2010). Whether the edge of the subducted Yakutat terrane corresponds to the slab edge, or non-Yakutat lithosphere exists further to the east or beneath the WVF is unclear, with important implications for potential magma sources here.

However, the Wadati-Benioff zone terminates west of the edge of the tomographically imaged Yakutat terrane (Eberhart-Phillips et al. 2006, Wang et al. 2014; Martin-Short et al. 2016) and the extent of the slab as inferred by tectonic tremor (Wech 2016). Indeed, a transition in tremor frequency from low in the west to high in the east led Wech (2016) to assert that deformation continues by continuous aseismic slip further east, connecting the seismic Pacific-Yakutat slab to an aseismic Wrangell slab. The causes of intermediate depth seismicity, or lack thereof (e.g., in Cascadia) are debated, but are thought to be related to the structure and hydration state of the down-going plate (e.g. Hacker et al. 2003). The presence of a slab edge and close proximity of hot asthenospheric material may influence the transition from seismic to aseismic deformation here, but the geometry of this boundary must be mapped to address such issues.

The receiver function studies of O'Driscoll et al. (2015) and Bauer et al. (2014) have attempted to constrain the subduction geometry beneath Alaska by imaging velocity discontinuity structures. The S-P receiver function model of O'Driscoll et al. (2015) does not resolve moderate-to-steeply dipping structures, but reveals a flat Yakutat LAB at $\sim$ 100km depth beneath south-central Alaska and hints at the existence of a shallow slab beneath the WVF. The plane wave migration technique employed by Bauer et al. (2014) imaged dipping features and Yakutat crust $\sim$ 80km below the WVF; the extent of the slab north of the volcanoes was unconstrained however.

Ward (2015) used ambient noise tomography to study south-central Alaska. At short periods (8-12 s), low phase velocities are associated with thick sedimentary basins such as the Cook Inlet, Kodiak Shelf and Tanana basins (Figure 4.5a). An elongate region of low phase velocities underlies the WVF at intermediate periods (14-25 s). The shape of this region mirrors that of a relatively low Bouguer gravity anomaly, implying compositional heterogeneity between the WVF and the surrounding crust (Ward, 2015). At 20-25 s period, across the Denali fault, low velocities beneath the Wrangellia Composite Terrane in the south contrast with higher velocities in the north, beneath the Yukon Composite Terrane. This is interpreted as a change in crustal thickness between the terranes. A Moho offset of $\sim$ 10km near the Denali Fault has been reported by receiver function studies (e.g. Veenstra et al. 2006; Brennan et al. 2011; Miller et al. 2018) and local tomography (Allam et al. 2017),

which demonstrates the offset occurs across the Hines Creek fault in central Alaska and the Totschunda Fault to the east. The crust thickens again further north beneath the Brooks Range (Fuis et al. 2008).

4.5 Datasets and methodology

Rayleigh wave phase velocity maps are produced using independent workflows for the ambient noise and earthquake surface wave datasets. Receiver functions were then generated for all stations Miller et al. (2018), before being inverted jointly with the phase velocity data for absolute shear wavespeed below each station. Finally, a 3D S-velocity map is generated by interpolation between station locations.

Ambient noise tomography

Continuous, day-long, long-period, vertical component seismograms from broadband stations in the region 52-73°N, 171-123°W were analyzed for the period January 2014 to September 2017 (Figure 4.1a). Following Bensen et al. (2008) and Ward (2015), time domain normalization with an absolute mean method and a 128s window was applied to these data after filtering in a 5-150 s passband. Spectral whitening was then applied to reduce spectral imbalance and the real and imaginary components of each day-long time-series were output. Station spectra were grouped into month-long segments and cross-correlograms determined for each station-station pair. These were subsequently stacked over the maximum available timeframe. The resulting two-sided, stacked cross-correlograms are dominated by Rayleigh wave energy travelling between the stations in two directions. They can then be averaged to create a symmetric signal, which is an estimation of the Empirical Green's Function (EGF) of the station-station path (Bensen et al. 2007). The dispersion characteristics of EGFs were determined using the FTAN method with a phase-matched filter Levshin et al. (1992), yielding group and phase velocity dispersion curves for each station-station path at periods of 8-40s. Dispersion curves corresponding to station pairs where one station is far outside the region of interest (Figure 4.2) were removed, as were dispersion measurements with a signal-to-noise ratio < 15 and an interstation distance < 3 wavelengths. These criteria follow Ward (2015), but we found that varying them had little impact on the final model. The remaining dispersion measurements were then inverted for 2D maps of phase velocity for periods of 10-35s using the ray theoretical surface wave inversion method of Barmin et al. (2001). Resolution testing indicates that our ray coverage yields phase velocity maps able to resolve features of lengthscale $\sim$ 100km.

Our inversions are regularized via three user-defined parameters: The damping (α), the smoothing in regions of poor path coverage (β), and the Gaussian smoothing width (σ). Systematic variation of these parameters and inversion on a 0.1°x0.1°grid reveals that their values do not significantly affect the results within the region of interest. Thus we follow

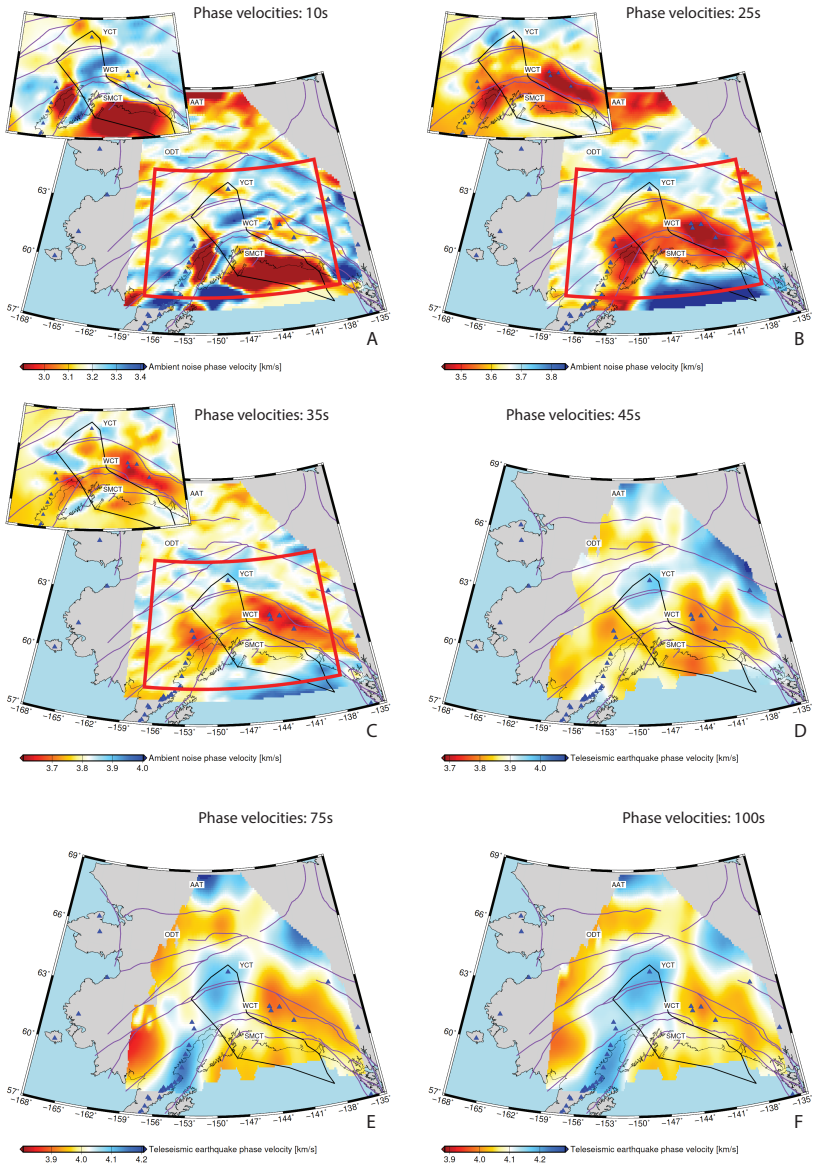

Figure 4.2: Rayleigh wave phase velocity maps for periods of 10s (a), 25s (b), 35s (c), 45s (d), 75s (e) and 100s (f). Maps (a) to (c) were constructed using the ambient noise tomography workflow and corroborate the results of Ward (2015) (inset maps). Maps (d) to (f) are constructed using the earthquake-based surface wave tomography workflow. Purple lines are major faults; the black line indicates the extent of the Yakutat Terrane. Blue triangles are active volcanoes. Short periods reveal variation in crustal structure, while the high-velocity subducting slab becomes increasingly apparent at longer periods. Panels a) to c) show the same geographic region as selected for the final velocity model, while panels d) to f) color only grid cells whose phase velocities are constrained by more than 10 station-event pairs.

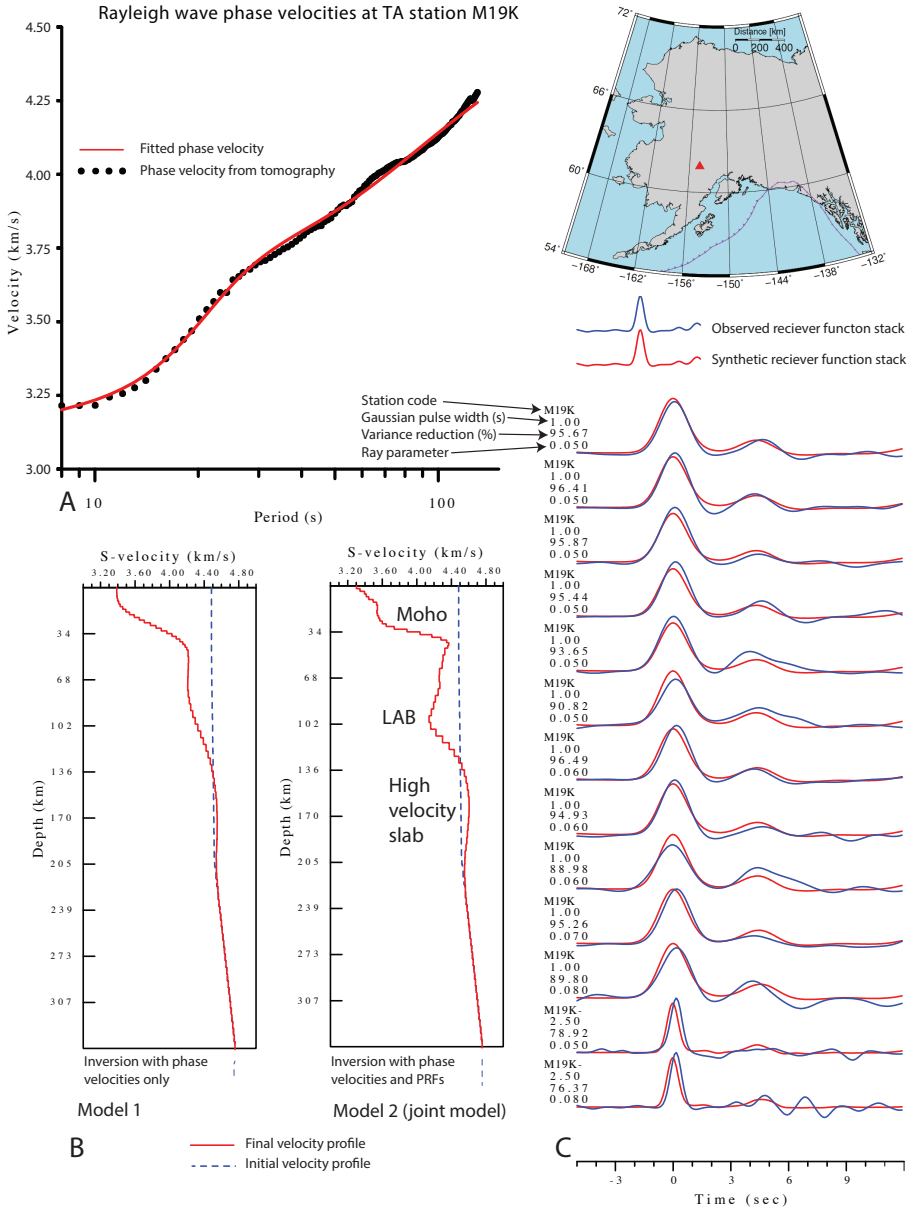

Figure 4.3: Example of the joint inversion workflow for station M19K, which lies above the subducting Pacific plate. (a) the fit to the phase velocity data. (b) final velocity models constructed using just the phase velocity data (model 1) and with the addition of the receiver functions (models 2 and 3). The joint model is the preferred model because it reveals a clearer discontinuity structure. (c) shows fits to the observed receiver function stacks.

Ward (2015) and use $\alpha = 600$ and $\beta = 100$; σ is roughly equal to one wavelength of the inversion period. Our results are similar to those of Ward (2015) where they overlap spatially, but span a larger area due to our expanded station coverage (Figure 4.3).

Earthquake-based surface wave tomography

To investigate deeper velocity structure, we follow Jin et al. (2015) and use the Automated Surface Wave Measuring System (ASWMS) software package to produce 25-130 s period fundamental mode Rayleigh wave phase velocity maps from the seismograms of teleseismic earthquakes. We analyze waveforms recorded at all stations for earthquakes of mb > 6 from January 2014 to September 2017 within a distance range of 20-160°. For each station-event pair, the Rayleigh wave and most of its coda are windowed and a cross correlation between this packet and waveforms recorded for the same earthquake at all stations within 500km is performed. The peak of each cross-correlogram is further windowed and the periods of interest are isolated by application of narrow bandpass filters. Each filtered cross-correlogram can be represented by a 5-parameter wavelet, two of whose parameters are the time-dependent group and phase delays between the two stations whose waveforms were cross-correlated. For each frequency the results are inverted for the phase traveltime gradient, which is then used by the Eikonal and Helmholtz equations to produce phase velocity maps (Jin et al. 2015). Smoothing and quality control parameters in the ASWMS workflow are chosen to minimize the difference in appearance between phase velocity maps in the 25-35 s period range and those produced for the same period range by the ambient noise tomography workflow. Phase velocity maps produced by the ASWMS workflow are sensitive to the lower crust and upper mantle at short periods; longer periods image the subducting Pacific-Yakutat plate.

Receiver functions

Receiver functions are estimations of the Earth response function beneath a seismometer (e.g. Langston 1979). We utilize a large database of P-S receiver functions determined at 468 stations in Alaska and the Yukon by Miller et al. (2018). An upgraded version of the Funclab software package (Eagar et al. 2012; Porritt and Miller 2018) is used to calculate and trace-edit the receiver functions. The first step involves time-domain iterative deconvolution to estimate the radial Earth response, which is then multiplied by the transform of a 2.5s-wide Gaussian pulse in the frequency domain to limit the inclusion of high frequency signals not warranted by the observations Langston (1979). We supplement this dataset with receiver functions for TA and AK network stations, calculated from waveforms recorded between January 2014 and September 2017. A Gaussian pulse of 1 s width damps high frequency signals in the receiver functions, leaving them with only the direct arrival and signals from the most significant discontinuities.

In preparation for the joint inversion workflow, we follow Porritt et al. (2015) by binning the receiver functions at each station in ray parameter increments of 0.01 and backazimuth

increments of 45°and stack the results in each bin.

Joint inversion

We use the *Joint96* program from the Computer Programs in Seismology (CPS) software suite (Herrmann 2013) to jointly invert the stacked P-S receiver functions and phase velocities from the ambient noise and earthquake-based surface wave processing workflows (Julia et al. 2000). These datasets are theoretically sensitive to the density, P and S-velocity structure of the subsurface, but in practice the S-velocity structure has the dominant influence and is hence inverted for here (e.g. Julia et al. 2000).

In the period range 25-35 s, we have phase velocities from both the ambient noise and event-based tomography. These are combined using a simple linear weighting scheme that places 100% weight on the ambient noise tomography at 25 s and 0% at 35 s. Overlap between the ambient noise and event-based phase velocity maps is imperfect (Figure 4.2). At the model edges some stations lack sufficient event-based phase measurements to construct a full 1D profile; mean velocities corresponding to that period are used instead.

Given an 82-layer initial S-velocity model (the 1D starting velocity model of Eberhart-Phillips et al. (2006) with a constant velocity of 4.48 km/s from the surface to 60 km depth), *Joint96* conducts a series of forward calculations and linearized inversions to iterate towards a final model. In our simple starting model, the uppermost 50km is constrained by layers of 2km thickness, while the structure from 50 to 335km depth is constrained by layers of 5km thickness. Furthermore, the starting model contains no a-priori assumptions about crustal thickness, meaning the final result is entirely data-driven.

Joint96 calculates Rayleigh wave depth sensitivity kernels for each of the periods represented in the phase velocity data set. At each step, these are used to forward calculate dispersion curves following Rodi et al. (1975). Synthetic receiver functions are determined using the method of Randall (1989). Residuals are determined between the synthetic calculations and the observed data; linearized inversion is used to adjust the velocity model (Julia et al. 2000). Thirty such iterations are run, and at each step variance reduction is reported as a measure of fit between the synthetics and observations for both individual receiver functions and the dataset as a whole. The result is a profile of shear velocity as a function of depth (Figure 4.3). We permit large departures from the initial model ($>$ 1km/s) in the upper 100km, where our data provide good constraints, but decrease model variance to zero at 230km depth. We weight our phase velocity and receiver function datasets at a ratio 25:75 during the inversion, thus placing more weight on the receiver functions (Julia et al. 2000). Variation of this parameter does not significantly affect the final velocity model.

After initial calculation of the 1D velocity profiles, receiver functions whose reported variance reduction is $<$ 70% are discarded. If the variance reduction of the dispersion curve at

a station is < 70%, that station is discarded, and the *Joint96* inversion is re-run. This removes the effects of noisy receiver functions, and locations where the receiver function and phase velocity datasets cannot be satisfied by a single velocity profile.

In some locations (e.g. offshore) receiver function data are unavailable, but velocity structure can still be constrained by the phase velocity datasets. In offshore regions, we construct a 1°x1°grid of 'ghost stations' at which the phase velocity dataset alone is used to construct 1D velocity profiles. The same is true for a small number of onshore station locations where all the of the receiver function data is removed by the QC workflow.

The surface waves most sensitive to velocity structure > 100km depth have long periods (> 100s) and thus long wavelengths (> 300 km). This causes a reduction in the lateral resolution of our joint model with depth. Consequently, we truncate our profiles at 200km and use a relative S velocity model derived from finite-frequency, relative arrival-time body wave tomography to investigate the mantle below.

A three-dimensional (3D) model of shear velocity to 200km depth is constructed by linear interpolation between the 1D profiles determined at the station locations (hereafter known as the joint model). We also construct a 3D model using constraints from the phase velocities alone using the same station locations as in the joint inversion (hereafter known as model 2) and by linear interpolation between profiles determined on a regular grid with a spacing of 0.5°(hereafter known as model 3). There is little difference between models generated by the two interpolation strategies. However, at shallow depths, the grid-interpolation models contain more structure. Comparison of the joint model with the phase velocity-only model reveals that addition of receiver functions greatly improves our ability to identify the Moho and LAB (Figure 4.4).

Teleseismic body wave tomography

We extend the finite frequency, relative arrival-time S-wave velocity model of Martin-Short et al. (2016) by incorporating travel-time picks for mb > 6.0 earthquakes recorded on AK and TA instruments between June 2016 and September 2017, at epicentral distances of 30-120°. Caution should be exercised when comparing the relative and absolute velocities (Bastow 2012). However, the locations of these anomalies can be used to inform and support interpretations of the joint model above 200 km depth and extend our knowledge of the mantle structure below.

4.6 Results

We present a series of depth slices and cross sections through the joint model and teleseismic body wave models (Figures 4.5, 4.7 & 4.9). We color the depth slices by absolute velocity,

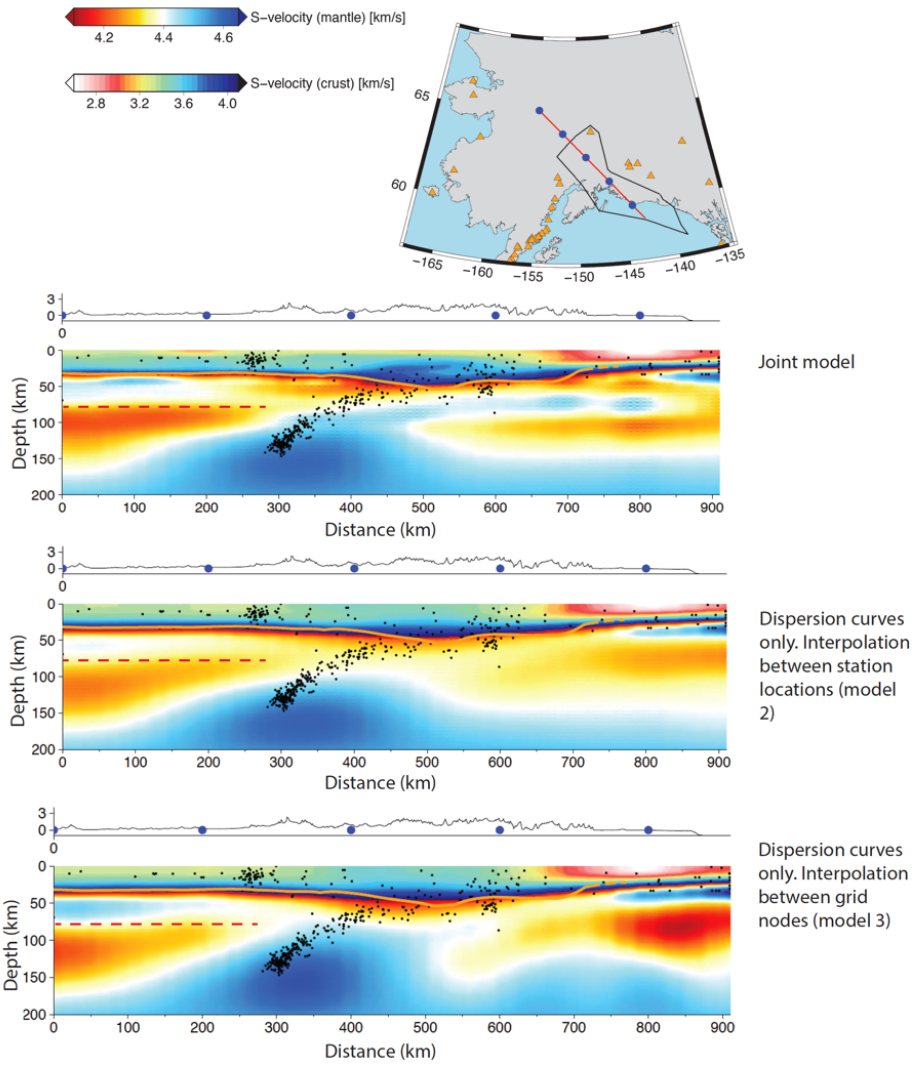

Figure 4.4: Cross-sections though the three models, showing the velocity structure of the Denali Volcanic gap (section A-B in Fig 4.7). Section A shows the joint model, section B model 2 and section C model 3. Large features such as the subducting slab, continental lithosphere and low velocity mantle wedge are consistent across the sections. However, section A clearly images the flat-lying Yakutat LAB, thus providing better constraints on the thickness and extent of the subducted Yakutat terrane than models constructed without the aid of the receiver function dataset. The flat-lying North American LAB is drawn on all three sections at the depth at which it is imaged by the joint model. It is consistently seen in all three models.

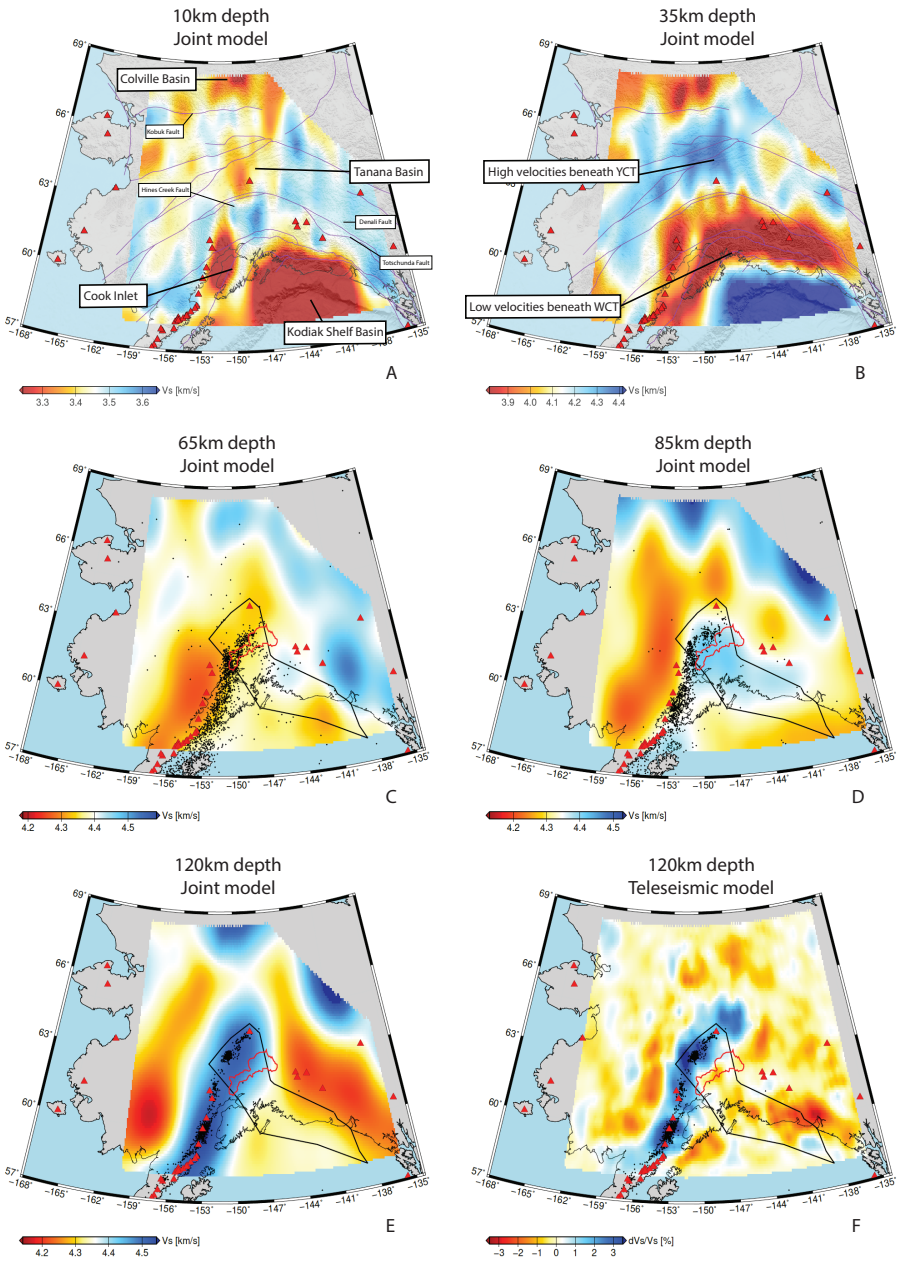

Figure 4.5: Slices though the joint model at depths of 10km (a), 35km (b), 65km (c), 85km (d) and 120km (e), which reveal large-scale variations in the crust and uppermost mantle beneath Alaska. Black dots are M $>$ 3.0 earthquake hypocenters within 5km of the depth slices. Topography contours are displayed in (a) and (b) to illustrate the connection between tomography and crustal velocity structure. Faults (purple lines) in (b) indicate differences in velocity across major terrane boundaries. The red outline in panels (c) to (f) indicates the zone of tectonic tremor identified by Wech (2016), whose eastern boundary aligns with the edge of the high velocity slab. The black line delineates the subducted Yakutat terrane. Red triangles are active volcanoes. (f) 120km depth slice though the teleseismic finite frequency S body wave, which a shows a broadly similar structure to map (e).

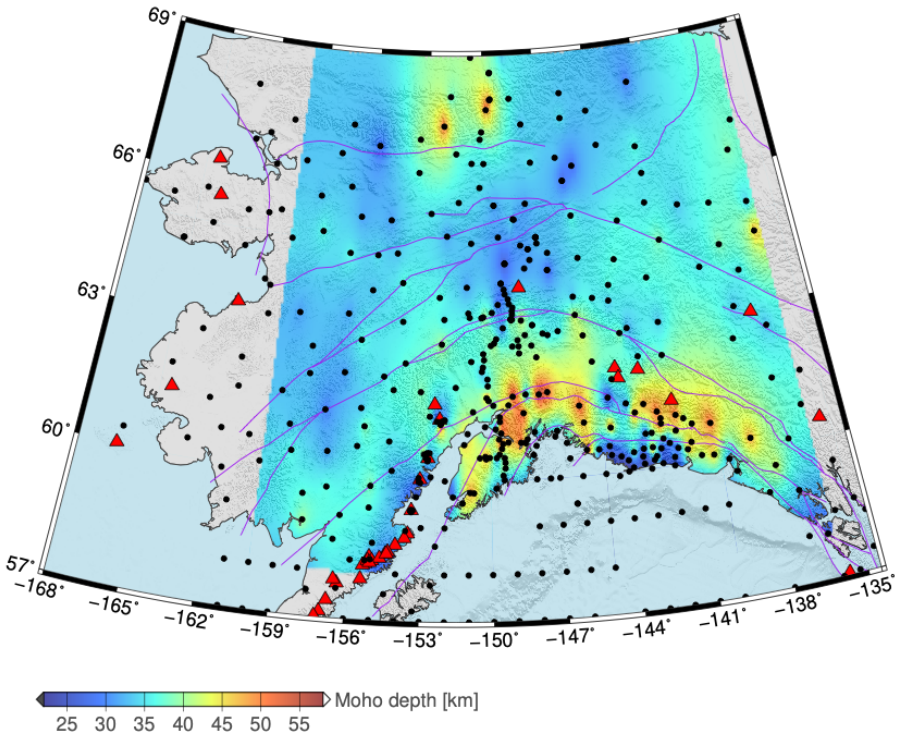

Figure 4.6: Map of depth to the Mohorovičić discontinuity beneath Alaska. This was generated via picking of the location of maximum velocity gradient between depths of 20 and 60km on each of the 1D velocity profiles produced by the joint inversion methodology. A two-dimensional (2D) spline was then fit to the depth values. The map is necessarily smooth because of the large inter-station distances, but reveals large-scale variation in crustal thickness. Shading on the map indicates topography and black dots indicate station locations at which Moho measurements were obtained.

with the color scale centered on the mean velocity at each depth. Absolute velocities in the crust and mantle are colored separately in cross sections though the joint model (Figures 4.4 4.7 & 4.9).

We identify four core observations: The pattern of velocity anomalies in the crust, variations in Moho depth across Alaska, differences in mantle wedge anomalies between the DVG and Aleutian arc, and the geometry of the subducting slab, which is inferred from the extent of a prominent high velocity feature (Figure 4.5).

At shallow depths (10-20 km) we observe several regions of very low S-wave velocity (< 3.1 km/s at 10 km), which roughly correspond to the locations of the deep Cook Inlet, Kodiak Shelf and Colville sedimentary basins (Figure 4.5). Relatively high velocities are seen beneath regions of high topography, including the Alaska and Chugach ranges, the mountains of the Aleutian Arc and the eastern YCT. The central YCT contains the lowland Tanana valley region, where relatively low velocities are likely associated with the Nenana and Yukon Flats basins (Figure 4.5). Model 3, which comprises profiles interpolated over short distances on a regular grid, yields the most detailed images of structure at these shallow depths. In the case of model 2 and the joint model, interpolation between velocity profiles determined at station locations tends to smooth short wavelength structure that is present in the ambient noise dataset and resolvable on the 0.5°grid.

At lower-crustal depths (30-45km) we see several long wavelength anomalies (Figure 4.5). There is a dramatic contrast between low velocities south of the central part of the Denali fault and high velocities to the north. Onshore velocities are highest below the lowlands of the Tanana basin and decrease again below the high topography of the Brooks Range. The lowest velocities are seen beneath the Aleutian Island arc, Chugach Mountains and WVF, corroborating phase velocity maps at intermediate periods (14-25 s) constrained by Ward (2015). The highest velocities are found offshore, beneath the Pacific plate.

A low-resolution map of continental Moho depth can be generated from the joint model by identifying the depth of maximum velocity gradient at each station location where receiver functions are available and then fitting these values with a continuous surface (Figure 4.6). We force this method to pick a Moho between 20 and 60km depth, thereby avoiding picking of the oceanic Moho in regions where oceanic crust is directly overlain by continental crust, as is the case throughout the SMCT. The map is necessarily smooth due to the station spacing, but reveals the presence of an arc of thick crust (> 50km) beneath the Chugach mountains, a transition between relatively thick (> 35km) to thin (~ 25km) crust across the central Denali fault and a return to thick crust (> 40km) below the Brooks Range. Moho picks from the joint velocity model are in good agreement with those determined directly from the P-S receiver functions by Miller et al. (2018). Furthermore, the differences in Moho depth between receiver function only and joint receiver function-surface wave inversion methodologies can often be on the order of those observed here (e.g., in Cameroon: Gallacher

et al. 2012).

In the uppermost mantle we observe several notable features. A low velocity anomaly in the mantle wedge west of the Aleutian arc at $\sim$ 60km depth persists to $>$ 100km (Figures 4.5c and 4.5d). This feature is also present, but less pronounced, in the mantle wedge beyond the northwestern edge of the subducted Yakutat terrane. A low velocity anomaly at 60 km depth beneath the northeastern edge of the WVF becomes broader and more pronounced with depth, where it connects with the low velocities in the mantle wedge north of the subduction zone. This creates a channel of low velocity material that separates high velocity features in the far north and east of the model region from those in south-central Alaska.

A broad high velocity feature is seen within the boundaries of the subducted Yakutat terrane (Figure 4.5d). It appears at $\sim$ 70 km depth in the southeast and, with increasing depth, spreads north and west to become an elongate high velocity feature that extends along the Aleutian arc and broadens beneath south-central Alaska. The western edge of this feature parallels the Wadati-Benioff zone; its east-facing edge is aligned with the tectonic tremor zone identified by Wech (2016). Furthermore, the WVF is orientated along the northeast-facing edge of this zone (Figure 4.5).

We interpret this high velocity anomaly as the subducting Pacific-Yakutat lithosphere (Figure 4.5). Below $\sim$ 100 km depth, the slab anomaly within the joint model is subject to significant lateral smearing but its geometry is consistent with that of the slab as inferred from the teleseismic body wave model (Figure 4.5f). This consistency is especially clear in cross section (e.g. Figure 4.7).

4.7 Discussion

The large spatial extent of our velocity model and its use of complementary imaging techniques allow us to provide a interpretation of the tectonic structure beneath central Alaska throughout the crust and upper mantle.

Crustal structure and Moho depth variation

At shallow depths, the lowest velocities are located within the $>$ 8 km-deep Cook Inlet and Kodiak shelf sedimentary basins (Shellenbaum et al. 2010; Christeson et al. 2010). Moderately low velocities characterize other major Cenozoic sedimentary basins (Figure 4.5a). The highest velocities are seen beneath the Chugach, Kenai and Talkeetna Mountains, which comprise layers of intermediate to ultramafic material, thought to be accreted slivers of oceanic crust Ferris et al. (2003). High velocities also characterize the Aleutian arc and western Yukon-Tanana uplands, where they likely indicate the high-grade metamorphic or igneous cores of these elevated regions.

In most locations, our model lacks the necessary resolution to map potentially-abrupt steps in crustal thickness across terrane boundaries (e.g. Allam et al. 2017; Miller et al. 2018). However, our maps, cross sections and Moho depth calculations confirm that significant crustal thickness variations exist from terrane to terrane (Figure 4.3). Despite not being constrained by receiver functions, the Pacific-Yakutat crust offshore is observed to be relatively thin compared to that of North America, hence explaining the presence of mantle velocities offshore in the 35km depth slice (Figure 4.5b). The continental crust beneath the WCT and SMCT is relatively thick, especially beneath the Chugach Mountains and south of the WVF, where it exceeds 50km. This is consistent with previous observations of Moho depth in this region (Eberhart-Phillips et al. 2006; Christeson et al. 2010; Miller et al. 2018) and is probably the result of Yakutat underplating of the WCT (Christeson et al. 2010).

The sharp velocity contrast between the WCT and YCT across the Denali Fault in central and eastern Alaska at 35km depth (Figure 4.5b) is interpreted as a Moho step. This is consistent with previous studies, which consistently report that crust below the Tanana Basin is some of the thinnest in Alaska (e.g. Veenstra et al. 2006; Miller et al. 2018) and is offset from the thick crust to the south along the Hines Creek Fault (Allam et al. 2017). This offset is most dramatic close to where the BEAAR array crosses the terrane boundary, but continues west along the Hines Creek fault and then south on the landward side of the Aleutian arc (Figure 4.5). There is no abrupt change in velocity between the YCT and ODT, but the sharp decrease in velocity seen across the Kobuk fault zone (Figure 4.5), which bounds the AAT and ODT, indicates crustal thickening beneath the Brooks Range, consistent with the findings of Miller et al. (2018).

Mantle wedge and Denali volcanic gap

Figure 4.7 shows cross sections through the velocity structure of the DVG (Figure 4.7a) and the Aleutian island arc near Mt. Spurr (Figure 4.7b). These indicate the slab and continental LAB locations, which are inferred from velocity discontinuities and agree with LAB picks from O'Driscoll et al. (2015) where the models overlap.

The slab is imaged as a dipping, high velocity (4.4-4.6 km/s) structure whose uppermost surface is delineated by a Wadati-Benioff zone. The slab geometry and velocity values are consistent with the models of Wang et al. (2014) and Eberhart-Phillips et al. (2006). The latter study has higher resolution but is more restricted spatially. Velocities in the mantle wedge are relatively low (4.2-4.3 km/s) and overlain by a zone of higher velocities (4.3-4.5 km/s), interpreted as continental lithosphere. In both cases there is a region of very low velocities (4.1-4.2 km/s) at the nose of the mantle wedge at depths of 40-60km (corresponding to $\sim$ 1.2-1.8GPa), directly above a high seismicity zone that likely marks the onset of eclogitization (Rondenay et al. 2010; Chuang et al. 2017). The large volume change that accompanies eclogitization of the down-going oceanic crust is thought to promote fluid release into the mantle wedge (Audet et al. 2009). At the cool ($< 600^{\circ}$C) mantle wedge

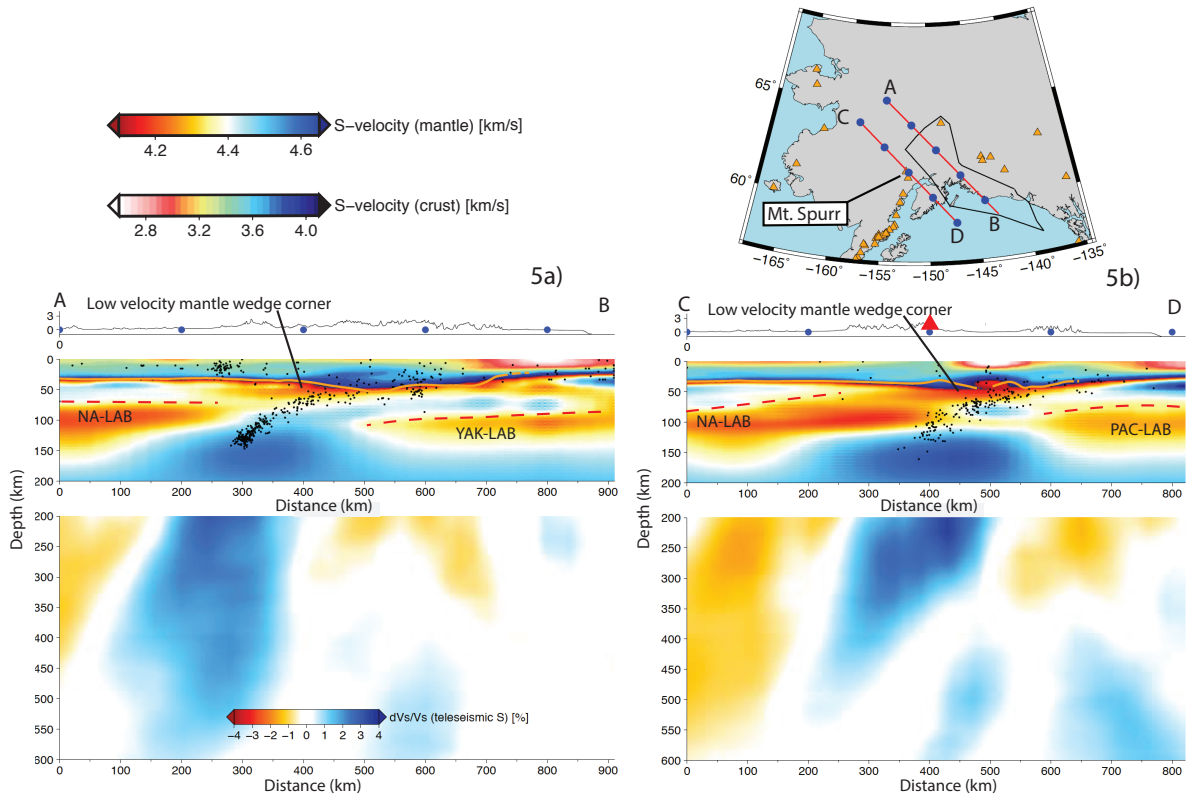

Figure 4.7: Cross-sections from the joint model (0-200km depth) and teleseismic S model (200-600km depth) though the Denali Volcanic Gap (DVG) (a) and Aleutian Arc (b). The absolute velocity structure of the crust and mantle is mapped with two different color schemes, spanning 2.65-4.10 km/s and 4.10-4.65 km/s respectively. The orange line is the continental Moho as inferred from the joint model. Black dots are earthquake hypocenters within 20km of the slices. Annotations on the joint model slice are our tectonic interpretations.

nose, hydration of peridotite leads to the formation of the serpentine mineral antigorite, the presence of which can depress seismic velocities (e.g. Christeson et al. 2010). We interpret the low velocity mantle forearc in Figures 4.7a and 4.7b to indicate the presence of fluids and the formation of antigorite. Evidently the degree of serpentinization is low in comparison to Cascadia, because the receiver functions do not indicate an inverted Moho as is there (Bostock et al. 2002). These findings support the interpretation of Stachnik et al. (2004), who attribute a high-Q region in the DVG mantle forearc to serpentinization. The Vp/Vs model of Rossi et al. (2006) also indicates $>$ 30% serpetinization within the nose of the DVG mantle wedge. Our models indicate that this serpentinized nose is present in both the volcanic and non-volcanic zones.

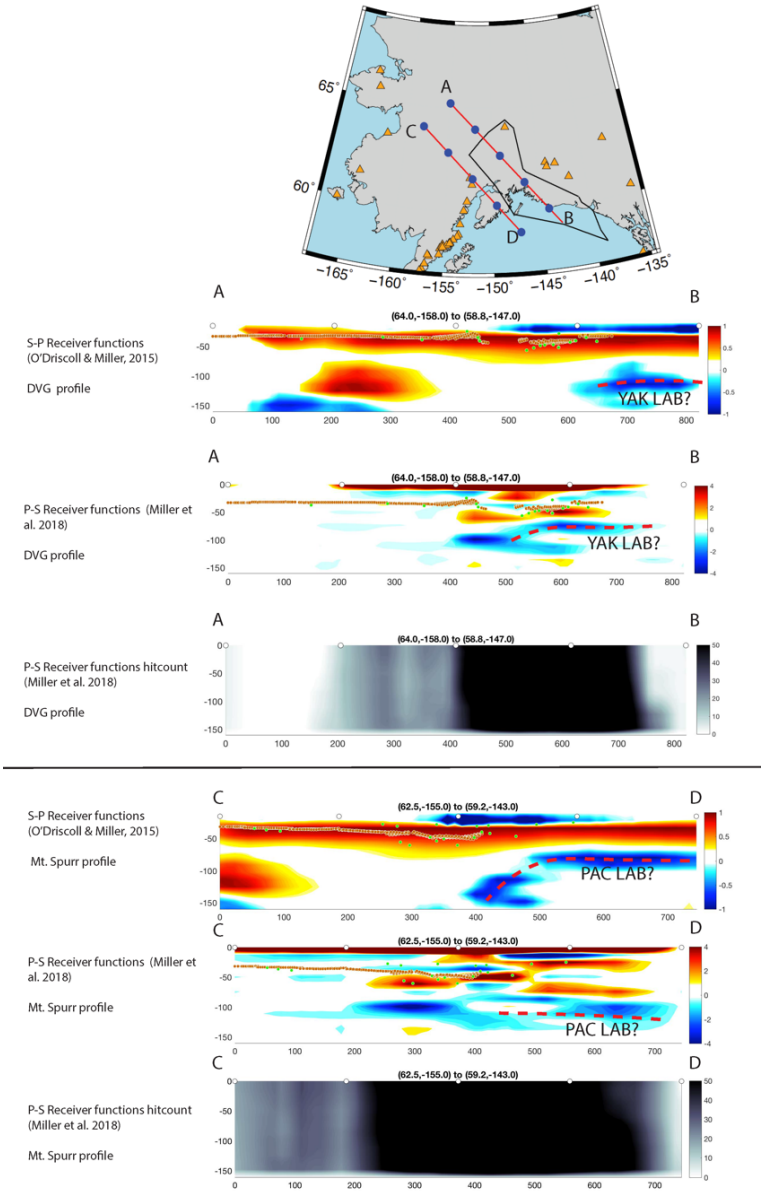

Figure 4.8: Cross sections though the receiver function CCP stacks of O'Driscoll et al. (2015) and Miller et al. (2018). Warm colors indicate positive conversions that result from fast-to-slow velocity interfaces. Cool colors indicate negative conversions resulting from slow-to-fast interfaces. Green dots indicate Moho picks from the raw receiver function stacks. Orange dots indicate the location of the Moho as inferred from our joint model. These are extracted from the map shown in figure 4.6. The upper three panels correspond to cross-section A-B (the same as figure 4.7a) while the lower three correspond to section C-D (the same as figure 4.7b). While these previous studies were more limited in their spatial coverage than ours, their discontinuity observations provide support for many of the features interpreted from our velocity model. There is good agreement between the depth of the Pacific and Yakutat LAB between these cross sections and figure 4.7, for example.

In both cross-sections, a continental LAB caps the low velocity mantle wedge asthenosphere. Below the volcanogenic region, the LAB dips northwards in such a way that it disappears beneath the Aleutian arc volcanoes (Figure 4.7b). In contrast, the continental LAB beneath the DVG is horizontal at $\sim$ 70km depth, thus separating the low velocity mantle wedge asthenosphere from the serpentinized forearc mantle at shallower depths (Figure 4.7a). The location of this horizontal LAB is similar to that of the horizontal low velocity anomaly seen below the DVG in the images of Rondenay et al. (2008), which they interpret as pooled melt below an impermeable mantle layer. This supports the suggestion of Chuang et al. (2017) that the Rondeney et al. (2008) low velocity anomaly is an expression of the continental LAB, where dry lithosphere overlies hydrated asthenosphere. Our model resolution is insufficient to rule out the melt-pocket interpretation, however, and it remains compatible with our discussion.

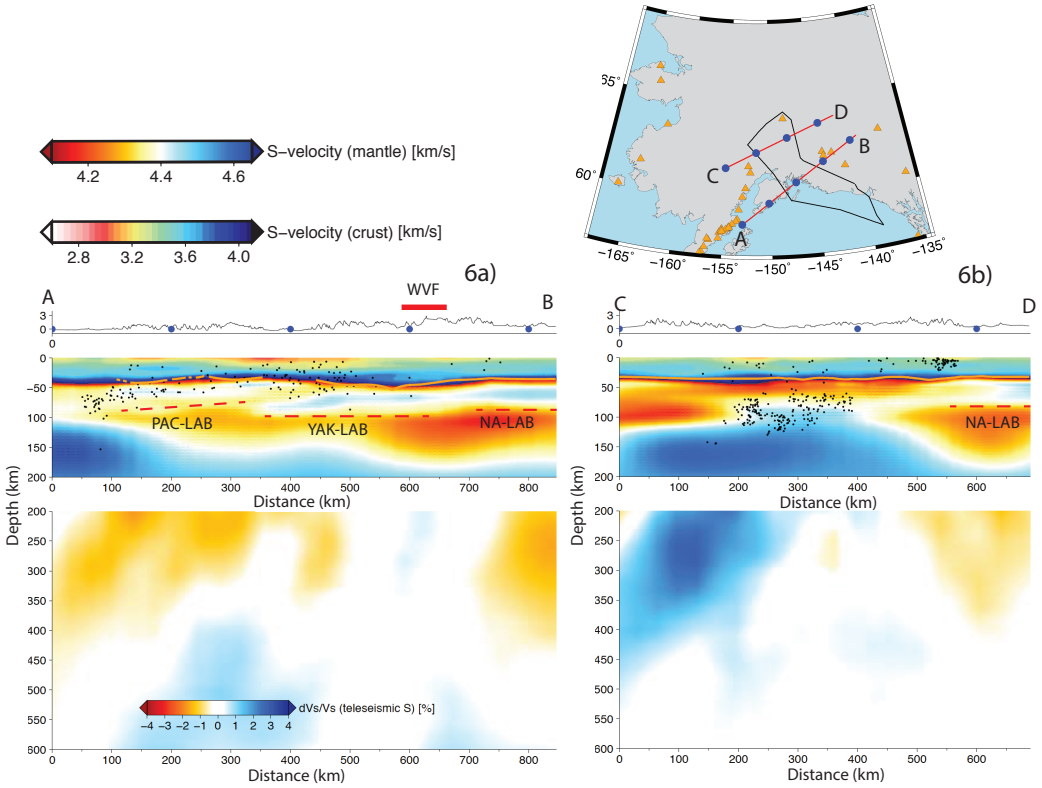

Figure 4.9: Cross-sections from the joint and teleseismic models. Section a) is taken across the northwestern extent of the Yakutat terrane, while section b) is taken perpendicular to the strike of the Wrangell Volcanic Field (WVF). The color scheme and symbols are the same as described in Figure 4.7

In the Aleutian Arc cross-section (Figure 4.7b), the dipping LAB allows low velocity mantle wedge material much closer to the surface than the horizontal LAB beneath the DVG. We

interpret this low velocity region as convecting, hot asthenosphere. In the volcanogenic zone, it is present in the mantle directly below the volcanoes, above the 100km depth contour of the downgoing slab. Fluids being released from eclogitizing oceanic crust thus enter this zone and contribute to melt production and volcanism. In contrast, the paucity of low velocity mantle wedge material above the 100km slab depth contour within the DVG, suggests the mantle wedge there is relatively isolated from asthenospheric circulation and may not be warm enough to generate sufficient melt to cause volcanism, even if slab-derived fluids are present. This is consistent with the Q tomography of Stachnik et al. (2004), which suggests that the DVG mantle wedge is anomalously cool. Cooling of the wedge and isolation from circulation can be attributed to shallowing of the slab dip angle due to subduction of the thick Yakutat crust, as indicated by the geodynamic modeling of Rondenay et el. (2010). Localized melt production must still occur in this region as evidenced by the presence of the Buzzard Creek Maars cinder cones (Figure 4.1a).

The DVG mantle wedge may also be deprived of slab-derived fluids relative to the Aleutian arc mantle wedge, which could further help to explain the observed pattern of anomalies. Chuang et al. (2017) propose the Yakutat water budget is confined to the uppermost oceanic crust, rendering the Yakutat terrane relatively anhydrous compared to the adjacent Pacific plate. Thus, most fluid is released over a relatively small depth range (60-80km), where P-T conditions prevent it from catalyzing melt production. If the catalyzing fluids are restricted to shallow depths, metagabbros in the mid-Yakutat crust can remain metastable to $>$ 100km depth, below which they experience accelerated eclogitization at pressures far above equilibrium (Chuang et al. 2017).

Our model does not constrain the relative hydration states of Yakutat and Pacific crust; nor does it allow us to distinguish between low velocity zones resulting from fluid or melt. Nevertheless, the Chuang et al. (2017) interpretation, which elucidates previously-unexplained characteristics of DVG seismicity, is compatible with our observations. Consequently, we suggest that a combination of low mantle wedge temperatures due to relative isolation from asthenosphere circulation, and low fluid content due to shallow dehydration of the Yakutat crust, explain the lack of volcanism in the DVG and its association with the Yakutat terrane. The cross sections shown in figure 4.7 support and extend the findings of O'Driscoll et al. (2015) and Miller et al. (2018), based on receiver functions alone which are shown

Eastern slab edge and Wrangell Volcanic Field

The teleseismic tomography model indicates that the deep ($>$ 150 km) slab terminates abruptly and does not extend past 148°W. This likely has important implications for asthenospheric flow (e.g. Jadamec et al. 2010). The eastern edge of the subducted material above 150km depth corresponds to the eastern edge of the Yakutat terrane as imaged by Eberhart-Phillips et al. (2006) (Figures 4.5 & 4.9). We interpret the broad high velocity zone that appears within the boundaries of the Yakutat terrane to be the subducted Yaku-

tat lithosphere, which is connected to the subducted Pacific lithosphere in a continuous arc. Given approximate ages of 50 Ma for the Yakutat terrane and 20 Ma for the adjacent Pacific plate, a simple conductive cooling calculation reveals that the Yakutat lithosphere should be $\sim$ 25 km thicker than Pacific lithosphere. This may explain why the Yakutat lithosphere is more prominent in our models (Figures 4.5 & 4.7).

Although the Wadati-Benioff zone terminates $\sim$ 85km west of the eastern edge of the subducted material, the end of tectonic tremor zone identified by Wech (2016) is well aligned with this edge (Figure 4.5d). The tremor zone occurs at depths of 50-80km, and the interevent time increases from $\sim$ 10 days in the west to $\sim$ 3 hours in the east. Wech (2016) suggests that this increase in tremor frequency documents a transition from periodic slip to continuous aseismic slip. However, we see no evidence for subducted material east of the eastern edge of the tremor zone and thus conclude this is the true slab edge. The lack of a Wadati-Benioff zone and increase in tremor frequency could thus be explained by heating of the slab edge by the adjacent hot asthenosphere.

Figures 4.5d and 4.9 suggest that the southeast to northwest trending WVF lies directly above the truncated edge of the subducted Yakutat Terrane. This is compatible with the observations of previous studies (e.g. Bauer et al. 2014; O'Driscoll et al. 2015), which also note the presence of subducted lithosphere beneath the WVF. However, these studies infer that the subducting material also extends northeast of the WVF, as would be the case in a typical subduction zone. We see no evidence for a Wrangell slab that extends northeast of the WVF in our models. Instead, we observe a horizontal Yakutat LAB that terminates directly below the WVF (Figure 4.9a). This is consistent with the SKS splitting observations of Witt (2017), which reveal a dramatic change in fast axis orientation across the axis of the WVF. This could be interpreted as a transition between sub-slab flow to flow in the asthenosphere beyond the slab edge, which parallels North American absolute plate motion. However, we acknowledge that our inability to conduct resolution tests on the joint model must limit our confidence in these interpretations.

Northeast of the edge of the Yakutat terrane, which is interpreted as the edge of the subducted material, lies a zone of low velocity (4.1-4.3 km/s) asthenosphere. This is capped by relatively fast (4.4-4.5 km/s) material at $\sim$ 70km depth, interpreted as continental lithosphere (Figure 4.9a). Geodynamic modeling predicts quasi-toroidal mantle flow around the sharp edge of the Pacific-Yakutat slab should lead to upwelling beneath the WVF, explaining volcanism there (Jadamec et al. 2010; Jadamec et al. 2012). The presence of a low velocity zone just northwest of the volcanoes supports this idea. We assert that the unusual geochemical and physiographical characteristics of the WVF, in addition to its northwestward advance over the past 23Ma, can be explained by processes occurring at the truncated edge of the Yakutat terrane and their interaction with hot, upwelling asthenosphere. The arc-wide suite of calc-alkaline lavas identified by Preece et al. (2004) could be explained by interaction between fluids derived from the Yakutat crust and this high-temperature as-

thenosphere. Melting of the slab edge itself would also explain the presence of adakites along the south-facing edge of the WVF (Preece et al. 2004). The northwestwards insertion of the Yakutat terrane beneath North America may have been associated with the formation of trans-tensional basins within the WVF (Finzel et al. 2011), which in turn provide a suitable environment for the eruption of the tholeiitic lavas reported by Preece et al. (2004).

4.8 Concluding remarks

We have presented a new absolute velocity model of the Alaskan subduction zone by jointly-inverting receiver functions and phase velocities from ambient noise tomography and earthquake-based surface wave tomography. This complements an updated version of the finite frequency, teleseismic S-wave relative arrival-time tomography model of Martin-Short et al. (2016). Recent deployment of the Transportable Array (TA) in Alaska permits the construction of tomography models of sufficient geographic extent to investigate differences between mantle wedge structure below the Denali Volcanic Gap (DVG) and adjacent Aleutian arc, and to map the geometry of the eastern edge of the slab. We draw three fundamental conclusions:

1. There is a significant difference in crustal thickness between the Southern Composite Terranes (SMCT and WCT) and Yukon Composite Terrane (YCT), which lies to the north of the Denali Fault. The largest offset occurs in central Alaska, where the Tanana Basin lies adjacent to the Alaska Range. This has been noted by previous localized studies (e.g. Veenstra et al. 2006; Ward 2015; Allam et al. 2017; Miller et al. 2018), but we are the first to observe it in a large-scale velocity model. The thickest crust in Alaska (50-55km) is found beneath the Chugach range, where crustal thickening may be the result of underplating of material from the subducting Yakutat terrane (e.g. Christeson et al. 2010).

2. A reduction in slab dip caused by the introduction of thick, buoyant Yakutat crust to the subduction zone has cooled the mantle wedge below the DVG, thickening the continental lithosphere here and thus preventing hot, convecting asthenosphere mixing with slab-derived fluids at depths where they could promote extensive melting. This contrasts with the steeper dip of the subducting Pacific plate to the west. Our interpretation is similar to that made by Rondenay et al. (2010) and supported by their geodynamic modeling.

3. We provide new constraints on the geometry of the eastern edge of the subducting slab, although our confidence is limited by an inability to conduct resolution tests on the joint model. The edge of the Yakutat terrane, as inferred from the crustal model of Eberhart-Phillips et al. (2006), closely aligns with the edge of the high velocity slab, and with the eastern limit of the tectonic tremor region (Wech 2016). We see no evidence for subducted material east of the Yakutat terrane, implying the Wrangell Volcanic Field lies directly above the truncated, northeastward-facing edge of the Yakutat terrane. Adjacent to this edge is a low velocity (4.2-4.3 km/s) zone, interpreted as hot, potentially-upwelling, asthenosphere.

Melting of the slab edge by this material, interaction with fluids derived from the Yakutat crust, and extension of the overlying crust within trans-tensional basins, may explain the unusual geochemistry and age progression of the WVF.

Finally, our model provides a platform on which further imaging studies of this region can build. Such work could, for example, seek to quantify the uncertainties in our joint model though a Monte-Carlo inversion approach (e.g. Shen et al. 2012). The resolution of our models might also be improved though the joint inversion of Rayleigh wave group, Love wave phase and group velocities along with the Rayleigh phase observations made here. Future studies might also seek to jointly invert body and surface wave observations to produce a single model capable of resolving features from the crust to the mantle transition zone in order to gain a more self-consistent picture of the subduction zone at a large scale.

A full published version of this paper can be found at https://doi.org/10.1029/2018GC007962. The supporting information for this paper contains more detail about the methodologies, resolution and model testing.

This chapter greatly extends the tomography work presented in chapter 2 by applying multiple seismic imaging techniques with complementary strengths to the same, large seismic dataset in order to produce the most comprehensive velocity models possible for the Alaska region. Our models could be used as starting points for more advanced imaging techniques such as full waveform tomography, but alone they provide a valuable recourse for the community seeking to understand the tectonics of Alaska and particularly the slab geometry. Perhaps the most important finding to come out of this Alaska imaging work is the idea the the Wrangell Volcanic Field formed at a slab edge, which is supported by multiple subsequent geochemical and imaging studies (e.g. Ward and Lin 2018; Jiang et al. 2018)

An important component of this chapter not explicitly mentioned in the text was the detailed documentation of the various software packages use to produce the velocity models and the data processing workflow required to use them. This documentation is available for use by future students in the Berkeley Seismic Laboratory.

4.9 Chapter acknowledgments

We thank C. Tape and one anonymous reviewer for helpful comments. All seismograms come from the Incorporated Research Institutions for Seismology (IRIS) Data Management Center, which is funded through the Seismological Facilities for the Advancement of Geoscience and EarthScope (SAGE) Proposal of the National Science Foundation under Cooperative Agreement EAR-126168. TA network data were made freely available as part of the EarthScope USArray facility, operated by IRIS and supported by the National Science Foundation, under Cooperative Agreements EAR-1261681. Ambient noise phase velocities were constructed

using CU-Boulder software. Earthquake-derived phase velocities were determined using the ASWMS software. Figures were created using the Generic Mapping Tools (Wessel & Smith 1998).

Part II

Simulating the ability of MyShake networks to detect and locate earthquakes

Chapter 5

Towards Global Earthquake Early Warning with the MyShake Smartphone Seismic Network

Advisor: Richard M. Allen

Collaborator: Qingkai Kong

5.1 Introduction

Earthquake Early Warning (EEW) is a technology that uses networks of seismometers to quickly determine the location and magnitude of an earthquake after it has begun and issues warnings to regions anticipated to experience intense shaking (e.g. Allen et al. 2009). Such alerts are typically issued within seconds of the earthquake origin time and can provide up to several minutes of warning depending on the geometry of the monitoring network and distance between the event and population centers (Allen et al. 2003; Allen et al. 2009). During this warning time, actions can be taken by individuals and organizations that could potentially save lives and mitigate damage (Strauss et al. 2016). In order to be effective, EEW requires the existence of a dense seismic network that has the capability of real-time monitoring of potential earthquake signals. The closer the instruments are to the epicenter, the faster the detection and hence the larger the warning times can be. EEW has been developed mainly using traditional seismic and geodetic networks, which are costly to operate and only exist within a small number of countries (Allen et al. 2009). Much of the global population at high risk from earthquake damage thus currently is not benefitting from EEW.

Many alternative, cheaper, non-traditional networks have been proposed, including micro-electromechanical system (MEMS) accelerometers installed in buildings, USB accelerometers attached to personal computers or other low-cost sensory equipment (Luetgert et al. 2009; Clayton et al. 2015; Cochran et al. 2009; Chung et al. 2011). Although promising, these ideas suffer from the same major disadvantage as traditional networks because they require physical installation and maintenance from the network operators, which hampers the sustainability and expandability of the EEW system, especially in remote regions.

Recent advances in mobile accelerometer technology mean that smartphones are becoming a viable alternative to fixed seismometers as the primary sensing instruments for EEW (e.g. Kong et al. 2016; Finazzi 2016; Dashti et al. 2014). Furthermore, there is also interest in the development of the smartphone networks that use GPS and users app launching times to detect earthquakes (Minson et al. 2015). There are many advantages of using smartphone networks for this application: The devices are globally ubiquitous, even in regions without traditional earthquake monitoring. Since the hardware is maintained by the users, the only requirement for the network operators is to develop and market a software application that can made accessible via the Google Play or Apple IOS store. This makes the network easier to maintain and grow.

However, the use of smartphones for earthquake early warning is not without its challenges. Namely, the detection software must be capable of reliably distinguishing between earthquake shaking and all other vibrations that the device might experience. Furthermore, the noise floor of mobile accelerometers is significantly higher than that of traditional seismometers, the extent of coupling between the smartphone and the ground may be poor and the recording of earthquakes is not a priority for users.

MyShake is a smartphone application that developed at Berkeley Seismological Laboratory to monitor the accelerometer data to detect earthquakes. It uses an artificial neural network (ANN) trained on examples of earthquake and non-earthquake waveforms and is able to successfully classify earthquake motions from the human activity motions recorded on the phone (Kong et al. 2016). The MyShake application monitors the accelerometer on the device and sends real-time messages containing time, location and ground acceleration to a server when earthquake-like motions are detected. Kong et al. (2016) should be consulted for a complete description of MyShake application operations. Since its first public release in February 2016, MyShake phones have successfully recorded useful seismic waveforms from 900 earthquakes worldwide and the app has approximately 300,000 downloads and 40,000 active users, with approximately 6000 devices making daily data contributions. The data recorded by MyShake shows great potential in various applications, such as earthquake early warning, mapping ground motion (Kong et al. 2016), routine seismic operation, building health monitoring (Kong et al. 2018), and dense array detection. EEW is clearly an exciting application area for this global seismic network. However, due to the fact that the current network is relatively sparse, especially outside the US, the potential for MyShake

networks to contribute to EEW has not been systematically assessed beyond a handful of basic simulations. Such assessment is vital before MyShake can begin to issue public early warnings globally, because the usefulness of MyShake networks for early warning will vary from region to region, depending on a wide range of factors such as the distance between population centers and active faults, the density and distribution of MyShake users and the origin time and magnitude of the earthquake. Quantification of these factors will allow the MyShake development team to identify regions of the world where earthquake early warning with MyShake would be most beneficial, the minimum number or density of users required for accurate, rapid detections and the likely warning times that could be issued to major population centers in the event of large earthquake.

This study describes a simulation platform that has been built to understand the performance of MyShake networks at various regions around the globe. The platform is built on top of MyShake observations with the aid of a simple physics model and a series of machine learning algorithms which can be used to test and understand the whole MyShake workflow from individual phone triggers to the final detection of the earthquake and estimation of the alerting area. The challenges associated with this dynamic EEW system can also be assessed using our simulation platform. It can simulate trigger times and ground acceleration values that might be expected from hypothetical MyShake networks responding to given input events and various population densities. The locations, times and ground motions reported by individual phones are then provided to a network detection algorithm, which first determines whether or not an earthquake is occurring and then uses the trigger information to estimate the earthquake's location and magnitude. Once the earthquake has been located, the system estimates the radius of the region expected to experience shaking of intensity ≥ 4, for which a warning could be issued. As the simulation proceeds, the earthquake hypocenter parameters can be updated as more trigger information becomes available.

We test our network detection workflow on real data collected from devices running MyShake during the June 2016 M5.2 event in Borrego Springs and January 2018 M4.4 event in Berkeley, CA, which are currently the locations with the highest density of MyShake users. Had the system been operating at the time, it could have provided about 6 seconds of warning before the arrival of strong shaking in Palm Springs, more than 20 seconds to Los Angeles (LA), and several seconds to much of the San Francisco bay area. This confirms the ability of MyShake networks to issue useful early warnings. Following this test with real data, we conduct simulations for all historical earthquakes $M > 4.0$ since January 1st 1980 for a range of earthquake-prone regions around the world, namely Southern California, New Zealand, Nepal, Chile, Haiti and Sulawesi (Indonesia). The platform can be used to simulate earthquake detection anywhere in the world, but these regions were chosen specifically because they represent a wide range of tectonic environments, population distributions and levels of socioeconomic development. An addition, each region has been affected by a major earthquake in recent years.

For each region, we assume that 0.1% of the total population are MyShake users, which is the approximate proportion of the population of the LA region that have download the app to date. These simulations allow us to assess the general performance of the network detection workflow in each region with this density level of users, determine the spatial and magnitude distribution of events that could be detected and report their expected warning times and location errors. Furthermore, we conduct a suite of 200 simulations of the single most damaging event in each region. This provides the distribution of errors in origin time, epicenter location and magnitude that might be expected for these events given different samplings of the population.

Our results indicate that the MyShake network detection algorithm is able to reliably detect and locate events greater than M5.0 and issue warnings within about 10 seconds of the origin time. The performance is poorer in subduction zone settings with most of the MyShake users lying on the one side of the earthquake, such as Chile and Central America, where the events are typically large, deep and offshore. This can lead to larger errors in magnitude and location, but would still enable the MyShake network to provide valuable seconds of warning time to populations lacking traditional EEW capabilities. Overall, we show that at a penetration level of 0.1% of the population, MyShake would provide accessible, useful earthquake early warning to communities worldwide.

5.2 Overview of the simulation platform

Our simulation platform consists of several components, which are shown in Figure 5.1. These components can be divided into two main functionalities. The first is a mechanism for simulating MyShake networks and their response to earthquakes. This component is supplied with the coordinates of the region of interest, the proportion of the population of that region assumed to be MyShake users and the parameters of the earthquakes (i.e. location, origin time, magnitude) to be simulated. At each timestep of the simulation, ground acceleration values at each device are estimated and used to determine if the device will 'trigger'. The trigger data is then collected and passed to a network detection algorithm to confirm this is the occurrence of an earthquake. Although hypothetical by nature, this simulation component builds upon observations of real MyShake networks in determining the network configuration, and in setting thresholds for device triggering in addition to uncertainties in the reported times and acceleration values.

The second function is a network detection algorithm that takes trigger times, locations and ground acceleration values from the triggered phones in the MyShake network and uses them to 1). Determine if the network is experiencing an earthquake and 2). If an earthquake is occurring, estimate its location, origin time and magnitude as quickly as possible. This algorithm can be run on data received by real MyShake devices as in our Borrego Spring and Berkeley test cases, or from simulated triggers. This tested version of the network detection

algorithm will be implemented in the a future release of the MyShake mobile application to detect events in real time and issue warnings.

In this section we describe each stage of the MyShake simulation workflow, beginning with sampling the population, through simulating triggers on a device level to the details of our network detection algorithm. At each stage we note the parameters that can have a significant impact on the results and justify our choice of values for them.

Sampling the population

Prior to each simulation, we need to determine the spatial distribution of the simulated MyShake network. This is done by inputting the fraction of the population of the region of interest assumed to have the MyShake application installed on their mobile device, currently, we use a default value of 0.1%. User locations are then found by randomly sampling cells of a 1km by 1km grid of the area of interest with a sampling probability weighted by the population in that cell. The world population data is obtained from the 2015 Gridded Population of the World, Version 4 (GPWv4). Once a cell has been identified, the coordinates of the simulated device are drawn from a uniform distribution within the cell. This procedure allows for random sampling of the population that takes density into account, naturally leading to a greater density of simulated devices in urban areas.

Determining steady phones

In current MyShake applications, only the steady phones will be monitored to detect earthquakes and record their waveforms. Therefore, we use a relationship based on data from the existing global MyShake network to estimate the proportion of active devices that are 'steady' given the origin time of the event to be simulated. The proportion of MyShake devices that are steady varies significantly over each 24 hour cycle, which reflects the temporal, dynamic nature of the network and is shown in the Figure 5.2. Figure 5.2 indicates that the network has more phones steady for detecting earthquakes at night than in the daytime. This difference is encoded into the simulation platform.

Determining which phones will trigger

The triggering mechanism of individual phones for the current simulation platform is determined by an amplitude based approach. Ground motion accelerations associated with P and S-waves at each device are estimated using the distance-magnitude relationships developed by Cua & Heaton (2009), which, given an event magnitude and distance, return the mean and standard deviation of the estimated ground motion distribution for P and S waves separately. These relationships are empirical, based on observations from earthquakes in southern California and known to saturate for events of $M \geq 6.5$ (Cua & Heaton, 2009).

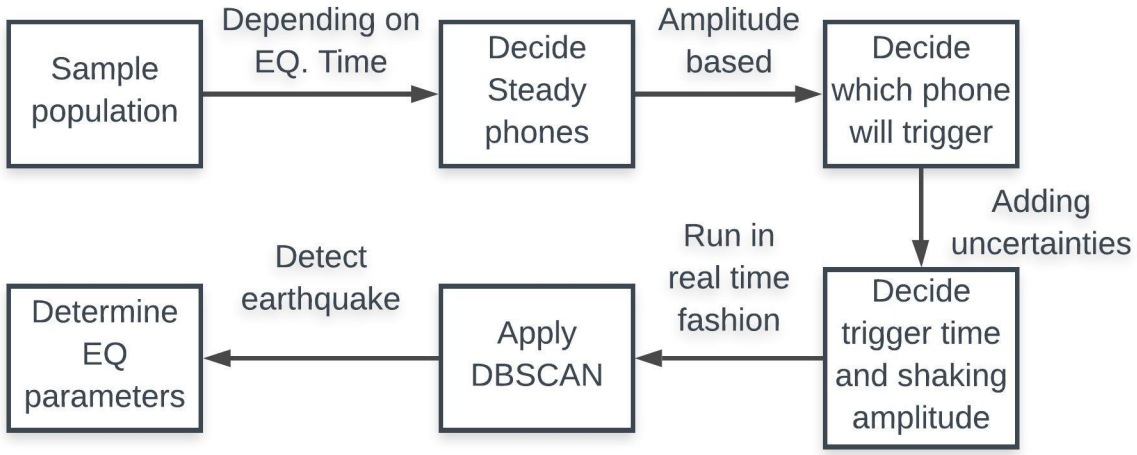

Figure 5.1: Workflow for the MyShake simulation platform. Figure courtesy of Qingkai Kong

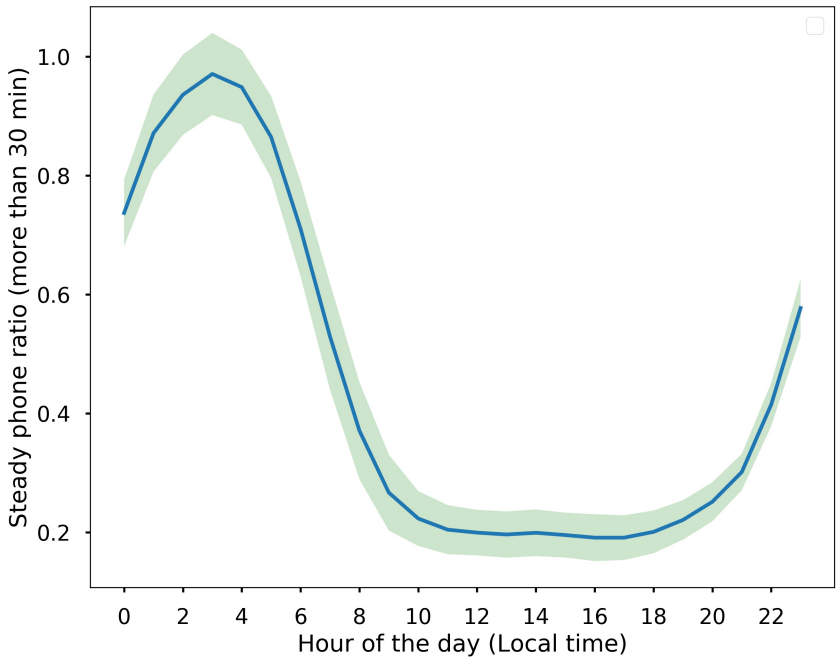

Figure 5.2: Percentage of phones that are steady for more than 30 minutes during each hour of the day. The solid line is the average percentage, while the shaded area is the standard deviation. The data used here is from MyShake users between 2017-07-01 to 2018-07-01. Figure courtesy of Qingkai Kong.

Nevertheless, they provide a convenient and relatively accurate way for us to estimate ground motion values for both P and S phases anywhere in the world.

The ground motion associated with each device is then sampled from the normal distribution returned by the Cua and T. H. Heaton (2009) relationships. If the reported ground acceleration value at a device exceeds 0.01g, the phone will have a triggering probability of 1. Below this threshold, the phone will have a triggering probability define by p = amplitude / 0.01. The 0.01g threshold is determined by the observation that the majority of phone triggers from the real MyShake network have the amplitude larger than 0.01 g at the trigger time. After determining this triggering probability, it is scaled by a factor of 0.8, which accounts for situations in which the trigger is correctly sent. This can happen, for example, if for some reason the phone doesn't send the data to the server successfully, or is in a location that severely attenuates the trigger amplitude.

Analysis of real MyShake triggers has indicated that it is possible to discriminate between whether the phone has triggered on a P or S phase by calculating the ratio between the maximum amplitude recorded on the vertical component and the maximum value on the horizontal components in a 2-second window around the trigger. Our tests indicate that this phase discrimination procedure has an accuracy of about 70%, so in the trigger simulation workflow the code generates an accurate phase label with a probability of 0.7 to indicate whether the trigger is a P-wave or S-wave trigger. Random triggers are also simulated at a rate determined by the triggering rate from the data collected by the MyShake network at each hour of the day. Then at each timestamp, we will use the random triggering rate to determine how many phones in the region will send false triggers with random amplitudes.

Determining trigger times and ground motion amplitudes

We assume constant P and S-wave velocities of 6.10 and 3.55 km/s respectively for a half-space model, which allows us to determine travel times of P and S waves to each device. This is clearly an oversimplification of the true velocity structure but the errors it introduces are likely to be small compared to all the other uncertainties in the MyShake network detection workflow. In order to account for uncertainties in the observed trigger times from real events due to the wrong clock time on the phone, or the phone simply not triggering on the onset of the P wave due to high-noise level, we sample P triggers from a half-normal distribution with a standard deviation of 2 seconds centered at the predicted P arrival time and S triggers from a normal distribution with a standard deviation of 1 second centered on the predicted S arrival time. The acceleration amplitude for the triggered phone is the amplitude calculated by the Cua & Heaton (2009) relationship that is used to determine the triggering probability.

Figure 5.3 shows a comparison between trigger times recorded by MyShake devices during the 2016 M5.2 Borrego Springs event in southern California and those simulated by the trigger generation algorithm assuming 0.1% of the population are MyShake users for the same event.

We can see the triggers that are associated with P and S waves, as well as the random triggers in both cases. It is clear that the simulation is able to capture the general characteristics of how the MyShake network responds to events. But also this simple amplitude based approach losses more P-wave triggers at further distances than the ANN algorithm used by MyShake in this case. During the development of the triggering mechanism, we also tried using the Southern California Earthquake Center (SCEC) Broadband platform (Maechling et al. 2014) to generate earthquake waveforms from M4.0 to M8.0 at a very dense grid-station configuration, and evaluated the ANN algorithm's triggering performance. However we found that the SCEC Broadband platform doesn't generate realistic high-frequency P wave components to trigger the algorithm.

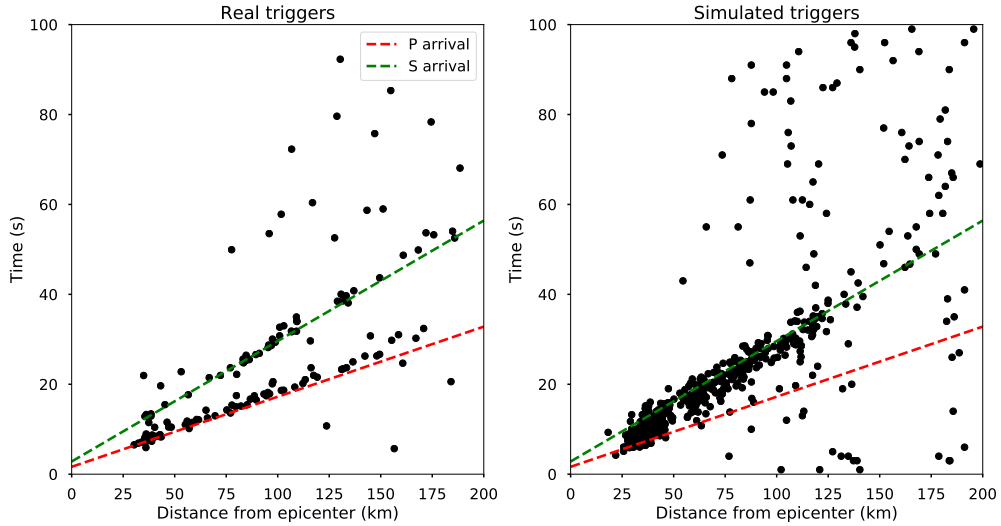

Figure 5.3: Actual and simulated trigger times as a function of epicentral distance for the June 2016 M5.2 Borrego Springs earthquake. The red and green lines show the predicted arrival times of the P and S phases assuming constant velocities of 6.10 and 3.55km/s and an event depth of 10km. These three parameters are fixed in all simulations.

Network detection with modified DBSCAN clustering

Our network detection workflow has the task of using either simulated or real-world trigger information to quickly detect that an earthquake is occurring and then determine its origin time, magnitude and hypocenter parameters. MyShake networks present unique challenges for rapid network detection when compared to traditional seismometers. These include the fact that the network configuration varies over time, triggers can be either P and S waves, potential inaccuracies in trigger timing data due to an inaccurate phone clock or the high noise floor. Finally, the detection algorithm must be capable of accounting for spurious or random triggers that are caused by non-earthquake shaking. The network detection problem essentially is a real-time spatio-temporal clustering problem. We applied a modified version

of density-based spatial clustering machine learning algorithm - DBSCAN (Density-Based Spatial Clustering of Applications with Noise) (Ester et al. 1996) to tackle these challenges.

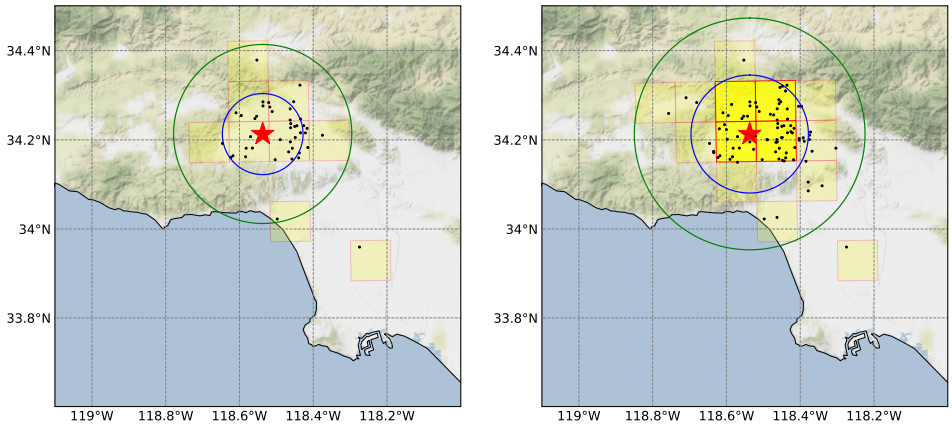

Figure 5.4: Visualization of the detection process during a simulation of the 1994 M6.7 Northridge earthquake in Los Angeles. The panel on the left shows the situation four seconds after the origin time. Black dots represent MyShake devices that have triggered since the start of the event. Yellow squares are the MGRS grid cells known by the algorithm to contain triggers. The green circle represents the estimated location of the P-wave front at this time, while the blue circle shows the location of the S-wave front. An earthquake has not yet been declared because there are insufficient triggers to 'activate' two or more cells. The panel on the left shows the situation at five seconds after the origin time. Four cells (highlighted in yellow) have now activated and they have been clustered to represent a single event. Triggers within these four cells are then used to estimate the event location and magnitude.

To make the DBSCAN algorithm more reliable and speed up the processing in real-time, we divide up the region of interest into grid cells using the Military Grid Reference System (MGRS) (Lampinen 2001) with 10 by 10 km resolution. Each cell is assigned a weight that can be considered a measure of its reliability in the detection algorithm. The weights are calculated by dividing the number of triggers in each cell by the number of steady phones in the cell, and they are updated during the event as more information becomes available. If a cell contains more than five steady phones and the weights are above 0.5, then it is designated a possible candidate for clustering, or we say that the cell is 'activated'.

Once two or more cells are activated, the DBSCAN clustering algorithm will start to try use the centroids of these cells to form clusters in order to determine if an event is occurring. The advantages of using DBSCAN are (1) there is no need to specify the number of clusters, (2)

the algorithm can automatically label the noisy data points that not belong to any clusters. The DBSCAN algorithm has two parameters: `epsilon` (the parameter for the radius) and `min_samples` (the parameter for setting the minimum number of points within a sphere to grow the cluster). The algorithmic steps are: (1) for each centroid in the activated cells, we draw a 2-dimensional circle of radius epsilon around the centroid. (2) If the number of centroids inside the circle is larger than the `min_samples`, we set the center of the circle as the cluster, and all the centroids within the circle belong to this cluster. (3) Loop through all the centroids within the circle with the above two steps to grow the cluster whenever the centroids satisfies the two rules. (4) Centroids that do not belong to any cluster are ignored and treated as noisy outliers. By default we set the `epsilon` to 200 km and `min_samples` to two grid cells. Once there are clusters formed, each cluster of cells reported by DBSCAN represents a single event. This approach effectively prevents random triggers from being considered part of an earthquake cluster. Furthermore, because DBSCAN is a density-based clustering algorithm that does not require a user-specified number of centroids, the network detection algorithm has the capability of detecting multiple earthquakes simultaneously. This is essential if it is to be run continuously on a global network. A visual explanation of this clustering approach is shown in Figure 5.4.

Each cluster of cells contains triggers that can be used to locate the event associated with that cluster. This is done by finding a hypocenter location and origin time that minimizes the following objective function, which is a weighted sum of square residual travel times

$$J(X, Y, T) = \sum_{i=1}^{N} w_i((t_i - T) - \frac{D_i}{v_{ps}})^2$$

$$D_i = \text{Distance}(\text{trigger latitude}_i, \text{trigger longitude}_i, X, Y)$$

where w_i is the weighting of the MGRS cell containing the trigger i, t_i is the trigger time, T is the origin time of the event, D_i is the distance between trigger i and the event location, and v_{ps} is the velocity of the phase predicted to have caused the trigger. X and Y above are the event latitude and longitude. The workflow has access to phase information from the triggers. We assume the fixed event depth 10 km and choose a suitable X, Y and T such that the objective function $J(X, Y, T)$ is minimized.

If the minimization fails to converge within 5000 iterations of the Nelder-Mead method (Nelder et al. 1965), a grid search for the optimal location and origin time is carried out. The grid search approach is more time consuming and less accurate due to constraints imposed by the grid step size. However, in practice the optimization fails in less than 5% of all the simulated cases.

Once the event has been located, its distance from each trigger is determined and its magnitude is estimated by providing the distance and ground acceleration value to a random forest regressor trained on synthetic ground accelerations. The training set is generated by applying the Cua & Heaton (2009) amplitude relations to a range of synthetic magnitudes and distance values, with magnitudes from M3.5 to M9.0 in steps of 0.1 and distance from 1 to 300 km in steps of 1 km. Essentially, the random forest model encodes the ground motion relationships into a simple map from epicentral distance and the ground motion acceleration to magnitude. The inputs into the model are the logarithm of epicentral distance and ground motion acceleration, and the output is the magnitude of the earthquake.

After testing several approaches, we found that training two separate random forest models for P and S wave triggers yields the best results. Separate random forest regressors are trained for magnitude estimation from P and S wave amplitude information, with each trigger being passed to the appropriate model according to its associated phase flag. The final event magnitude estimate is then given by the mean of these trigger magnitudes. To test the performance of the trained random forest, we randomly generate accelerations for 100 triggers (mixed with P and S) at for each magnitude from the range of M3.5 to M9.0 with distance randomly sampled from 1 to 100 km. We then provide acceleration and distance from these 100 triggers at each magnitude to the trained random forest models to estimate the magnitude. The performance of this magnitude estimation approach is elucidated in Figure 5.5, which shows the results of the random forest models applied to this test set. The models exhibit good performance up to magnitudes of about 7.0, albeit suffering from some overestimation at low magnitudes. However they are seen to saturate for larger events, which is a known limitation of the Cua & Heaton (2009) relationships.

As time progresses beyond the initial earthquake location step, shaking emanates from the hypocenter in a characteristic pattern governed by the speed of P and S waves. In order to improve the initial location estimate, our network detection algorithm can perform a series of updates using additional trigger information as it becomes available. Any additional triggers must be either associated with an earthquake or discarded if they are spurious. The association of new triggers to the detected events is done by checking if the trigger time of the device within a time-space box for P and S waves. This update step is set to occur every 0.5 seconds, with all the triggers associated with the events, but this value could eventually be adjusted dynamically to take population density into account. The location of the event, origin time and the magnitude of the earthquake are all updated with the arrival of the new triggers until the user-specified number of updates is reached.

The alerting area currently set in the simulation platform is the area with shaking intensity above MMI 4. The shaking intensity is calculated based on the relationship described by Worden et al. (2012).

The network detection algorithm uses several user-defined parameters that can have the

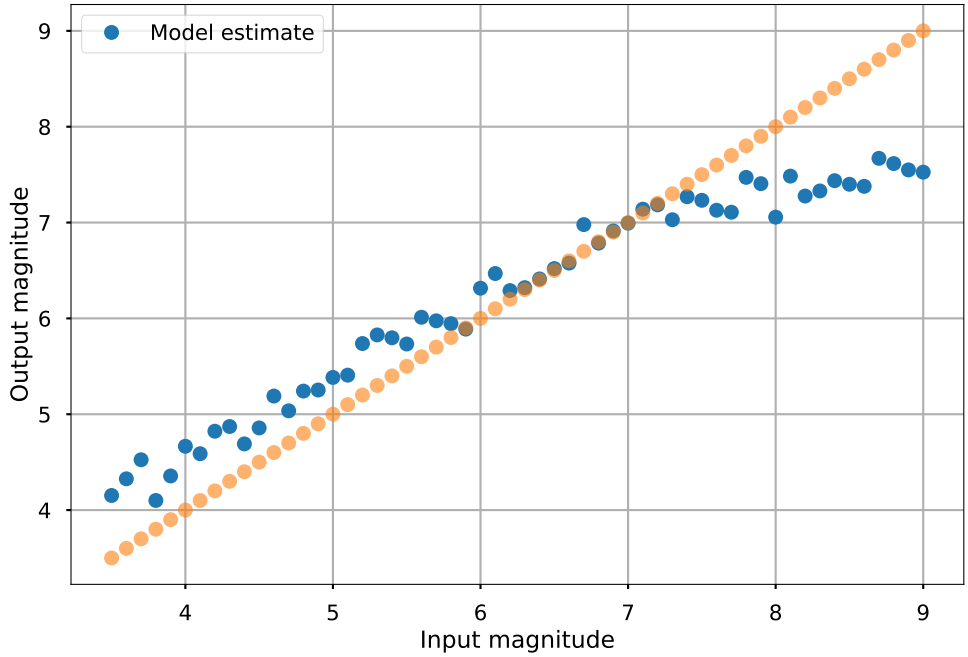

Figure 5.5: Estimated event magnitudes using our magnitude estimation workflow. This test dataset consists of trail events with magnitudes between 3.5 and 9.0. For each event, 100 trigger distances are drawn from a uniform distribution between 0 and 100 km from the event. Then for each trigger, the Cua & Heaton (2009) distance-amplitude relationships are used to estimate a ground acceleration distribution, from which a value was randomly drawn. The generated P or S wave triggers will have a 70% chance of having their phase labeled correctly. Subsequently, triggers flagged as 'P' are provided to a random forest regressor trained solely on P-wave amplitudes, and triggers flagged as 'S' are provided to a separate regressor trained on S-wave amplitudes. A single magnitude estimate is given for each trigger and the mean of these estimates over all triggers becomes the output magnitude. This workflow exactly emulates the simulation platform.

potential to exert significant influence on its performance in the real world. These include the minimum number of steady phones required in each MGRS grid cell, the fraction of these steady phones that need to trigger before the cell is considered for clustering and the size of the cells themselves. In practice, adjustment of these parameters provides a tradeoff between the speed and accuracy of detection. Typically, the more triggers that must be accumulated before an event is declared, the more accurate the location but the longer the alert time. Conversely lowering the thresholds for detection will lead to faster alert times but also makes it easier for spurious triggers to influence the detection. Thus, when this network detection algorithm is applied to real MyShake networks, it is likely that the parameters will need to be adjusted from region to region in order to provide optimal results.

5.3 Events recorded by the existing MyShake network

Although the MyShake mobile application has achieved global recognition, there are currently only a small number of regions where the network of users is approaching densities sufficient for effective early warning due to the infrequent of the earthquakes. Only two of these regions, the San Francisco Bay area and the Los Angeles area, have experienced sizable earthquakes since the launch of MyShake. This in part explains our reasoning for the creation of the simulation platform, which allow us to test wide range of hypothetical scenarios around the world. However, as a test of our network detection algorithm, we used it with triggers from devices that returned data during the January 4th 2018 M4.4 Berkeley and June 10th 2016 M5.2 Borrego Springs events.

The Berkeley M4.4 event occurred directly beneath an urban area. We input these triggers into the network detection workflow and instruct it to perform five updates after the initial parameter estimation stage. Figure 5.6 shows the time of first alert sent out with the initial location and magnitude estimation of this event. Because of the relatively high density of MyShake phones in the city of Berkeley, we found that setting the MGRS grid cell size used for clustering to 1 km by 1 km cells and the minimum number of steady phones required within each cell to two improved our results compared with their default values of 10 km resolution and six phones. With this adaption, we can see that the first alert is sent out 5.7 seconds after the origin time of the event, which gives the centers of San Francisco and San Jose 0.7 s and 13.3 s warning time respectively. This illustrates the need to have an adaptive thresholds for different regions depending on the density of the network. However, even with the default values the event is detected within 6.7 seconds of the origin time, providing several seconds of warning for much of the San Francisco Bay area before the arrival of the S wave. The initial location has a relatively small epicentral distance error of 4 km, and remains very close to this value during the subsequent updates. The magnitude of the event is slightly overestimated, as expected given the test shown in Figure 5.5, but we can see that the estimated intensity is slightly higher for various locations for both cases. This test suggests that had the network detection algorithm been operational during this event in

2018, it would have successfully provided early warnings.

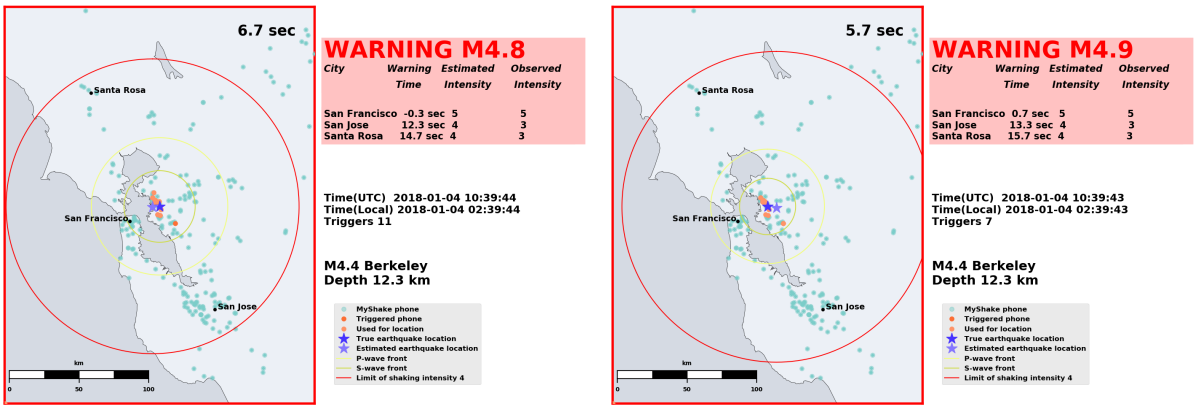

Figure 5.6: Initial performance of the network detection algorithm using real MyShake triggers to detect and locate the January 2018 M4.4 Berkeley event. Both panels correspond to the moment of first location of the event. Panel A shows performance with the default settings of 10 km resolution MGRS grid cells for clustering and a minimum of 6 steady phones required in each cell in order for it to be considered for clustering. Panel B shows the result with parameters modified to optimize detection speed, with 1 km resolution MGRS grid cells and a minimum of two steady steady. Blue dots are devices running MyShake, while orange dots are devices that actually triggered. The figures also show the estimated positions of the P and S wavefronts at the time of location and the estimated radius of shaking intensity greater than MMI 4 (the large red circle). When optimized for detection speed, the algorithm locates the event using 7 triggers within 5.7 seconds of the origin time, providing at least one second of warning to much of the San Francisco bay area.

The Borrego Springs event poses a more challenging test of the network detection algorithm because it occurred in a remote location about 50 km south of Palm Springs, where all of the initial triggers are located. Thus the initial azimuthal distribution of triggers is not ideal and the algorithm must be capable of associating later triggers to the same event, even though they occur at great distance from the original cluster. It is important for any network detection workflow to deal with such a situation, since it will be common in regions featuring major faults far from population centers. Despite these challenges, using its default settings, our network detection algorithm performs relatively well, locating the event with an initial error of about 14 km and a magnitude underestimation of 0.3 units. 5.5 seconds of warning time is provided to Palm Springs and people near San Diego would receive a warning of about 40 seconds. The radius anticipated to experience shaking of intensity 4 is denoted by the red circle in Figure 5.7. This is the region within which warnings could be issued.

These tests provide a us with an elementary indication of how our workflow might be ex-

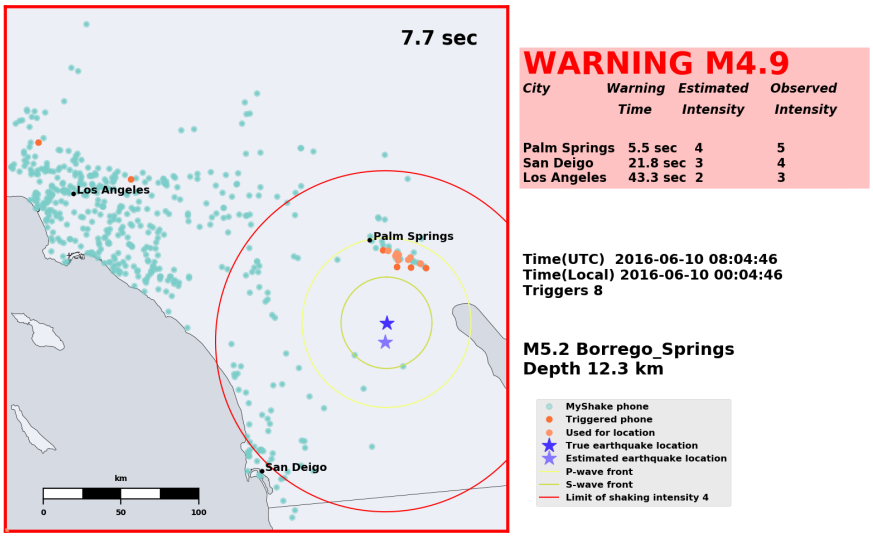

Figure 5.7: Performance of the network detection algorithm using real MyShake triggers from the M5.2 Borrego Springs earthquake. This panel shows the network detection algorithms performance at the moment of first alert. 8 triggers, all of which appear to occur on arrival of the P-wave in the Palm Springs area, are used to initially locate the event.

pected to perform in hypothetical future earthquake scenarios. However, these are only two examples in California of a plethora of earthquake-network configurations, and feature considerably fewer phones than we might expect in future as MyShake gains popularity around the world. Therefore, we developed the simulation platform to understand the performance of the system in different regions, which is discussed in the next section.

5.4 Simulations of historical events

In order to assess the potential benefits of using MyShake networks for EEW on a global scale, we perform a suite of simulations using historical events around the world as shown in Figure 5.8. For each region, we use the MyShake trigger generation workflow to produce triggers for all events $M > 4.0$ from January 1st 1980 to April 1st 2019 assuming that 0.1% of the population is running the mobile app. The simulated triggers for each event are then provided to the network detection algorithm, which is instructed to report an estimate of the event parameters for the first alert. Using the historical catalog in this way allows us to assess the typical magnitude range and proximity to population centers of events in each region and thus comment on the performance of the system. Although a full exploration of the parameter space required to determine exactly what effects specific features of a region have upon algorithm performance, our hope is that this analysis will give us a first order

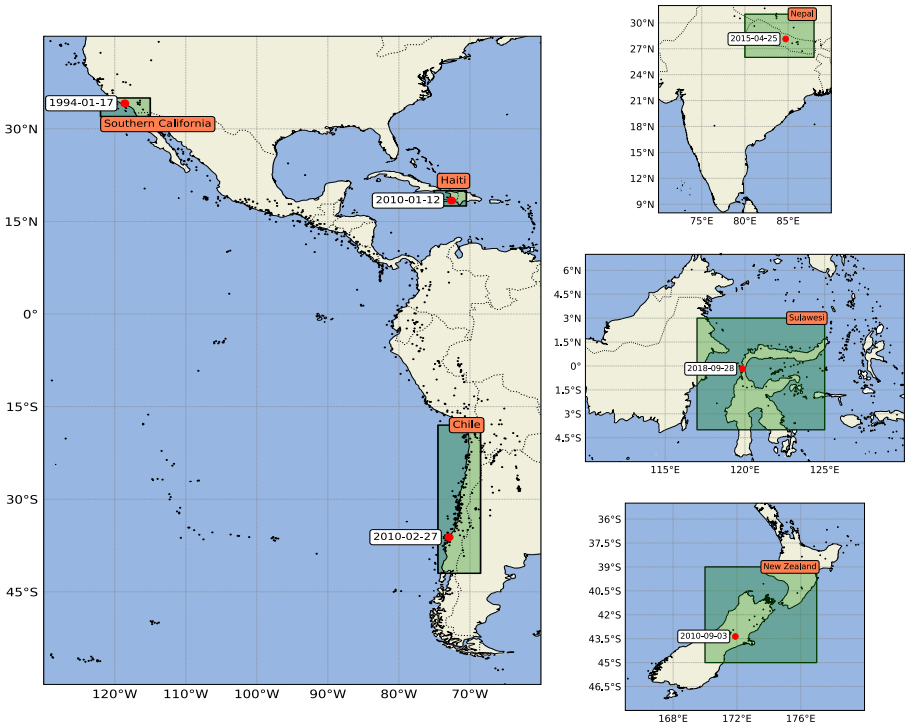

Figure 5.8: Regions of the world where we have tested the MyShake simulation platform. Labelled boxes show the geographic extent of each region, which chosen because they encompass major population centers and the sites of significant historical events, whose epicenters and dates are labelled. Together these regions also represent a wide range of tectonic regimes, population densities and socioeconomic development levels. Black dots are the locations historical events M $\geq$ 6.0 since 1980.

estimation and understanding of the MyShake performance at various regions.

Each of the six regions we choose has also experienced a major, damaging event in recent years. In order to assess the combined impact of the various uncertainties built into the population sampling, trigger generation workflows and the stability of the performance of the system, we conduct a suite of 200 simulations for each of these large events and report the distribution of location, magnitude and timing errors. This is important because the uncertainties we incorporate into our calculations of trigger times and ground accelerations on a device level represent our best understanding of how MyShake devices perform in practice. It is important to note that for simplicity we model these events as point sources, which ostensibly they are not, meaning that in practice the true distribution of ground acceleration values that would have been observed by a MyShake network may be quite different from our simple models. Nevertheless, the shapes of the error distributions returned

by the network detection algorithm provide us with some indication of the best and worst case performance scenarios for a major earthquake in each region.

Our six selected regions are shown in figure 5.8. They represent a wide range of tectonic settings, population distributions and levels of socioeconomic development. These three factors combine in a complex fashion to determine the usefulness of MyShake as an EEW system in each region.

Southern California

Southern California is one of the world's most well-studied regions in relation to earthquake hazard. The presence of the on-land, strike-slip boundary between the Pacific and North American plate, which manifests itself in the San Andreas fault zone, is responsible for seismic activity here. The seismogenic zone typically lies within the uppermost 15 km, and the region experiences a damaging M $>$ 6.0 event approximately every 10-20 years. The hazard is especially high in the densely populated Los Angeles basin, through which the San Andreas Fault runs. Southern California is well instrumented, containing dense networks of traditional seismometers facilitating a functioning EEW system that has recently become able to issue public alerts (Kohler et al. 2017). Nevertheless, MyShake would offer a complimentary set of triggers that could be used alongside traditional early warning and may be capable of more rapid and robust detections and alerts in the case of events occurring beneath urban areas.

Figure 5.9 shows MyShake simulation results for Southern California. The network performs relatively well here: most events have epicentral distance errors of less than 15 km, and those with a larger number of triggers appear to be located more accuracy, as expected. There is significant scatter in the magnitude-error graph, which can be attributed to the difficulty of estimating magnitudes from single ground acceleration values when earthquakes of a range of sizes produce broad and overlapping distributions of ground motion (e.g. Boore et al. 2014). Nevertheless, most events have magnitude errors of less than one unit. The time to first alert varies between 2.3 and 14.8 seconds, reflecting the spatial distribution of events and population centers shown in Figure 5.9b. As indicated by the histogram in 5.9a(4), a MyShake network generated by 0.1% of the population would be sufficient to reliably detect almost all events M $>$ 5.0 in this region. Many of the smaller events go undetected because they do not generate a sufficient number of triggers.

The histograms in Figure 5.9c show error distributions from 200 simulations of the 1994 M6.7 Northridge event. While the majority of errors are small, there is a tail of large magnitude, distance and time errors that correspond to instances where the event is initially very poorly located due to the uncertainties of the sampled phones and the generated triggers. Subsequent updates performed as the simulation proceeds act to remove these extreme error values.

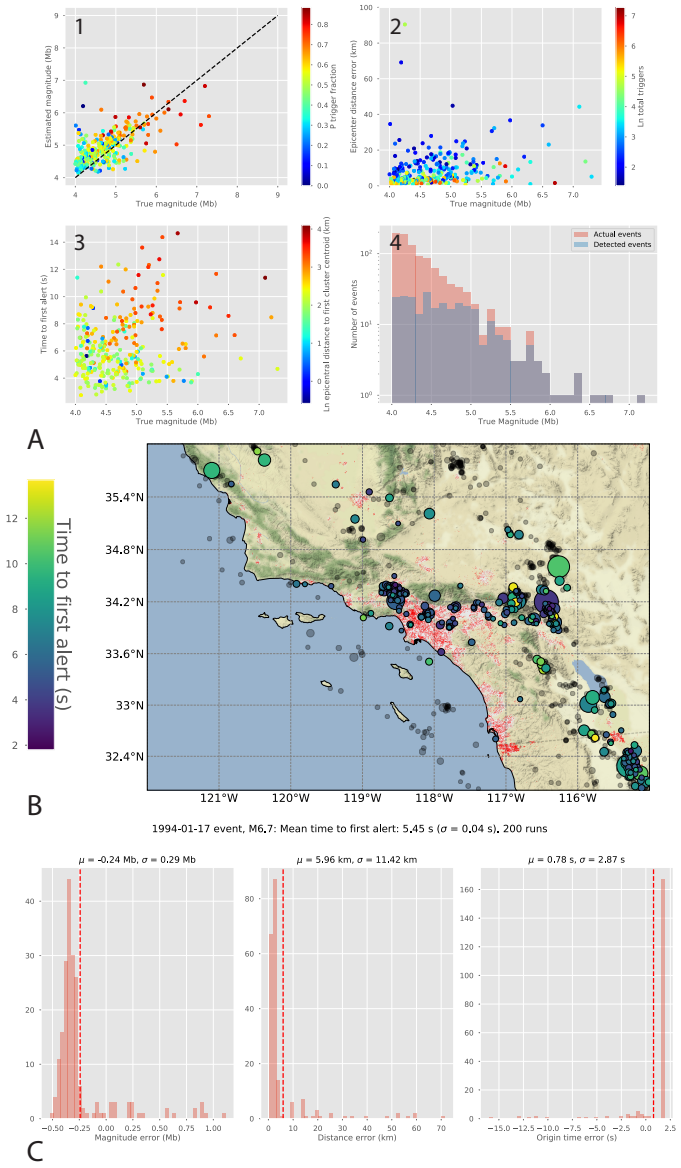

Figure 5.9: Summary of our simulation results for Southern California. Panel A highlights the performance of the network detection algorithm on all events M > 4.0 since 1980. Graph 1 plots estimated magnitude against USGS catalog magnitude, with earthquakes colored by the fraction of total triggers estimated to have occured in the P-wave. Graph 2 compares distance error against magnitude. Events are colored by the natural log of the total number of triggers. Graph 3 shows time to first alert as a function of magnitude, colored by the natural log of the epicentral distance to the centroid of the first trigger cluster identified by DBSCAN. This gives an indication of the distance between population centers and the earthquake. Graph 4 shows the proportion of actual events that are successfully detected, plotted on a log scale. Panel B is a map of the region, with earthquakes colored by the time to first alert from origin time of the earthquake. Red dots show the location of simulated MyShake users, representing 0.1% of the total population. Gray circles are events that were not detected. Finally, panel C shows the distribution of magnitude, distance and origin time errors resulting from 200 simulations of the M6.7 Borrego Springs event of 1994.

Haiti

The earthquake hazard in Haiti was brought to international attention by the devastating M7.0 event of 2010, which killed over 200,000 people and caused major economic damage (Bilham 2010). In addition to being one of the most densely populated Caribbean nations, Haiti is the poorest country in the western hemisphere and it suffered from weak to non-existent building regulation prior to 2010 (e.g. Bilham 2010, Frankel et al. 2011).

Haiti makes up roughly half of the island of Hispanola, which lies within a zone of deformation caused by motion of the Caribbean and North American plates (DesRoches et al. 2011). Haiti is the site of two major strike-slip faults: the Enriquillo Fault, on which the 2010 event occurred, which crosses densely populated regions in the south of the country and the Septentritional fault, which lies along the northern coast. Both have produced several major historical earthquakes (DesRoches et al. 2011). Haiti is also threatened by earthquakes occurring in two subduction zones: The Puerto-Rico Trough to the northeast and the Muertos Trough to the southeast. A traditional seismic network consisting of seven instruments was set up in the country following the 2010 earthquake, but is arguably too sparse to be useful for EEW. However, despite widespread poverty, mobile phone use in Haiti is ubiquitous and growing rapidly, making it potentially an ideal region for MyShake networks to take on the challenge of EEW here.

MyShake simulation results for Haiti are shown in Figure 5.10. Because of the high population density, shallow earthquakes and onshore faults the network performs well, arguably even better than in Southern California due to most of the events being onshore and close to the population clusters. All but one of the $M > 4.0$ events have epicentral distance errors of less than 20km and the scatter in magnitude estimates is significantly smaller than in the case of Southern California. Furthermore, the vast majority of all events $M > 4.5$ are successfully detected, including all onshore $M > 4.0$ events in Haiti and most in neighboring Puerto Rico. Combined with the low warning times, these results suggest that at 0.1% of the population, MyShake would be a very effective and much needed EEW tool for the people of Haiti. Furthermore, the 2010 event is located with distance errors of less than 6 km in 198 of the 200 test simulation runs, with a mean time to first detection of ~ 4.7 seconds and mean magnitude error of ~ 0.4 units. Again, these results are very encouraging and highlight the great potential benefits that MyShake could bring to developing nations that have limited fixed seismometers but ubiquitous mobile phone use.

Chile

Chile is one of the world's most seismically active regions. Tectonically, it is dominated by rapid suduction of the Nazca plate westward beneath the South American plate, which varies from about 80mm/yr in the south of the country to 65mm/yr in the north. Similar to other oceanic-continental convergence zones such as Central America and Japan, there

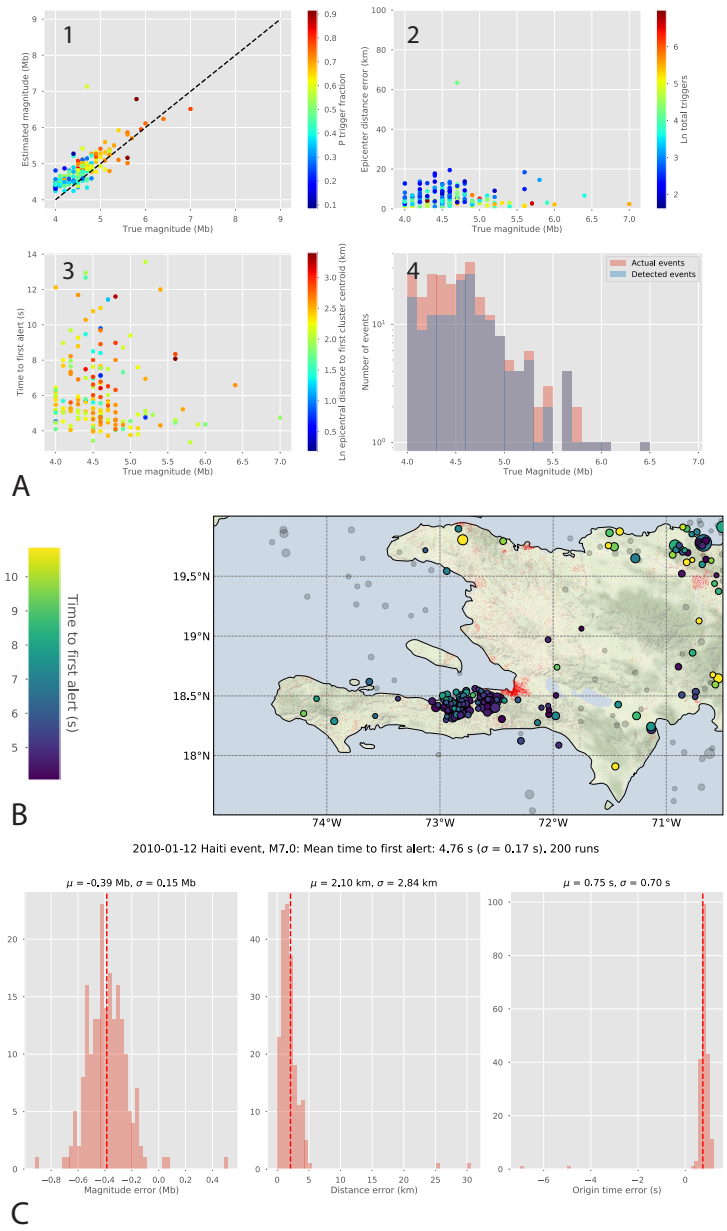

Figure 5.10: Summary of the simulation results for Haiti, with the panels arranged in the same format as in Figure 5.9. The network detection algorithm performs very well in this region, detecting the vast majority of M $>$ 4.0 events and locating them accurately in time, space and magnitude. As seen from panel B, many of the detected events are aftershocks of the 2010 M7.0 earthquake, and occur in very close proximity to densely populated regions of the country. Panel C shows the distribution of errors from 200 simulations of the 2010 event.

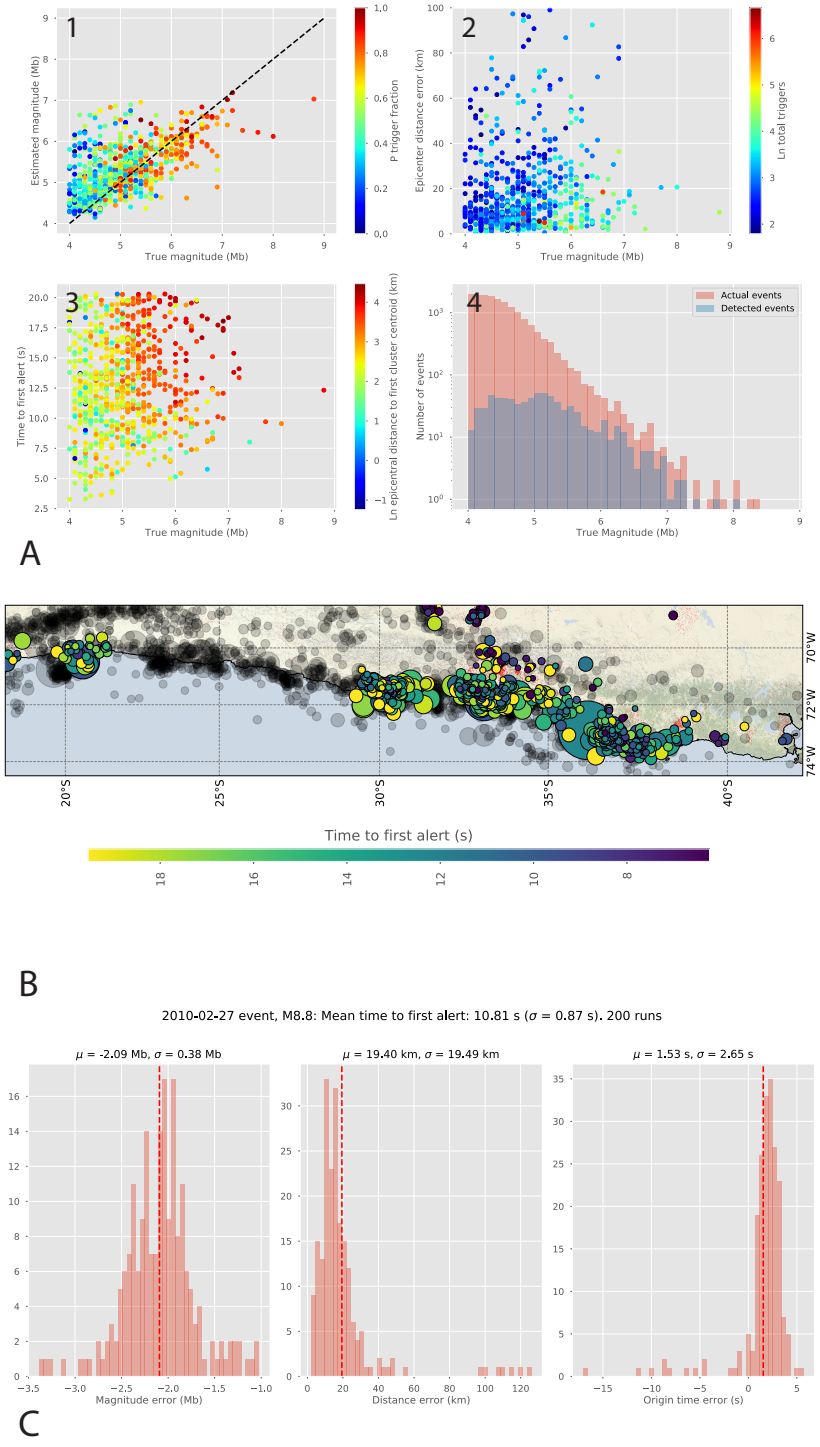

Figure 5.11: Summary of the simulation results for Chile. Chile is a classic subduction setting where the majority of the earthquakes occur offshore, to the west of population centers. This poses special challenges to the network detection algorithm, as reflected in its reduced performance here. Panel C shows its performance on simulations of the M8.8 2010 earthquake, which is the largest earthquake we attempted to simulated. Out magnitude scaling relationships and point source approximation are poorly suited to such an event.

are two main categories of earthquakes here; those occurring in the Wadati-Benioff zone, the largest of which tend to occur offshore near the Peru-Chile trench and those associated with deformation of the South American plate onshore in the forearc. In contrast to Central America, large subduction zone events here are frequent; numerous M > 8.0 events are known to have occured within the past century, many of which were responsible for major loss of life and economic damage. Notable earthquakes include the 1960 M9.5 near Valdivia, the largest recorded earthquake in history, the 2010 M8.8 in central Chile and the 2018 M8.3 near Illapel, all of which also generated large tsunamis.

The Chilean population is accustomed to experiencing earthquakes and much has been learned from the county's long history of devastating events. This has produced a high level of public awareness of the threat, strict building codes for life-safety and a significant monitoring effort on the part of the country's National Seismological Center.

The population distribution varies dramatically along the length of Chile. About 85% of the population live in urban areas, mainly those associated with the cities of Santiago and Valparaiso in the central part of the country. Many of these urban areas are coastal, putting them at risk of strong shaking and tsunamis generated by megathrust earthquakes. Our chosen region for earthquake simulation spans the country from -42°S to -18°S, encompassing the vast majority of its population and sites of major historical earthquakes.

Figure 5.11 shows our results. Our results for Chile are generally poorer than onshore settings such as Southern California and Haiti. Figure 5.11b shows that most events of M > 4.0 in close proximity to urban areas are detected, with events occurring further offshore generally having larger times to first alert. Figure 5.11a shows significant scatter in the the magnitude and location errors, especially for smaller events. This pattern is also seen in tests of the workflow at other subduction zones (namely Central America, Mexico and Japan) and is likely related to the challenging event-population geometry in these settings combined with the fact that the Cua & Heaton (2009) magnitude relations were not intended for use in subduction settings. This latter point is emphasised by the error histograms shown in Figure 5.11c, which were created by running 200 simulations of the M8.8 2010 event. The large magnitude errors clearly indicated that the Cua & Heaton (2009) relationship is saturated for events of this size. Despite these concerns, we suggest that MyShake networks could still be a valuable asset for issuing rapid warnings to urban areas in Chile, even if the choice was made not to include magnitude estimates in the warnings.

Nepal

Seismic hazard is also high in Nepal and northern India, which contain some of the world's most densely populated urban centers. These are at risk from major earthquakes occurring on thrust faults along the southern margin of the Himalayan mountains (Bilham et al. 2001). Most of the strain accumulated by India's 20mm/yr convergence with southern Tibet

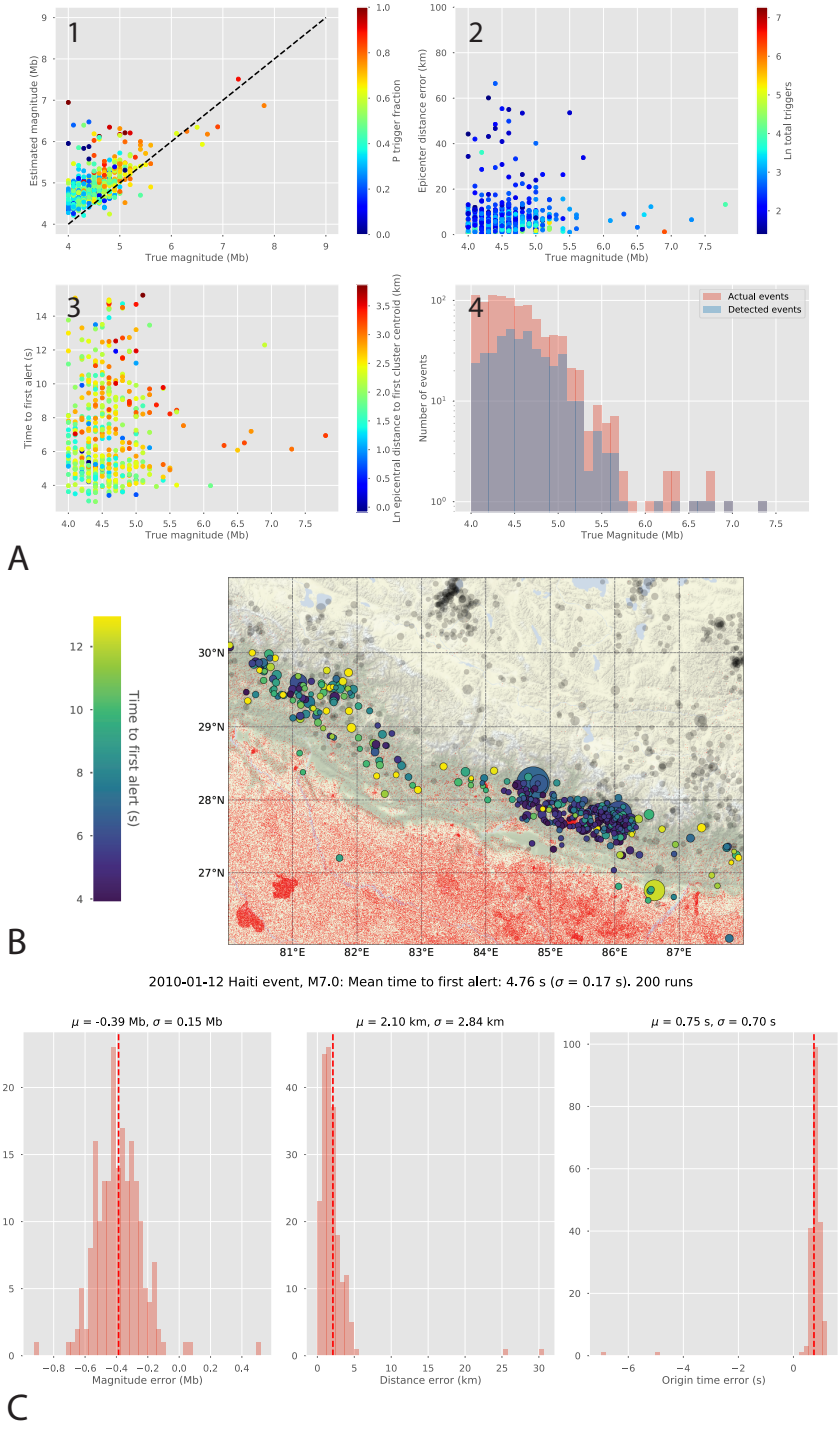

Figure 5.12: Summary of the simulation results for Nepal. The performance in this region is comparable to Southern California, although there is clearly bias in the magnitude estimation at low magnitudes. Most M $>$ 4.5 events south of the Himalayas are detected, but those to the north are too distant from population centers to cause enough triggers. The distributions of errors from the 200 simulations of the M7.8 2015 event (panel C) are broader than in the case of Southern California and Haiti, suggesting that the population distribution relative to the event poses more of a challenge to the network detection algorithm here.

is thought to be released by large earthquakes, with notable examples having occurred in 1803, 1833, 1897, 1895, 1932, 1950 and 2015. The 2015 M7.8 event brought international attention to the region, killing almost 9000 people. As in Haiti, many of the casualties occurred in due to the collapse of poorly constructed buildings in densely populated urban areas, most notably in Kathmandu. The National Seismological Center of Nepal operates a small network of traditional sensors in the country, which could potentially be used for EEW. However, mobile phone use in Nepal and northern India is already ubiquitous, with smartphone penetration at currently more than 50%. This suggests that there is great potential for MyShake networks to become the primary tool for EEW in this region.

Figure 5.12 summarizes our simulations in Nepal. Most of the detectable earthquakes occur in a narrow band just south of the Himalayas; those occurring north of the mountains in Tibet are typically too far from population centers to be detected. Our results here are somewhat similar to those for Southern California; most detected events have epicentral distance errors of less than 20km. In contrast to Southern California, the magnitudes of events in Nepal appear to be consistently overestimated by about 0.5Mb, suggesting that the Cua & Heaton (2009) relations used in the magnitude calculation workflow are not valid in this region and should be replaced with a version developed using events local to Nepal if MyShake is to be deployed here. Our simulations of the 2015 M7.8 earthquake indicate that it is consistently mislocated by about 10km and its magnitude is underestimated. Nevertheless, given a mean time to first alert of ~ 7 seconds, this would have provided Kathmandu with ~ 16 seconds of warning. Furthermore, this performance could likely be improved by tuning the parameters of the network detection algorithm.

Sulawesi

Indonesia is one of the most seismically active countries in the world. Many of the islands formed through volcanism and accretion of terranes along the region's two major tectonic boundaries. These consist of northwards subduction of the Indo-Australian plate beneath the Eurasian plate in the south and west and a very complex boundary involving subduction of both the Pacific and Philippine Sea plates in the northeast (e.g. Villeneuve et al. 2002). The island of Sulawesi lies just southeast of Borneo, near the center of the Indonesian archipelago and in a complicated and poorly understood tectonic setting that involves both subduction and strike-slip motion along the boundaries of several microplates (Villeneuve et al. 2002). Sulawesi was chosen for MyShake simulations because it is relatively densely populated, exhibits a diversity of seismic activity and suffered devastation in the M7.5 Palu event of 2018. Despite being having a predominantly strike-slip mechanism, this event generated a 2 meter high tsunami that inundated the coastal city of Palu and claimed over 4000 lives (Carvajal et al. 2019). In addition to that in 2018, Sulawesi has experienced three further tsunamigenic earthquakes during the past century and a host of damaging strike-slip events along the Palu-Koro and Matano faults, which cut though the island and lie close to urban areas (Carvajal et al. 2019). Similar to Haiti and Nepal, Sulawesi has no operating earthquake

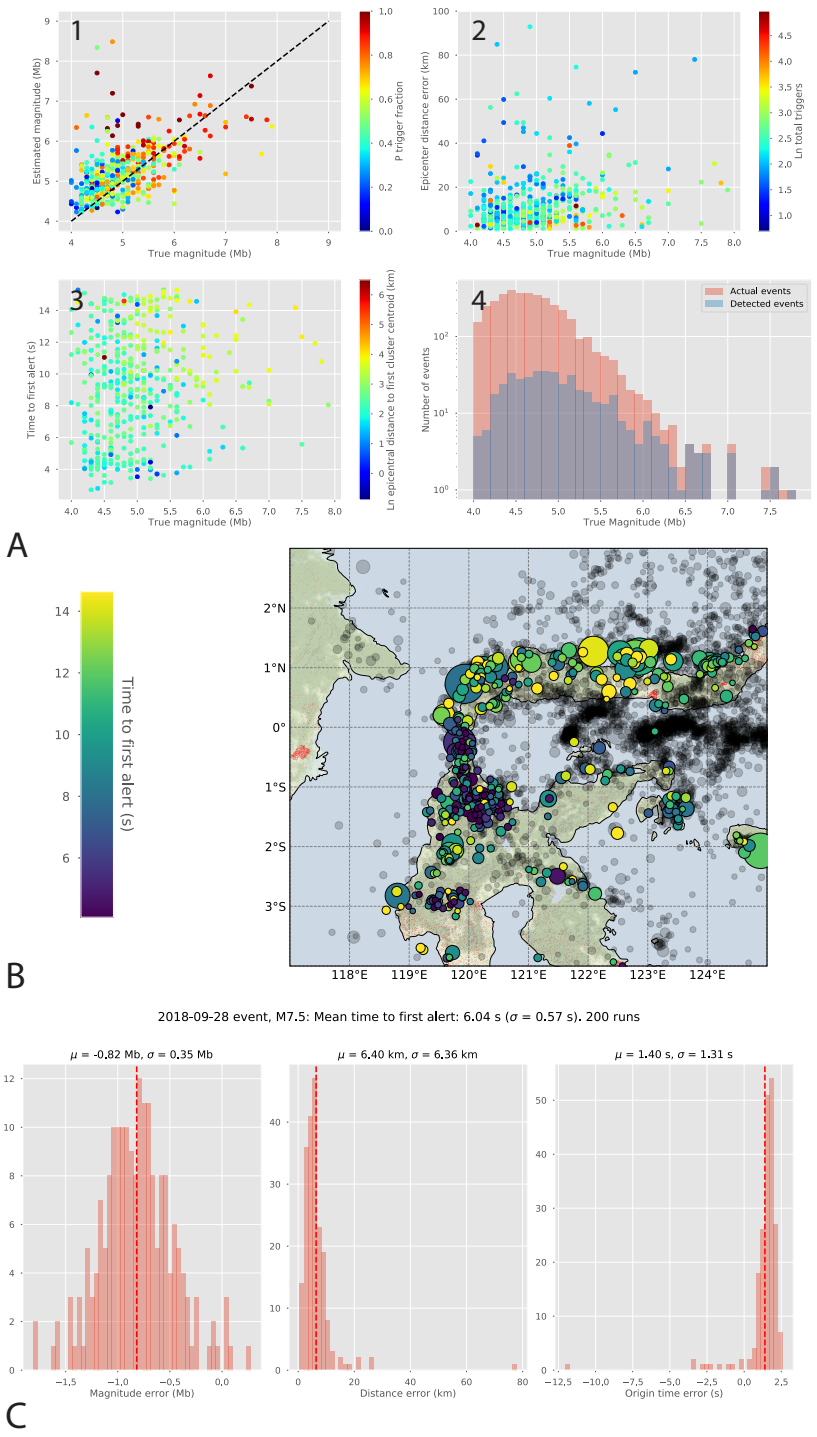

Figure 5.13: Summary of the results from the Indonesian island of Sulawesi. The performance is best for onshore earthquakes that occur near the densely populated Palu region, but events occurring just offshore along the northern coast are also reliably detected. Panel C shows simulation errors for the 2018 Palu event.

early warning system but smartphone use is widespread and growing rapidly. Again, this makes the area an ideal candidate to benefit from MyShake-based EEW.

Our results from Sulawesi simulations are shown in Figure 5.13. The colors in panel A(2) indicate that there are generally more triggers per event than in the case of Nepal, suggesting populations in closer proximity to the events. This observation is also supported by panel A(3). Variation in the magnitude and location estimation performance is likely due in part to variation in the tectonic regime: Events off the north coast of Sulawesi are typically offshore in a subduction setting, for example, while running through the central part of the island are occuring along the Palu-Koro and Matano transform faults. The locations and alert times of this second group of events are especially promising. The simulation also performs well in the case of the 2018 M7.5 Palu event. Its large size inevitably means that its magnitude is underestimated, but it is well located and an alert time of 6 seconds would have provided about 15 seconds of warning before the S wave reached the densely populated Palu region.

New Zealand

New Zealand is our final choice of demonstration regions for the MyShake simulation platform. Of the regions considered here, it is most similar to Southern California in terms of socioeconomic development, but has much lower population density and thus poses unique challenges for the network detection algorithm. In contrast to the aforementioned areas, earthquake fatalities here have historically been low, in part due to stringent construction regulations and a low population. Nevertheless, New Zealand is very seismically active. It sits astride a plate boundary that transitions from eastwards-verging subduction along the Hikurangi margin off the east coast of the North Island to left-lateral strike-slip motion along the Alpine Fault zone that bisects the South Island (Anderson et al. 1994). Four of the country's major cities, Christchurch, Wellington, Hastings and Napier, lie in close proximity to these major fault zones and have each suffered damage from $M > 7.0$ events over the past century. In the aftermath of the 2011 M6.2 Christchurch event, which killed 185 people, there has been renewed interest in seismic monitoring and EEW in New Zealand (Wood et al. 2012). MyShake networks could provide a valuable contribution here, alongside the country's already well-developed traditional monitoring network, which is maintained by the New Zealand Seismological Observatory.

Figure 5.14 summarizes the simulation results for New Zealand. The low population density means that only a small proportion of the total number of events are actually detected. Of those that are detected, most have epicentral distance errors of less than 20km and magnitude errors of less than 0.5Mb, although once again there is overestimation at the small magnitudes. The majority of these small events are aftershocks of the 2011 M6.1 earthquake. In our 200 simulations of this event, the magnitude error distribution is approximately centered on zero and the location is generally accurate. The mean first alert time of 4 seconds would not have been sufficient to issue warnings to central Christchurch, which is only 10

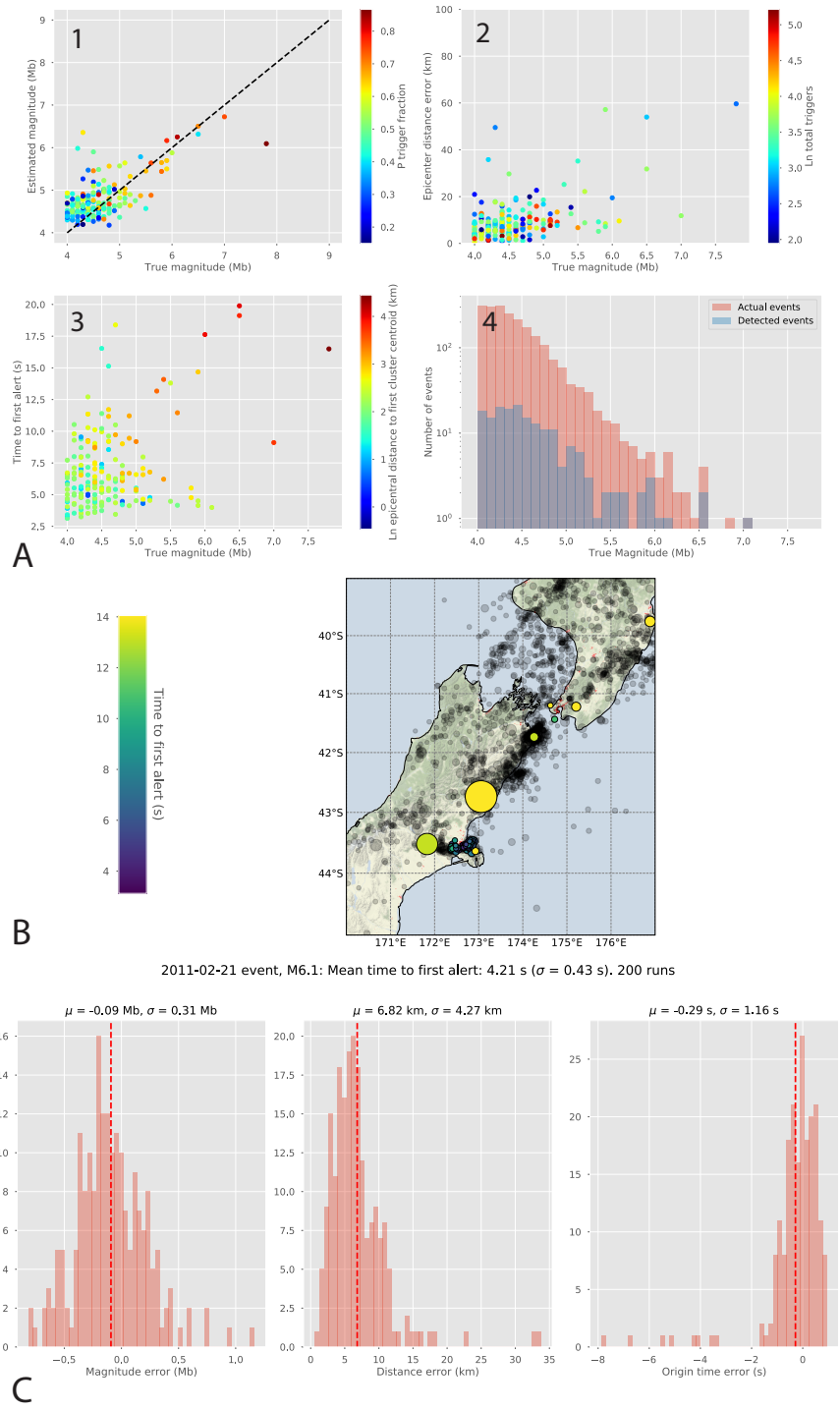

Figure 5.14: Summary of our simulation results for New Zealand. The region is sparsely populated, but events occurring close to urban areas are generally located accurately. Many of the M < 4.5 events that are successfully detected are aftershocks of the 2011 Christchurch earthquake. Panel C shows simulation errors from that M6.1 2011 event.

km from the epicenter. Nevertheless, the city's suburbs and nearby town of Ashburton could have received several seconds of warning had this network been present.

5.5 Discussion

Our results explore the application of a newly updated network detection algorithm to currently existing (section 3) and hypothetical (section 4) MyShake networks at the ambitious but not unreasonable penetration of 0.1% of the population. With a new design of the MyShake application (Rochford et al. 2018) aimed at user engagement, and the promise of issuing public early warnings, we expect a significant increase in the number of MyShake users globally. MyShake has great potential for earthquake early warning, the greatest advantage being that it can be used anywhere in the world at potentially much greater densities and at much lower cost than traditional, dedicated networks of seismometers. The results presented here provide us with a first order indication of the performance of the system in various regional settings around the globe. There are still many challenges that need to be addressed in order to improve the simulation platform and the network detection algorithm. In this discussion, we lay out some of the implications of our initial results and challenges associated with improving them in future.

The current triggering mechanism for individual phones in our simulation platform is an amplitude-based approach, which captures the general triggering pattern from the current MyShake network but it is far from perfect. The artificial neural network algorithm used in the MyShake application uses both the frequency and amplitude information from the waveforms, thus even at great distances with the amplitude is relatively small, the ANN can still recognize it as a seismic waveform. This is different from the current implementation of this simple amplitude based approach. A better way to model this triggering process needs to be developed in the future, likely by generating realistic seismic waveforms for various magnitude earthquakes at different distances and applying the ANN algorithm to derive a relationship. Furthermore, rapid but accurate magnitude estimation is another big challenge for the MyShake network, as it is for all EEW systems (e.g. Strauss et al. 2016).

As explained in section 2, earthquakes of a given magnitude produce broad distributions of ground motion with large uncertainties at a given distance, especially for the smartphones which are typically used in buildings without good coupling. There is also the added complication that the phones can be triggered either on the P or the S phase. Given the uncertainties associated with measuring the the ground motion from these devices, large amounts of observational data would be required to derive a reasonable empirical relationship. In the simulation platform, our trigger generation workflow attempts to account some of the uncertainties by sampling from a distribution with uncertainties built-in. However, since the distributions from different magnitudes overlap considerably at a given distance, especially for the P wave amplitude, it is difficult for any model to accurately estimate magnitude from

distance and initial acceleration alone.

The fact that our magnitude estimation performance varies considerably from region to region suggests that a more tailored approach is necessary in future refinements of the algorithm. Additionally, we find that location and magnitude accuracy improves with increasing confidence in our ability to discern whether a trigger has occurred on a P or an S phase, so increasing the accuracy of this from the current level of 70% could also be a fruitful avenue for future development. A machine learning model to distinguish the P and S wave triggers in real-time could help to address this issue, for example. Our results also show that in general events with more initial triggers tend to be located more accurately, which makes sense because the effect of any spuriously timed triggers tends to diminish as their total number increases. As the simulations proceed beyond the initial detection stage and incorporate more and more updates, the total number of triggers increases further. Consequently event locations do generally improve and outlier error values, such as those seen in panel C for many of the regions, disappear.

Our tests suggest that MyShake will be of greatest utility in densely populated, developing nations experiencing shallow crustal earthquakes occurring onshore in close proximity to urban areas. The results for Haiti are especially encouraging given the performance, socioeconomic conditions in the country and the obvious dire need to improve earthquake safety and public awareness here. Our detection workflow is more severely tested in subduction zone settings such as Chile, where the most destructive earthquakes tend to be very large and occur offshore. Evidently use of the Cua & Heaton (2009) amplitude-distance relationships to estimate magnitude and approximation of the events as point sources breaks down in the case of such earthquakes, leading to inaccuracies. Nevertheless, despite this limitation the algorithm is still able to quickly and accurately locate an earthquake, even in these most challenging settings. Furthermore, we have built the simulation platform and network detection workflow so that it is straightforward for users to adjust influential parameters and test different methods of magnitude estimation. Thus, the algorithm can be tailored to each region in which it is deployed.

The global MyShake network is currently in its infancy and there are an insufficient number of users at many places around the world to evaluate the system. This explains why we have built the simulation platform. We acknowledge that simulation results can only tell us so much, and fully expect to refine our trigger generation and network detection algorithm as MyShake gains popularity and more trigger data become available. Nevertheless, our simulations are a solid first test of the viability of MyShake networks as a tool for earthquake early warning on a truly global scale.

5.6 Concluding remarks

In this study, a new MyShake simulation platform with an updated network detection algorithm are proposed for a global smartphone earthquake early warning (EEW) system. We lay out the details of the first implementation of this simulation platform and test the updated network detection algorithm using real recordings from MyShake devices and hypothetical simulated events. Our results indicate that this updated network detection algorithm works reasonably well in most of the cases and can start to undergo tests on in real time on trigger data. Furthermore, simulated triggers in various regions from past events provide us with a first order understanding of MyShake's global performance and raise more challenges for us to tackle as more data becomes available from the growing MyShake network.

This final chapter is a testament to the wide range of research projects and opportunities ongoing at the Berkeley Seismological Laboratory. The most important contribution from this work is the MyShake simulation platform code itself, which was written by Qingkai Kong and Robert Martin-Short and is hosted on Github.

5.7 Chapter acknowledgments

The Gordon and Betty Moore Foundation fund this analysis through grant GBMF5230 to UC Berkeley. We thank the MyShake team members: Roman Baumgaertner, Garner Lee, Arno Puder, Louis Schreier, Stephen Allen, Stephen Thompson, Jennifer Strauss, Kaylin Rochford, Doug Neuhauser, Stephane Zuzlewski, Asaf Inbal, Sarina Patel and Jennifer Taggart for keeping this Project running and growing. We also thank all the MyShake users who contribute to the project.

Chapter 6

Conclusion

The work embodied in this dissertation has made the following major contributions the seismological research community.

- In Cascadia, we used seismic data from ocean bottom seismometers deployed as part of an ambitious, community-driven experiment (Toomey et al. 2014) to investigate the geometry of upper mantle flow between a spreading ridge and a subduction zone for the first time documented in the scientific literature. Our most important finding was that mantle flow beneath the small, slow-moving and internally-deforming Gorda plate appears to driven by shear imposed by the neighboring Pacific plate. This suggests that there may be a lower limit on size that controls a tectonic plate's ability to influence the underlying asthenosphere. It also offers an alternative interpretation for a toroidal pattern of seismic anisotropy observed in northern California by Eakin et al. (2010), suggesting that this may be due to material being drawn out from beneath North America by the motion of the Pacific plate.
- In Alaska, we used a combination of body wave, earthquake surface wave and ambient noise tomography, together with receiver function analysis to create some of the most comprehensive and detailed velocity models of the subsurface to date. This was made possible by deployments of Transportable Array (TA) seismometers across the entire state. We show that the subducting Pacific plate beneath Alaska ends in a sharp eastern edge, which has important implications for mantle flow (Venereau et al. 2019). Our images suggest that there is no deep slab beneath the enigmatic Wrangell Volcanoes, and that they likely formed at the northeastern edge of the subducted Yakutat terrane, an origin story that explains many of their unusual physical and geochemical features. Finally, or models allow us to interpret the possible cause of the Denali Volcanic Gap, which we suggest is due to isolation of the mantle wedge from hot, circulating asthenosphere by the shallow subduction of the thick oceanic crust of the Yakutat terrane.

- This dissertation also contains a contribution to the earthquake early warning literature. We describe a network detection algorithm that can generate early warnings using data from smartphones running the MyShake mobile application (e.g. Kong et al. 2016). We develop a workflow to test the ability of networks of MyShake devices to detect, locate and issue warnings about earthquakes in regions all over the world. Our network detection approach performs well, especially in densely populated regions at risk from shallow crustal earthquakes such as Haiti and Nepal. This contribution will be used by the MyShake development team as they continue to progress towards the goal of building the world's first crowd-sourced earthquake early warning system.

Bibliography

Accardo, NJ, et al. "Surface wave imaging of the weakly extended Malawi Rift from ambient-noise and teleseismic Rayleigh waves from onshore and lake-bottom seismometers". *Geophysical Journal International* 209.3 (2017): 1892–1905. Print.

Allam, AA, et al. "Ten kilometer vertical Moho offset and shallow velocity contrast along the Denali fault zone from double-difference tomography, receiver functions, and fault zone head waves". *Tectonophysics* 721 (2017): 56–69. Print.

Allen, Richard M, Paolo Gasparini, et al. "The status of earthquake early warning around the world: An introductory overview". *Seismological Research Letters* 80.5 (2009): 682–693. Print.

Allen, Richard M and Hiroo Kanamori. "The potential for earthquake early warning in southern California". *Science* 300.5620 (2003): 786–789. Print.

Allen, Richard M and Alon Ziv. "Application of real-time GPS to earthquake early warning". *Geophysical Research Letters* 38.16 (2011). Print.

Anderson, Helen and Terry Webb. "New Zealand seismicity: patterns revealed by the upgraded National Seismograph Network". *New Zealand journal of geology and geophysics* 37.4 (1994): 477–493. Print.

Arrial, Pierre-André and Magali I Billen. "Influence of geometry and eclogitization on oceanic plateau subduction". *Earth and Planetary Science Letters* 363 (2013): 34–43. Print.

Audet, Pascal, et al. "Seismic evidence for overpressured subducted oceanic crust and megathrust fault sealing". *Nature* 457.7225 (2009): 76. Print.

Barmin, MP, MH Ritzwoller, and AL Levshin. "A fast and reliable method for surface wave tomography". *Monitoring the Comprehensive Nuclear-Test-Ban Treaty: Surface Waves*. Springer, 2001. 1351–1375. Print.

Bastow, Ian D. "Relative arrival-time upper-mantle tomography and the elusive background mean". *Geophysical Journal International* 190.2 (2012): 1271–1278. Print.

Bauer, Mark A, Gary L Pavlis, and Michael Landes. "Subduction geometry of the Yakutat terrane, southeastern Alaska". *Geosphere* 10.6 (2014): 1161–1176. Print.

Bell, Samuel W, Donald W Forsyth, and Youyi Ruan. "Removing noise from the vertical component records of ocean-bottom seismometers: Results from year one of the Cascadia Initiative". *Bulletin of the Seismological Society of America* 105.1 (2014): 300–313. Print.

Bensen, GD, MH Ritzwoller, MP Barmin, et al. "Processing seismic ambient noise data to obtain reliable broad-band surface wave dispersion measurements". *Geophysical Journal International* 169.3 (2007): 1239–1260. Print.

Bensen, GD, MH Ritzwoller, and Nikolai M Shapiro. "Broadband ambient noise surface wave tomography across the United States". *Journal of Geophysical Research: Solid Earth* 113.B5 (2008). Print.

Bilham, Roger. "Lessons from the Haiti earthquake". *Nature* 463.7283 (2010): 878. Print.

Bilham, Roger, Vinod K Gaur, and Peter Molnar. "Himalayan seismic hazard". *Science* 293.5534 (2001): 1442–1444. Print.

Bird, Peter. "An updated digital model of plate boundaries". *Geochemistry, Geophysics, Geosystems* 4.3 (2003). Print.

Blackman, Donna K and J-Michael Kendall. "Sensitivity of teleseismic body waves to mineral texture and melt in the mantle beneath a mid–ocean ridge". *Philosophical Transactions of the Royal Society of London A: Mathematical, Physical and Engineering Sciences* 355.1723 (1997): 217–231. Print.

Bodmer, Miles A, et al. "Seismic anisotropy beneath the Juan de Fuca plate system: Evidence for heterogeneous mantle flow". *Geology* 43.12 (2015): 1095–1098. Print.

Bodmer, M, et al. "Buoyant asthenosphere beneath Cascadia influences megathrust segmentation". *Geophysical Research Letters* 45.14 (2018): 6954–6962. Print.

Boore, David M, et al. "NGA-West2 equations for predicting PGA, PGV, and 5% damped PSA for shallow crustal earthquakes". *Earthquake Spectra* 30.3 (2014): 1057–1085. Print.

Bostock, MG, et al. "An inverted continental Moho and serpentinization of the forearc mantle". *Nature* 417.6888 (2002): 536. Print.

Bowman, J Roger and Masataka Ando. "Shear-wave splitting in the upper-mantle wedge above the Tonga subduction zone". *Geophysical Journal of the Royal Astronomical Society* 88.1 (1987): 25–41. Print.

Boyden, James A, et al. "Next-generation plate-tectonic reconstructions using GPlates". (2011). Print.

Brennan, Patrick RK, Hersh Gilbert, and Kenneth D Ridgway. "Crustal structure across the central Alaska Range: Anatomy of a Mesozoic collisional zone". *Geochemistry, Geophysics, Geosystems* 12.4 (2011). Print.

Brudzinski, Michael R and Richard M Allen. "Segmentation in episodic tremor and slip all along Cascadia". *Geology* 35.10 (2007): 907–910. Print.

Carr, Michael J and Richard E Stoiber. "Geologic setting of some destructive earthquakes in Central America". *Geological Society of America Bulletin* 88.1 (1977): 151–156. Print.

Carvajal, Matías, et al. "Nearly-instantaneous tsunamis following the Mw 7.5 2018 Palu earthquake". *Geophysical Research Letters* (2019). Print.

Chaytor, Jason D, et al. "Active deformation of the Gorda plate: Constraining deformation models with new geophysical data". *Geology* 32.4 (2004): 353–356. Print.

Cheng, Cheng, et al. "Cascadia subduction slab heterogeneity revealed by three-dimensional receiver function Kirchhoff migration". *Geophysical Research Letters* 44.2 (2017): 694–701. Print.

Christensen, Douglas H and Geoffrey A Abers. "Seismic anisotropy under central Alaska from SKS splitting observations". *Journal of Geophysical Research: Solid Earth* 115.B4 (2010). Print.

Christeson, Gail L, et al. "The Yakutat terrane: Dramatic change in crustal thickness across the Transition fault, Alaska". *Geology* 38.10 (2010): 895–898. Print.

Chuang, Lindsay, et al. "Plateau subduction, intraslab seismicity, and the Denali (Alaska) volcanic gap". *Geology* 45.7 (2017): 647–650. Print.

Chung, AI, et al. "The Quake-Catcher Network rapid aftershock mobilization program following the 2010 M 8.8 Maule, Chile earthquake". *Seismological Research Letters* 82.4 (2011): 526–532. Print.

Clayton, Patricia M, Jeffrey W Berman, and Laura N Lowes. "Seismic performance of self-centering steel plate shear walls with beam-only-connected web plates". *Journal of constructional steel research* 106 (2015): 198–208. Print.

Cochran, Elizabeth S, et al. "The quake-catcher network: Citizen science expanding seismic horizons". *Seismological Research Letters* 80.1 (2009): 26–30. Print.

Cole, Frances, et al. "An integrated model for the tectonic development of the frontal Brooks Range and Colville Basin 250 km west of the Trans-Alaska Crustal Transect". *Journal of Geophysical Research: Solid Earth* 102.B9 (1997): 20685–20708. Print.

Colpron, Maurice, JL Nelson, Donald C Murphy, et al. "Northern Cordilleran terranes and their interactions through time". *GSA today* 17.4/5 (2007): 4. Print.

Conrad, Clinton P, Mark D Behn, and Paul G Silver. "Global mantle flow and the development of seismic anisotropy: Differences between the oceanic and continental upper mantle". *Journal of Geophysical Research: Solid Earth* 112.B7 (2007). Print.

Cua, Georgia and Thomas Heaton. "The Virtual Seismologist (VS) method: A Bayesian approach to earthquake early warning". *Earthquake early warning systems*. Springer, 2007. 97–132. Print.

Cua, Georgia and Thomas H Heaton. "Characterizing average properties of southern California ground motion amplitudes and envelopes". (2009). Print.

Currie, Claire A, et al. "Shear wave anisotropy beneath the Cascadia subduction zone and western North American craton". *Geophysical Journal International* 157.1 (2004): 341–353. Print.

Dashti, Shideh, et al. "Evaluating the reliability of phones as seismic monitoring instruments". *Earthquake Spectra* 30.2 (2014): 721–742. Print.

Debayle, Eric and Yanick Ricard. "Seismic observations of large-scale deformation at the bottom of fast-moving plates". *Earth and Planetary Science Letters* 376 (2013): 165–177. Print.

DeMets, Charles and Timothy H Dixon. "New kinematic models for Pacific-North America motion from 3 Ma to present, I: Evidence for steady motion and biases in the NUVEL-1A model". *Geophysical Research Letters* 26.13 (1999): 1921–1924. Print.

DesRoches, Reginald, et al. "Overview of the 2010 Haiti earthquake". *Earthquake Spectra* 27.S1 (2011): S1–S21. Print.

Eagar, Kevin C and Matthew J Fouch. "FuncLab: A MATLAB interactive toolbox for handling receiver function datasets". *Seismological Research Letters* 83.3 (2012): 596–603. Print.

Eakin, Caroline M, et al. "Seismic anisotropy beneath Cascadia and the Mendocino triple junction: Interaction of the subducting slab with mantle flow". *Earth and Planetary Science Letters* 297.3-4 (2010): 627–632. Print.

Eberhart-Phillips, Donna, et al. "Imaging the transition from Aleutian subduction to Yakutat collision in central Alaska, with local earthquakes and active source data". *Journal of Geophysical Research: Solid Earth* 111.B11 (2006). Print.

Ester, Martin, et al. "A density-based algorithm for discovering clusters in large spatial databases with noise." *Kdd*. 1996. 226–231. Print.

Ferris, Aaron, et al. "High resolution image of the subducted Pacific (?) plate beneath central Alaska, 50–150 km depth". *Earth and Planetary Science Letters* 214.3-4 (2003): 575–588. Print.

Finazzi, Francesco. "The earthquake network project: Toward a crowdsourced smartphone-based earthquake early warning system". *Bulletin of the Seismological Society of America* 106.3 (2016): 1088–1099. Print.

Finzel, Emily S, et al. "Upper plate proxies for flat-slab subduction processes in southern Alaska". *Earth and Planetary Science Letters* 303.3-4 (2011): 348–360. Print.

Fjeldskaar, W. "Viscosity and thickness of the asthenosphere detected from the Fennoscandian uplift". *Earth and Planetary Science Letters* 126.4 (1994): 399–410. Print.

Fontaine, Fabrice R, et al. "Upper-mantle flow beneath French Polynesia from shear wave splitting". *Geophysical Journal International* 170.3 (2007): 1262–1288. Print.

Frankel, Arthur, et al. "Seismic hazard maps for Haiti". *Earthquake Spectra* 27.S1 (2011): S23–S41. Print.

Fuis, Gary S, et al. "Trans-Alaska Crustal Transect and continental evolution involving subduction underplating and synchronous foreland thrusting". *Geology* 36.3 (2008): 267–270. Print.

Gallacher, RJ and ID Bastow. "The development of magmatism along the Cameroon Volcanic Line: Evidence from teleseismic receiver functions". *Tectonics* 31.3 (2012). Print.

Gao, Haiying. "Three-dimensional variations of the slab geometry correlate with earthquake distributions at the Cascadia subduction system". *Nature communications* 9.1 (2018): 1204. Print.

Gripp, Alice E and Richard G Gordon. "Young tracks of hotspots and current plate velocities". *Geophysical Journal International* 150.2 (2002): 321–361. Print.

Gutscher, Marc-André, et al. "Can slab melting be caused by flat subduction?" *Geology* 28.6 (2000): 535–538. Print.

Hacker, Bradley R, Geoffrey A Abers, and Simon M Peacock. "Subduction factory 1. Theoretical mineralogy, densities, seismic wave speeds, and H2O contents". *Journal of Geophysical Research: Solid Earth* 108.B1 (2003). Print.

Hager, Bradford H and Richard J O'Connell. "A simple global model of plate dynamics and mantle convection". *Journal of Geophysical Research: Solid Earth* 86.B6 (1981): 4843–4867. Print.

Hawley, William B, Richard M Allen, and Mark A Richards. "Tomography reveals buoyant asthenosphere accumulating beneath the Juan de Fuca plate". *Science* 353.6306 (2016): 1406–1408. Print.

Hayes, Gavin P, David J Wald, and Rebecca L Johnson. "Slab1. 0: A three-dimensional model of global subduction zone geometries". *Journal of Geophysical Research: Solid Earth* 117.B1 (2012). Print.

Heesemann, Martin, et al. "Ocean networks canada: from geohazards research laboratories to smart ocean systems". *Oceanography* 27.2 (2014): 151–153. Print.

Herrmann, Robert B. "Computer programs in seismology: An evolving tool for instruction and research". *Seismological Research Letters* 84.6 (2013): 1081–1088. Print.

Hosseini, Kasra and Karin Sigloch. "obspyDMT: A Python toolbox for retrieving and processing of large seismological datasets". *Solid Earth* 8 (2017). Print.

Huang, Zhouchuan, et al. "P-wave azimuthal anisotropic tomography in northern Chile: Insight into deformation in the subduction zone". *Journal of Geophysical Research: Solid Earth* (2018). Print.

Hung, S-H, FA Dahlen, and Guust Nolet. "Wavefront healing: a banana–doughnut perspective". *Geophysical Journal International* 146.2 (2001): 289–312. Print.

Jadamec, MA and MI Billen. "The role of rheology and slab shape on rapid mantle flow: Three-dimensional numerical models of the Alaska slab edge". *Journal of Geophysical Research: Solid Earth* 117.B2 (2012). Print.

Jadamec, Margarete A and Magali I Billen. "Reconciling surface plate motions with rapid three-dimensional mantle flow around a slab edge". *Nature* 465.7296 (2010): 338. Print.

Jiang, Chengxin, et al. "Upper Mantle Seismic Structure of Alaska From Rayleigh and S Wave Tomography". *Geophysical Research Letters* 45.19 (2018): 10–350. Print.

Jin, Ge and James B Gaherty. "Surface wave phase-velocity tomography based on multichannel cross-correlation". *Geophysical Journal International* 201.3 (2015): 1383–1398. Print.

Julia, J, et al. "Joint inversion of receiver function and surface wave dispersion observations". *Geophysical Journal International* 143.1 (2000): 99–112. Print.

Karato, Shun-ichiro, et al. "Geodynamic significance of seismic anisotropy of the upper mantle: new insights from laboratory studies". *Annu. Rev. Earth Planet. Sci.* 36 (2008): 59–95. Print.

Kendall, J-M, et al. "Magma-assisted rifting in Ethiopia". *Nature* 433.7022 (2005): 146. Print.

Kennett, BLN and ER Engdahl. "Traveltimes for global earthquake location and phase identification". *Geophysical Journal International* 105.2 (1991): 429–465. Print.

Kohler, Monica D, et al. "Earthquake early warning ShakeAlert system: West coast wide production prototype". *Seismological Research Letters* 89.1 (2017): 99–107. Print.

Kong, Qingkai, Richard M Allen, et al. "MyShake: A smartphone seismic network for earthquake early warning and beyond". *Science advances* 2.2 (2016): e1501055. Print.

Kong, Qingkai, Daniel T Trugman, et al. "Machine learning in seismology: Turning data into insights". *Seismological Research Letters* 90.1 (2018): 3–14. Print.

Lallemand, Serge, Arnauld Heuret, and David Boutelier. "On the relationships between slab dip, back-arc stress, upper plate absolute motion, and crustal nature in subduction zones". *Geochemistry, Geophysics, Geosystems* 6.9 (2005). Print.

Langston, Charles A. "Structure under Mount Rainier, Washington, inferred from teleseismic body waves". *Journal of Geophysical Research: Solid Earth* 84.B9 (1979): 4749–4762. Print.

Levshin, Anatoli, Ludmila Ratnikova, and JON Berger. "Peculiarities of surface-wave propagation across central Eurasia". *Bulletin of the Seismological Society of America* 82.6 (1992): 2464–2493. Print.

Lindsey, Nathaniel J, et al. "Fiber-optic network observations of earthquake wavefields". *Geophysical Research Letters* 44.23 (2017): 11–792. Print.

Liu, Lijun and Dave R Stegman. "Segmentation of the Farallon slab". *Earth and Planetary Science Letters* 311.1-2 (2011): 1–10. Print.

Long, Maureen D. "The Cascadia Paradox: Mantle flow and slab fragmentation in the Cascadia subduction system". *Journal of Geodynamics* 102 (2016): 151–170. Print.

Long, Maureen D and Paul G Silver. "The subduction zone flow field from seismic anisotropy: A global view". *science* 319.5861 (2008): 315–318. Print.

Luetgert, JH, et al. "NetQuakes-A new approach to urban strong-motion seismology". *AGU Fall Meeting Abstracts*. 2009. Print.

Maceira, Monica, et al. "On the validation of seismic imaging methods: Finite frequency or ray theory?" *Geophysical Research Letters* 42.2 (2015): 323–330. Print.

Madsen, JK, et al. "Cenozoic to Recent plate configurations in the Pacific Basin: Ridge subduction and slab window magmatism in western North America". *Geosphere* 2.1 (2006): 11–34. Print.

Maechling, Philip J, et al. "SCEC Broadband Platform: System architecture and software implementation". *Seismological Research Letters* 86.1 (2014): 27–38. Print.

Martin-Short, Robert, Richard M Allen, and Ian D Bastow. "Subduction geometry beneath south central Alaska and its relationship to volcanism". *Geophysical Research Letters* 43.18 (2016): 9509–9517. Print.

Martin-Short, Robert, Richard M Allen, Ian D Bastow, et al. "Mantle flow geometry from ridge to trench beneath the Gorda–Juan de Fuca plate system". *Nature Geoscience* 8.12 (2015): 965. Print.

Martin-Short, Robert, Richard Allen, et al. "Seismic Imaging of the Alaska Subduction Zone: Implications for Slab Geometry and Volcanism". *Geochemistry, Geophysics, Geosystems* 19.11 (2018): 4541–4560. Print.

McNamara, Daniel E and Michael E Pasyanos. "Seismological evidence for a sub-volcanic arc mantle wedge beneath the Denali volcanic gap, Alaska". *Geophysical Research Letters* 29.16 (2002): 61–1. Print.

Miller, Meghan S, et al. "Multiscale crustal architecture of Alaska inferred from P receiver functions". *Lithosphere* 10.2 (2018): 267–278. Print.

Minson, Sarah E, et al. "Crowdsourced earthquake early warning". *Science advances* 1.3 (2015): e1500036. Print.

Nelder, John A and Roger Mead. "A simplex method for function minimization". *The computer journal* 7.4 (1965): 308–313. Print.

Nelson, JL, et al. "Paleozoic tectonic and metallogenetic evolution of pericratonic terranes in Yukon, northern British Columbia and eastern Alaska". *Paleozoic evolution and metallogeny of pericratonic terranes at the ancient Pacific margin of North America, Canadian and Alaskan Cordillera: Geological Association of Canada Special Paper* 45 (2006): 323–360. Print.

Nettles, Meredith and Adam M Dziewoński. "Radially anisotropic shear velocity structure of the upper mantle globally and beneath North America". *Journal of Geophysical Research: Solid Earth* 113.B2 (2008). Print.

Nicolas, Adolphe and Nikolas I Christensen. "Formation of anisotropy in upper mantle peridotites-A review". *Composition, structure and dynamics of the lithosphere-asthenosphere system* 16 (1987): 111–123. Print.

Nishimura, Clyde E and Donald W Forsyth. "The anisotropic structure of the upper mantle in the Pacific". *Geophysical Journal International* 96.2 (1989): 203–229. Print.

Nokleberg, Warren J. *Phanerozoic tectonic evolution of the Circum-North Pacific*. US Department of the Interior, US Geological Survey, 2000. Print.

Nye, C. "The Denali volcanic gapfffdfffdfffdMagmatism at the eastern end of the Aleutian arc". *Eos Trans. AGU* 80.46 (1999): F1202. Print.

Obrebski, Mathias, Richard M Allen, Fred Pollitz, et al. "Lithosphere–asthenosphere interaction beneath the western United States from the joint inversion of body-wave traveltimes and surface-wave phase velocities". *Geophysical Journal International* 185.2 (2011): 1003–1021. Print.

Obrebski, Mathias, Richard M Allen, Mei Xue, et al. "Slab-plume interaction beneath the Pacific Northwest". *Geophysical Research Letters* 37.14 (2010). Print.

O'Driscoll, Leland J and Meghan S Miller. "Lithospheric discontinuity structure in Alaska, thickness variations determined by Sp receiver functions". *Tectonics* 34.4 (2015): 694–714. Print.

Page, Robert A, Christopher D Stephens, and John C Lahr. "Seismicity of the Wrangell and Aleutian Wadati-Benioff zones and the North American plate along the Trans-Alaska crustal transect, Chugach Mountains and Copper River basin, southern Alaska". *Journal of Geophysical Research: Solid Earth* 94.B11 (1989): 16059–16082. Print.

Paulson, Archie and Mark A Richards. "On the resolution of radial viscosity structure in modelling long-wavelength postglacial rebound data". *Geophysical Journal International* 179.3 (2009): 1516–1526. Print.

Pavlis, Terry L, et al. "Mid-Cretaceous extensional tectonics of the Yukon-Tanana Terrane, Trans-Alaska Crustal Transect (TACT), east-central Alaska". *Tectonics* 12.1 (1993): 103–122. Print.

Plafker, George and Henry C Berg. "Overview of the geology and tectonic evolution of Alaska". *The Geological Society of America, Boulder, Co* (1994): 989–1021. Print.

Polet, J and H Kanamori. "Upper-mantle shear velocities beneath southern California determined from long-period surface waves". *Bulletin of the Seismological Society of America* 87.1 (1997): 200–209. Print.

Pollitz, FF and J Arthur Snoke. "Rayleigh-wave phase-velocity maps and three-dimensional shear velocity structure of the western US from local non-plane surface wave tomography". *Geophysical Journal International* 180.3 (2010): 1153–1169. Print.

Porritt, Robert W, Richard M Allen, and Fred F Pollitz. "Seismic imaging east of the Rocky Mountains with USArray". *Earth and Planetary Science Letters* 402 (2014): 16–25. Print.

Porritt, Robert W and Meghan S Miller. "Updates to FuncLab, a Matlab based GUI for handling receiver functions". *Computers & geosciences* 111 (2018): 260–271. Print.

Porritt, Robert W, Meghan S Miller, and Fiona A Darbyshire. "Lithospheric architecture beneath Hudson Bay". *Geochemistry, Geophysics, Geosystems* 16.7 (2015): 2262–2275. Print.

Pratt, Martin J, et al. "Shear velocity structure of the crust and upper mantle of Madagascar derived from surface wave tomography". *Earth and Planetary Science Letters* 458 (2017): 405–417. Print.

Preece, Shari J and William K Hart. "Geochemical variations in the¡ 5 Ma Wrangell Volcanic Field, Alaska: implications for the magmatic and tectonic development of a complex continental arc system". *Tectonophysics* 392.1-4 (2004): 165–191. Print.

Qi, Cheng, Dapeng Zhao, and Yong Chen. "Search for deep slab segments under Alaska". *Physics of the Earth and Planetary Interiors* 165.1-2 (2007): 68–82. Print.

Randall, GE. "Efficient calculation of differential seismograms for lithospheric receiver functions". *Geophysical Journal International* 99.3 (1989): 469–481. Print.

Ratchkovski, Natalia A and Roger A Hansen. "New evidence for segmentation of the Alaska subduction zone". *Bulletin of the Seismological Society of America* 92.5 (2002): 1754–1765. Print.

Richards, Mark A, et al. "Role of a low-viscosity zone in stabilizing plate tectonics: Implications for comparative terrestrial planetology". *Geochemistry, Geophysics, Geosystems* 2.8 (2001). Print.

Richter, DH, et al. "Age and progression of volcanism, Wrangell volcanic field, Alaska". *Bulletin of Volcanology* 53.1 (1990): 29–44. Print.

Riddihough, Robin. "Recent movements of the Juan de Fuca plate system". *Journal of Geophysical Research: Solid Earth* 89.B8 (1984): 6980–6994. Print.

Rochford, Kaylin, et al. "MyShake: Using Human-Centered Design Methods to Promote Engagement in a Smartphonebased Global Seismic Network". *Frontiers in Earth Science* 6 (2018): 237. Print.

Rodi, WL, et al. "A fast, accurate method for computing group-velocity partial derivatives for Rayleigh and Love modes". *Bulletin of the Seismological Society of America* 65.5 (1975): 1105–1114. Print.

Rondenay, Stéphane, Geoffrey A Abers, and Peter E Van Keken. "Seismic imaging of subduction zone metamorphism". *Geology* 36.4 (2008): 275–278. Print.

Rondenay, Stéphane, Laurent GJ Montési, and Geoffrey A Abers. "New geophysical insight into the origin of the Denali volcanic gap". *Geophysical Journal International* 182.2 (2010): 613–630. Print.

Rossi, Giovannibattista, et al. "Unusual mantle Poisson's ratio, subduction, and crustal structure in central Alaska". *Journal of Geophysical Research: Solid Earth* 111.B9 (2006). Print.

Shapiro, Nikolai M, et al. "High-resolution surface-wave tomography from ambient seismic noise". *Science* 307.5715 (2005): 1615–1618. Print.

Shellenbaum, Diane P and PR LJ Delaney. "Top Mesozoic unconformity depth map of the Cook Inlet basin, Alaska". (2010). Print.

Shen, Weisen, et al. "Joint inversion of surface wave dispersion and receiver functions: a Bayesian Monte-Carlo approach". *Geophysical Journal International* 192.2 (2012): 807–836. Print.

Silver, Paul G and W Winston Chan. "Shear wave splitting and subcontinental mantle deformation". *Journal of Geophysical Research: Solid Earth* 96.B10 (1991): 16429–16454. Print.

Simutė, Saulė, et al. "Full-waveform inversion of the Japanese Islands region". *Journal of Geophysical Research: Solid Earth* 121.5 (2016): 3722–3741. Print.

Skulski, Thomas, Don Francis, and John Ludden. "Arc-transform magmatism in the Wrangell volcanic belt". *Geology* 19.1 (1991): 11–14. Print.

Song, Teh-Ru Alex and Hitoshi Kawakatsu. "Subduction of oceanic asthenosphere: Evidence from sub-slab seismic anisotropy". *Geophysical Research Letters* 39.17 (2012). Print.

Stachnik, JC, et al. "Determination of New Zealand ocean bottom seismometer orientation via Rayleigh-wave polarization". *Seismological Research Letters* 83.4 (2012): 704–713. Print.

Stachnik, Joshua C, Geoffrey A Abers, and Douglas H Christensen. "Seismic attenuation and mantle wedge temperatures in the Alaska subduction zone". *Journal of Geophysical Research: Solid Earth* 109.B10 (2004). Print.

Strauss, Jennifer A and Richard M Allen. "Benefits and costs of earthquake early warning". *Seismological Research Letters* 87.3 (2016): 765–772. Print.

Tian, Xiaobo, et al. "SKS splitting measurements with horizontal component misalignment". *Geophysical Journal International* 185.1 (2011): 329–340. Print.

Toomey, Douglas R, et al. "The Cascadia Initiative: A sea change in seismological studies of subduction zones". *Oceanography* 27.2 (2014): 138–150. Print.

Trop, Jeffrey M, et al. "Mesozoic and Cenozoic tectonic growth of southern Alaska: A sedimentary basin perspective". *SPECIAL PAPERS-GEOLOGICAL SOCIETY OF AMERICA* 431 (2007): 55. Print.

Uyeda, Seiya. “Subduction zones: an introduction to comparative subductology”. *Tectonophysics* 81.3-4 (1982): 133–159. Print.

Uyeda, Seiya and Hiroo Kanamori. “Back-arc opening and the mode of subduction”. *Journal of Geophysical Research: Solid Earth* 84.B3 (1979): 1049–1061. Print.

VanDecar, JC and RS Crosson. “Determination of teleseismic relative phase arrival times using multi-channel cross-correlation and least squares”. *Bulletin of the Seismological Society of America* 80.1 (1990): 150–169. Print.

Veenstra, Elizabeth, et al. “Crustal thickness variation in south-central Alaska”. *Geology* 34.9 (2006): 781–784. Print.

Venereau, CMA, et al. “The role of variable slab dip in driving mantle flow at the eastern edge of the Alaskan subduction margin: insights from SKS shear-wave splitting”. *Geochemistry, Geophysics, Geosystems* (). Print.

Villeneuve, Michel, et al. “Geology of the central Sulawesi belt (eastern Indonesia): constraints for geodynamic models”. *International Journal of Earth Sciences* 91.3 (2002): 524–537. Print.

Wang, Yun and Carl Tape. “Seismic velocity structure and anisotropy of the Alaska subduction zone based on surface wave tomography”. *Journal of Geophysical Research: Solid Earth* 119.12 (2014): 8845–8865. Print.

Ward, Kevin M. “Ambient noise tomography across the southern Alaskan cordillera”. *Geophysical Research Letters* 42.9 (2015): 3218–3227. Print.

Ward, Kevin M and Fan-Chi Lin. “Lithospheric structure across the Alaskan cordillera from the joint inversion of surface waves and receiver functions”. *Journal of Geophysical Research: Solid Earth* 123.10 (2018): 8780–8797. Print.

Ward, Kevin M, George Zandt, et al. “Lithospheric structure beneath the northern Central Andean Plateau from the joint inversion of ambient noise and earthquake-generated surface waves”. *Journal of Geophysical Research: Solid Earth* 121.11 (2016): 8217–8238. Print.

Webb, Spahr C. “Broadband seismology and noise under the ocean”. *Reviews of Geophysics* 36.1 (1998): 105–142. Print.

Wech, Aaron G. “Extending Alaskafffdfffdfffds plate boundary: Tectonic tremor generated by Yakutat subduction”. *Geology* 44.7 (2016): 587–590. Print.

Wei, Wei, et al. “P and S wave tomography and anisotropy in Northwest Pacific and East Asia: Constraints on stagnant slab and intraplate volcanism”. *Journal of Geophysical Research: Solid Earth* 120.3 (2015): 1642–1666. Print.

Wessel, Paul and Walter HF Smith. “New, improved version of Generic Mapping Tools released”. *Eos, Transactions American Geophysical Union* 79.47 (1998): 579–579. Print.

White, Randall A and David H Harlow. “Destructive upper-crustal earthquakes of Central America since 1900”. *Bulletin of the Seismological Society of America* 83.4 (1993): 1115–1142. Print.

Witt, Derek Richard. “Seismic anisotropy in Northwestern Canada and Eastern Alaska from shear wave splitting measurements”. Diss. Colorado State University, 2017. Print.

Wolfe, Cecily J and Paul G Silver. "Seismic anisotropy of oceanic upper mantle: Shear wave splitting methodologies and observations". *Journal of Geophysical Research: Solid Earth* 103.B1 (1998): 749–771. Print.

Wolfe, Cecily J and Sean C Solomon. "Shear-wave splitting and implications for mantle flow beneath the MELT region of the East Pacific Rise". *Science* 280.5367 (1998): 1230–1232. Print.

Wood, Peter R, et al. "The 2010-2011 Canterbury New Zealand earthquakes and the emergency management of buildings and infrastructure". *Proceedings of the 14th US-Japan Workshop on the Improvement of Structural Design and Construction Practices*. 2012. Print.

Worden, CB, et al. "Probabilistic relationships between ground-motion parameters and modified Mercalli intensity in California". *Bulletin of the Seismological Society of America* 102.1 (2012): 204–221. Print.

Worthington, Lindsay L, et al. "Crustal structure of the Yakutat terrane and the evolution of subduction and collision in southern Alaska". *Journal of Geophysical Research: Solid Earth* 117.B1 (2012). Print.

Wüstefeld, Andreas and Götz Bokelmann. "Null detection in shear-wave splitting measurements". *Bulletin of the Seismological Society of America* 97.4 (2007): 1204–1211. Print.

Wüstefeld, Andreas, Götz Bokelmann, Guilhem Barruol, et al. "Identifying global seismic anisotropy patterns by correlating shear-wave splitting and surface-wave data". *Physics of the Earth and Planetary Interiors* 176.3-4 (2009): 198–212. Print.

Wüstefeld, Andreas, Götz Bokelmann, Christophe Zaroli, et al. "SplitLab: A shear-wave splitting environment in Matlab". *Computers & Geosciences* 34.5 (2008): 515–528. Print.

Wüstefeld, Andreas, Othman Al-Harrasi, et al. "A strategy for automated analysis of passive microseismic data to image seismic anisotropy and fracture characteristics". *Geophysical Prospecting* 58.5 (2010): 755–773. Print.

You, Tian and Dapeng Zhao. "Seismic anisotropy and heterogeneity in the Alaska subduction zone". *Geophysical Journal International* 190.1 (2012): 629–649. Print.

Zandt, George and E Humphreys. "Toroidal mantle flow through the western US slab window". *Geology* 36.4 (2008): 295–298. Print.

Zhao, Dapeng, Douglas Christensen, and Hans Pulpan. "Tomographic imaging of the Alaska subduction zone". *Journal of Geophysical Research: Solid Earth* 100.B4 (1995): 6487–6504. Print.

Zhu, Lupei and Hiroo Kanamori. "Moho depth variation in southern California from teleseismic receiver functions". *Journal of Geophysical Research: Solid Earth* 105.B2 (2000): 2969–2980. Print.